Diss. ETH N° 28726

Jérôme Gabathuler

The thickness of the quasi-liquid layer on ice and its interaction with atmospheric gases as seen by X-ray absorption and photoelectron spectroscopies

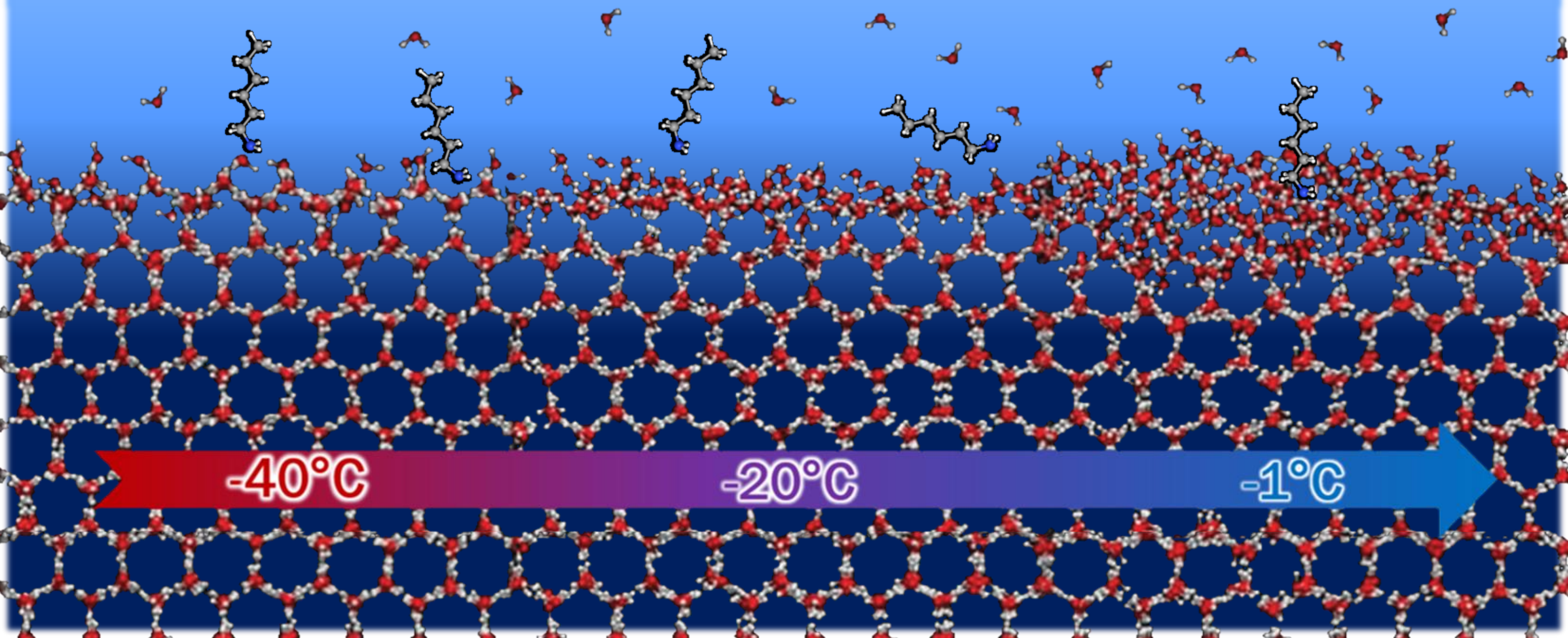

Diss. ETH No. 28726

THE THICKNESS OF THE QUASI-LIQUID LAYER ON ICE AND ITS INTERACTION WITH ATMOSPHERIC GASES AS SEEN BY X-RAY ABSORPTION AND PHOTOELECTRON SPECTROSCOPIES

A dissertation submitted to attain the degree of

Doctor of Sciences of ETH Zurich
(Dr. sc. ETH Zurich)

presented by

Jérôme Gabathuler
MSc. in Applied Physics, EPFL

born on 4 july 1993
citizen of Switzerland

accepted on the recommendation of

Prof. Markus Ammann
Prof. Thomas Peter
Dr. Hendrik Bluhm

2023

Jérôme Gabathuler: *The thickness of the quasi-liquid layer on ice and its interaction with atmospheric gases as seen by X-ray absorption and photoelectron spectroscopies,*

ABSTRACT

Ice is ubiquitous in the environment and plays a role in atmospheric chemical cycles, which impacts the environment and human health. Therefore, it is important to understand the mechanism by which ice interacts with the air. The commonly accepted picture is the presence of a quasi-liquid layer (QLL) on the surface of the ice that increases in thickness with increasing temperature or with increasing concentrations of soluble species.

X-ray excited electron spectroscopy, X-ray photoelectron spectroscopy (XPS), and partial electron yield X-ray absorption spectroscopy (PEY-XAS) are well-suited surface science techniques to investigate the QLL at the interface between the ice and the air of the atmosphere. While XPS enables a quantitative surface sensitive elemental and chemical composition analysis, PEY-XAS provides insights into the structure of the hydrogen bonding (HB) network in the ice lattice close to the surface.

In the frame of this thesis, I investigated the thickness of the QLL on ice as a function of temperature. I developed a careful analysis of the different uncertainties related to PEY-XAS, with a special focus on the assessment of the probing depth in PEY-XAS, using a Monte Carlo (MC) simulation of electron scattering. The results indicate that, at the probing kinetic energy (KE) window typically used to detect electrons in PEY-XAS, the escape depth is about $\sim$3 times larger compared to that of unscattered electrons and that gas phase scattering decreases this factor down to $\sim$1.5, at 5 mbar. Consideration of electron scattering in PEY-XAS is novel and the improved analysis of the PEY-XAS data reveals that the QLL is of the order of $\sim$2 nm close to the melting point.

After the QLL investigation on pure ice, I studied the adsorption of hexylamine (HA) on ice to complement the large literature that is available about the adsorption of acids on ice. I measured the surface coverage of HA as a function of gas-phase partial pressure, and for two different temperatures. I found that a saturated monolayer is present already at a partial pressure of 2×10^{-5} mbar, and that more than half of the HA molecules are protonated. The PEY-XAS data revealed that the adsorbed HA on ice at -20°C increases the fraction of water molecules in disordered configurations, and give a PEY-XAS signal similar to that of pure ice at -1°C. This is expected and has been observed in the literature with different acids such as HCl.

Finally, I studied the temperature dependence of the surface disorder in liquid water and found that the latter increases with temperature, similar to the QLL on ice. As a logical continuation of the MC simulation results, I established the proof-of-principle of PEY-XAS depth profiling ability on an ice sample, by probing the HB network and the carbon contamination as a function of depth. Last but not least, I investigated the direct impact of gas phase pressure (in this experiment, N_2) on the surface disorder of the ice and found no impact at -120°C.

RÉSUMÉ

Au sol ou dans l'atmosphère, la glace est omniprésente dans l'environnement et interagit avec des espèces de gaz à l'état de traces. La glace joue un rôle dans les cycles chimiques atmosphériques, qui ont une incidence sur l'environnement et la santé humaine. Par conséquent, il est important de comprendre le mécanisme par lequel la glace interagit avec l'atmosphère. L'image communément acceptée est la présence d'une couche quasi-liquide (QLL, pour Quasi-Liquid Layer en anglais) à la surface de la glace qui augmente en épaisseur lorsque la température augmente et/ou en présence d'impuretés.

La spectroscopie photoélectronique par rayons X (XPS), et la spectroscopie d'absorption des rayons X (PEY-XAS) sont deux outils expérimentaux qui permettent d'étudier la surface de la glace et son interaction avec l'atmosphère. Avec XPS, il est possible d'analyser quantitativement les concentrations des différents éléments présents sur la surface de la glace, et de connaître leurs configurations chimiques. Avec PEY-XAS, il est possible de mesurer le degré de coordination des liaisons hydrogènes dans la maille de la glace.

Dans le cadre de cette thèse, j'ai étudié la dépendance en température de la QLL. J'ai développé une analyse rigoureuse des différentes incertitudes liée aux techniques expérimentales, en mettant l'accent sur la sensibilité de sondage en profondeur. Pour ce faire, j'ai programmé une simulation du type Monte-Carlo qui reproduit les processus physiques sur lesquels sont basés les observations expérimentales. Les résultats indiquent que le choix de l'énergie cinétique mesurée avec PEY-XAS peut augmenter la profondeur de sondage par un facteur $\sim$3 et que la perte d'énergie cinétique par diffusion dans la phase gas ramène ce facteur à $\sim$1.5, pour une pression de 5 mbar. L'analyse améliorée des données révèle que la QLL est plutôt mince par rapport à ce qui a été déterminé dans la littérature scientifique.

Après l'analyse de la QLL, j'ai étudié l'adsorption de l'hexylamine sur la glace. J'ai mesuré la concentration de surface en fonction de la concentration en phase gas et ce, pour deux températures différentes. J'ai trouvé qu'une monocouche saturée était présente déjà à une concentration de 2×10^{-5} mbar, et que plus de la moitié des molécules d'hexylamine étaient protonées. Les données PEY-XAS ont révélé que l'adsorption de l'hexylamine augmente la part des molécules d'eau en configuration désordonnée.

Enfin, j'ai étudié la dépendance en température du désordre à l'interface entre l'eau liquide et l'air. J'ai trouvé que, de manière similaire à la QLL sur la glace, le désordre du réseau de liaison hydrogène dans l'eau liquide augmente avec la température. En rapport avec les incertitudes liées aux techniques expérimentales, j'ai caractérisé le flux de lumière utilisé en spectroscopie de rayon X. J'ai trouvé que ce dernier se composait d'une part importante de second ordre, ce qui pouvait influencer les résultats non seulement pour PEY-XAS, mais aussi pour les profils en profondeur mesurés avec XPS. Comme suite logique des résultats de la simulation Monte-Carlo j'ai établi une preuve

de concept concernant le potentiel de PEY-XAS à mesurer différentes profondeurs. Dernier point, mais non le moindre, j'ai mesuré l'impact direct de la pression au sens thermodynamique sur le désordre à la surface de la glace.

ACKNOWLEDGEMENTS

I would like to thank my supervisor and main adviser Prof. Markus Ammann for guiding me through the doctoral studies at the Department of Environmental Systems Science, ETH Zürich. Besides his profound insight and knowledge, I appreciated his human sense for understanding.

I would like to thank Dr. Thorsten Bartels-Rausch for supervising me in the beggining of my PhD, as well as the whole Laboratory of Environmental Chemistry (LUC) for the pleasant atmosphere and the sensational coffee-breaks.

I would like to thank the swimming club of PSI for the team spirit during the winter swims in the Aare. Thank you for helping me cool down and for challenging my physical and mental limits. Thanks to Kamil and Jiří for the interesting conversations.

I would like to thank Hendrik Bluhm for the small science talks during his visits at PSI.

I would like to thank my girlfriend Ekaterina, for the kindness, assistance, and 24/7 mental support.

I would like to thank my parents, and especially my mother for believing in my success and helping me in every possible ways.

Last but not least, I would like to thank the Swiss National Science Foundation (grant 178962) and by extension all the taxpaying citizens of Switzerland for funding this work.

Some external factors have contributed to making this work more challenging to achieve and I would like to acknowledge them here.

I would like to NOT thank the coronavirus, for making innocent victims but especially for causing an avalanche of restrictions on the people, inhibiting social interactions, and generating a wave of damages to society that are yet to be discovered.

I would like to NOT thank the political events that started on the 24th of February 2022, which also happened to be the beginning of my second hexylamine beamtime.

CONTENTS

NOTATION

Frequently used symbols

E_{ph}	photon energy
BE	binding energy
KE_e	kinetic energy
$\langle T_{loss} \rangle$	average kinetic energy loss

Physical constants

$k_B = 1.38 \times 10^{-23}\,\mathrm{J\,K^{-1}}$	Boltzmann constant
$T^0 = 273.15\,\mathrm{K}$	temperature of the ice at the triple point

Abbreviations

IMFP	Inelastic Mean Free Path $\equiv$ mean distance between 2 inelastic scattering events
MPD	Mean Probing Depth
HB	Hydrogen-bond

1

INTRODUCTION

> *If you can't explain it simply, you don't understand it well enough.*
>
> — Albert Einstein

1.1 Water

Water (H_2O) is the simplest molecule consisting of the most abundant element in the universe (hydrogen) and the most abundant element on Earth (oxygen). With an O−H bond length just below 1 Å [1–3] and a molar mass of $18\,\mathrm{g\,mol^{-1}}$, very few molecules are smaller or lighter. From a human perspective, water is tasteless, colorless, transparent, and ubiquitous on Earth i.e. nothing extraordinary. However, despite its simple appearance, water is a fascinating material that adopts complex structures in the condensed phase and exhibits unusual properties.

The anomalous properties of water are well described in the review by Brini et al. [4]. Among them, we can cite the high melting and boiling point, which allow water to be ubiquitous on Earth in the three phases. Water has a high surface tension due to the cohesive property of water molecules. Water can be sticky and slippery at the same time, and this 'stick/slip' feeling is how we can identify water by touching [5]. Water is a polar molecule and its liquid form can dissolve polar and ionic solutes. However, water differs from most other solvents when it is in contact with nonpolar molecules. This difference has been named 'the hydrophobic effect' [4].

Another notable anomalous property of water is that not only it expands upon freezing, but its density increases from room temperature down to ∼+4 °C and then, decreases from about +4 °C down to supercooled temperatures, as if tiny ice crystals start to nucleate in the thermodynamic liquid. Molecular dynamics (MD) studies have shown that while the mean distance of each oxygen atom to its four nearest oxygen atoms decreases with temperature as expected, it is the mean distance of each oxygen atom to its *fifth* nearest oxygen atom that increases unexpectedly upon cooling below +25 °C [6]. This property of water is very favorable for aquatic life to survive during the winter: as lakes' and rivers' temperatures cool down, the temperature gradient reverses at about +4 °C allowing the ice to grow on the surface while the bottom layer of the water body stays above 0 °C, as illustrated in Figure 1.1.

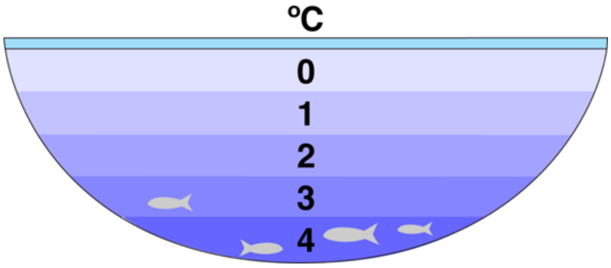

FIGURE 1.1: Lakes and rivers freeze from the top and provide insulation from the cold air. Ice floats because it is less dense than the liquid. So, even in wintry frozen lakes, fish can survive at the bottom of frozen lakes and rivers, where water is liquid. Taken from [4].

The phase diagram of water is complex, with many crystalline forms as shown on Figure 1.2.

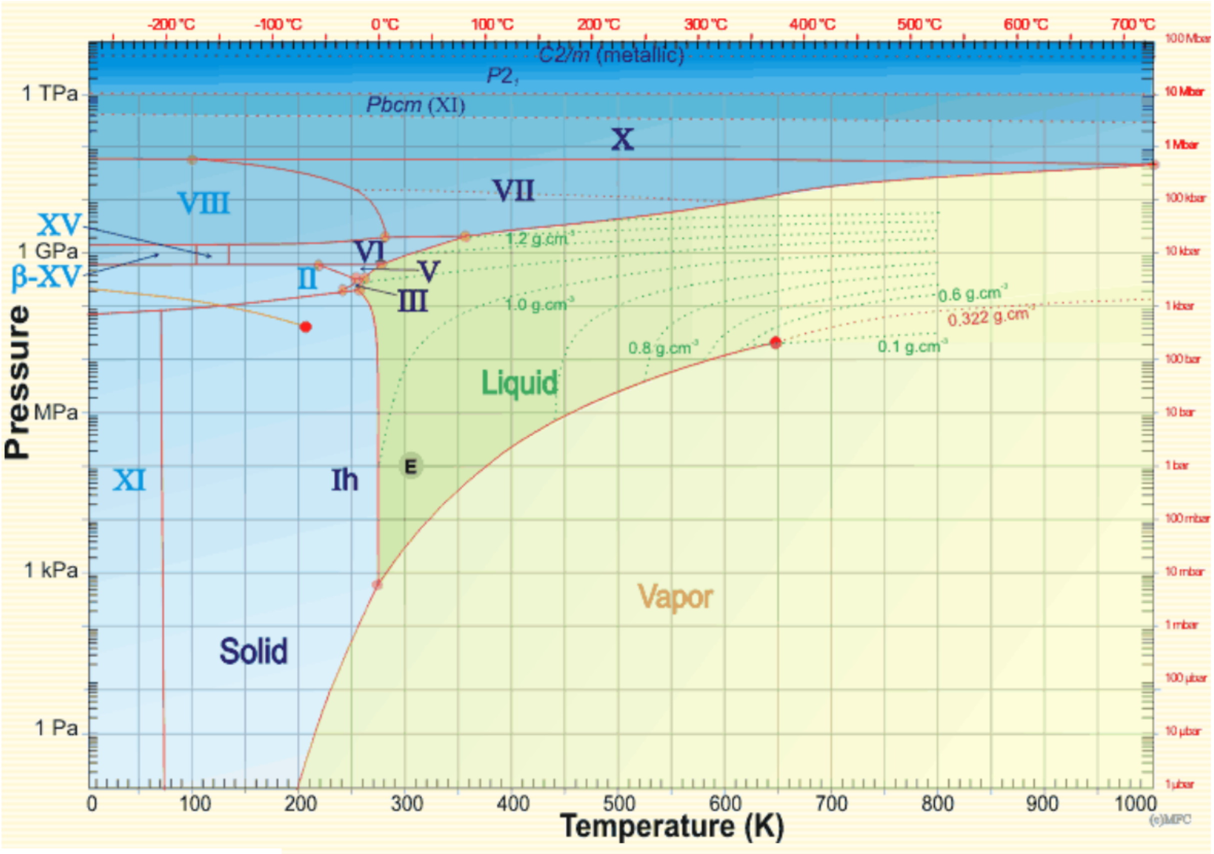

FIGURE 1.2: Phase diagram of water. Taken from [7].

On a phase line, the slope of the line $\frac{dP}{dT}$, can be expressed according to the Clausius–Clapeyron relation:

$$\frac{dP}{dT} = \frac{L}{T\Delta V} = \frac{\Delta S}{\Delta V} \tag{1.1}$$

where L is the latent heat (enthalpy change) for the phase change, ΔV is the change in volume, and ΔS is the change in entropy. We note that because the volume change from ice I_h to liquid water ΔV is negative, the slope of the solidus line must also be negative, which is not the case for melting from other solid phases such as ice VI, VII or X.

Many of the unusual properties of water are attributed to the ability of water molecules to form hydrogen bonds. The hydrogen bond is an attractive force between one of the hydrogen nucleus from one water molecule and one of the oxygen's lone pairs from a neighboring molecule. The hydrogen bond is weaker than the covalent bond linking the hydrogens to their respective oxygens in the water molecules, but it is sufficiently strong to overcome thermal fluctuations in the stability domain of the liquid phase (see green area in Figure 1.2), and impose a bulk-wide order when the temperature is sufficiently low (blue area in Figure 1.2).

Thanks to the strength of hydrogen bonds, water has very high melting and boiling points (without hydrogen bonds, water would boil at around -100°C [1]) and ice is ubiquitous in the environment [8, 9], mainly in its hexagonal crystal form I_h (see Figure 1.2). Where the temperature is below 0°C, that is, at high enough altitudes or latitudes, ice is found in various forms such as sea ice, ice caps, glaciers, snow, and clouds. Ice crystal growth is another fascinating topic, but since it is not really the subject of this thesis, I only mention here a very interesting review from K. G. Libbrecht [10], his apparatus for growing designer snow crystals [11], and his snow crystals website [12]. The physics of ice has been a field of intense scientific controversies. The friction coefficient of pure ice with any other solid material is surprisingly low [13], especially considering the fact that ice does not need to be lubricated to be slippery. But is it really not lubricated? In the 1850s, Faraday was the first to propose an answer to this question and to suggest the existence of an interfacial disorder. This thin film of (partially) disordered matter at the surface of the ice has also been named Quasi Liquid Layer (QLL), Liquid-Like Layer (LLL), disordered interface (DI), or premelting. Since then, the explanation of the QLL causing the slipperiness of ice has been controversially discussed. In particular, pressure melting [14] has been put forward to explain the slipperiness without provoking premelting; an idea that was later rejected, and today, it is clear that both friction heating and premelting lead to the slipperiness of ice [15]. This example shows that the differentiation between melting -a liquid bulk phase-, and premelting –an interfacial phenomenon-, is not trivial and has led to controversial discussions from the beginning.

Starting in the late 1970s, the QLL has been intensively investigated using a number of experimental techniques [15]. While there is a general agreement in the literature that the QLL emerges with increasing temperatures, there is a debate about the precise thickness and on-set temperature [16]. Currently, evaluations of the thickness of the QLL at -10°C scatter by two orders of magnitude as shown on Figure 1.3). Several arguments discussed in the literature suggest that the presence of impurities and experimental artefacts contribute to the scatter in the results of Figure 1.3: In atomic force microscopy (AFM) for example, surface tension may lead to the attraction of water molecules to the AFM tip, which is a likely explanation why this technique probes a rather large QLL in contact mode (g,i). Optimizing the use of AFM, and

---

[1] as expected by extrapolation of the boiling points of other Group 6A hydrides (H_2Po, H_2Te, H_2Se, H_2S)

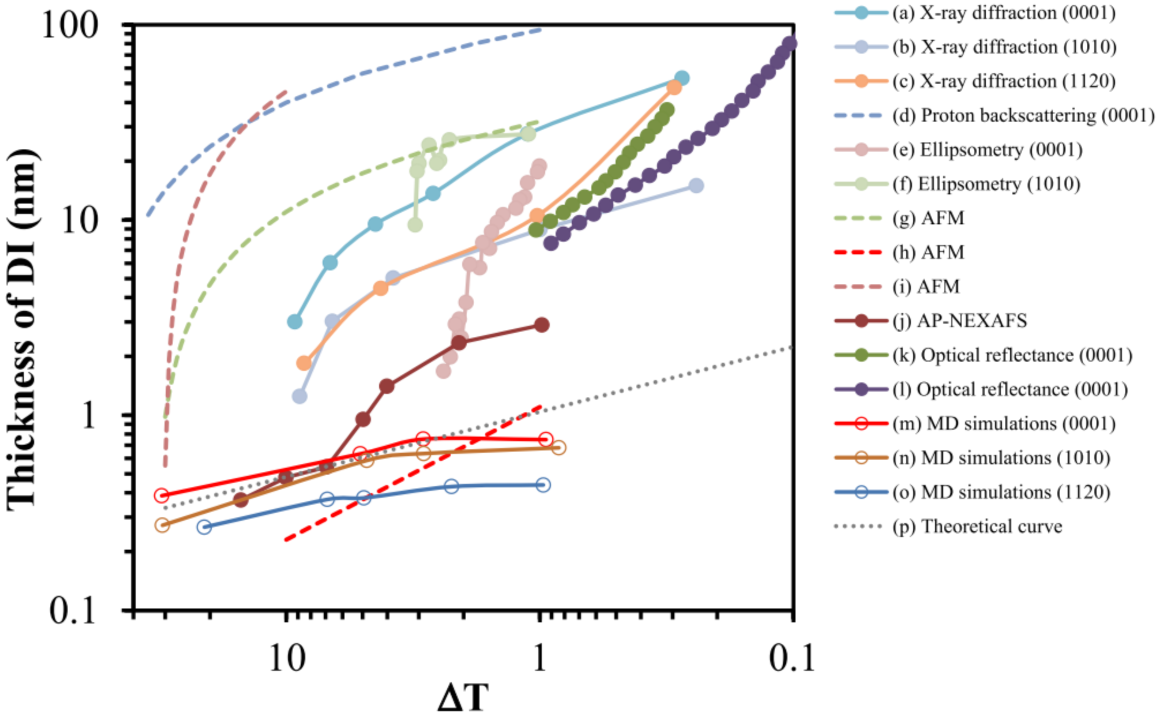

FIGURE 1.3: Comparison of different methods to derive the thickness of the QLL, or Disordered Interface (DI), as a function of the temperature difference to the melting point ($\Delta_T = T_m - T$). Taken from Bartels-Rausch et al. [16].

operating in velocity indentation mode, AFM gives a much smaller value (h). Recent AFM work, with careful consideration of the different artefacts, suggests a rather small value of the QLL thickness i.e. <1nm at -2°C [17]. Furthermore, the temperature calibration at the sample spot of the ice sample is delicate and impurities might be present in trace amounts, resulting in a thickening of the QLL. Finally, none of these methods probes the thickness directly, and depth calibration might thus be a further source of uncertainty. Figure 1.4 shows how the QLL develops with temperature, as seen from MD simulation [18].

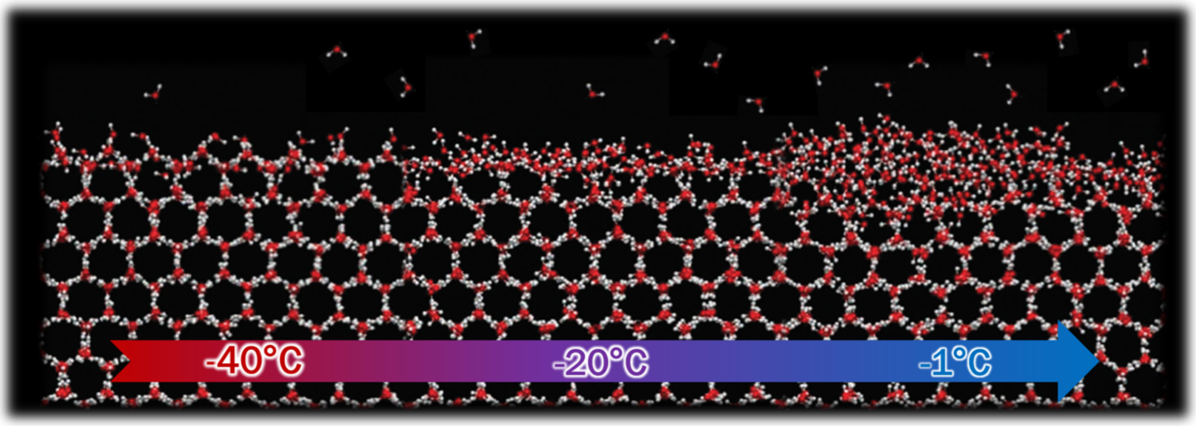

FIGURE 1.4: MD simulation of the surface of ice, showing the thickening of the QLL with increasing temperature. Adapted from [18]

Despite its small size, the QLL has large-scale consequences. For example, when an ice crystal collides with a warmer rimed particle[2], a net positive charge is transferred from the rimed particle (warmer ice surface) to the (colder) ice crystal due to the thermoelectric effect[3] which leads to cloud electrification [19]. If the QLL behaves as a liquid, its role here could be to enhance the charge transfer, by sticking to the colder surface during the collision.

---

[2] frozen supercooled water coating a particle

[3] protons (H^+) are more mobile than (OH^-)

In the mid 1980s, the ozone depletion observations have raised interest in understanding the interaction between trace gases such as HCl and ice. Using thermal analysis and FTIR spectroscopy to characterize the ice substrate, and mass spectrometry to measure the concentration of HCl and H_2O vapors in the gas phase, Abbatt et al. [20] have found that a liquid layer forms on the surface of the ice in the presence of HCl, even below the eutectic temperature (186 K). At HCl partial pressure that are commonly found in the stratosphere, HCl adsorbs on ice which increases its chemical reactivity. In particular, chlorine activation by heterogeneous reaction with $ClONO_2$ on the ice, reaction **1.2**, occurs efficiently and releases ozone-depleting reactive chlorine species.

$$\mathrm{HCl} + \mathrm{ClONO_2} \xrightarrow{\text{het.}} \mathrm{HNO_3} + \mathrm{Cl_2} \tag{1.2}$$

Reaction **1.2** happens on type II Polar stratospheric clouds (PSCs), consisting of ice particles (typically below $-80\,°\mathrm{C}$), and contributes to the formation of the ozone hole that is often observed in Antarctica. Ice can also act as a sink for the HCl reservoir, protecting the ozone from the chlorine catalytic cycle [21].

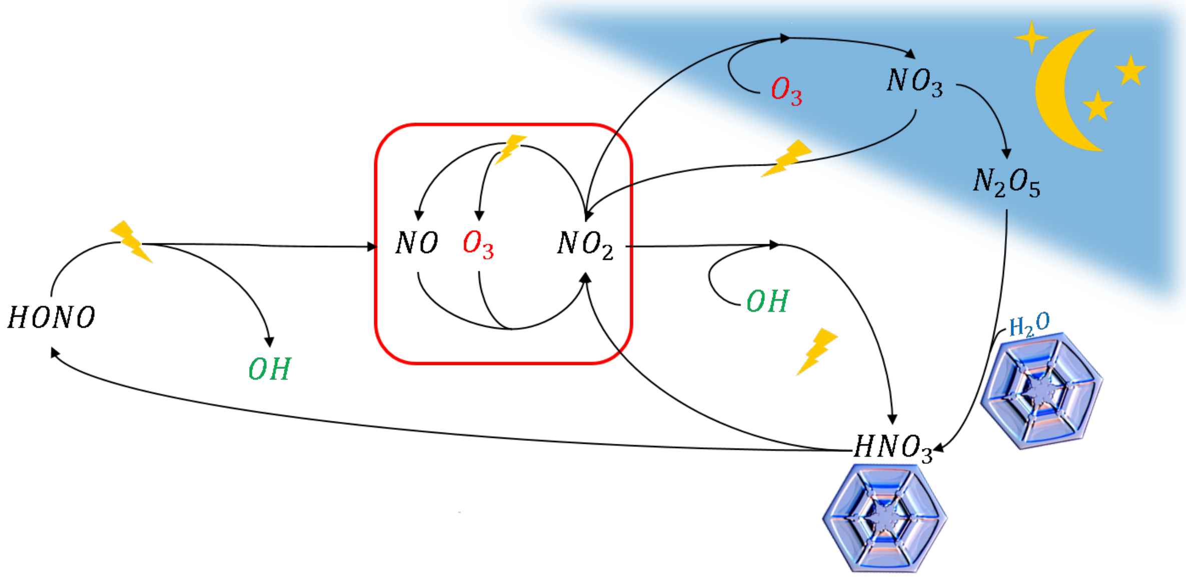

FIGURE 1.5: Nitrogen chemistry in a nutshell. The NO_x cycle indicated in red, determines the ozone concentration in the upper troposphere. Nighttime oxidation of NO_x by O_3 leads to the formation of N_2O_5 which can then form HNO_3 via hydrolysis on ice. Adsorbed HNO_3 or its dissociated nitrate ion can photolyze back to NO_2 or to HONO. HNO_3 is an acid so it remains strongly partitioned to the ice, and will eventually be washed away by precipitation of the ice. When the HNO_3 gas phase concentration decreases, it 'pulls' on the oxidation pathways and decreases NO_2 and O_3.

It is well known that the presence of impurities lowers the melting point of water. However, what does this imply for the QLL at the molecular level? Experimental

ellipsometry work shows that trace amounts of HCl are sufficient to induce a QLL on the ice surface, even at stratospheric temperatures (186-243K) [22]. The environmental implication for cirrus clouds in the troposphere is that the ice surfaces turn into a platform for halogen activation reactions and ozone depletion.
In addition, impurities have been suggested to increase the QLL thickness [22–27]. In particular strong acids have been found to have a strong impact on the QLL [24] whereas a weak acid needs to be more concentrated to show the same thickening [28]. In the preceding work to this project, [24], the fate of HCl on the surface of ice was investigated. The photoelectron spectroscopy data surprisingly shows that physisorbed and solvated HCl coexist at the surface of warm ice (-20°C), quite in contrast to expectations based on earlier work [29]. Using XPS, chloride was found up to 8 nm deep in the interfacial region, whereas the PEY-XAS data suggested a smaller thickness of the QLL (1-2 nm). Understanding this observation better is one goal of this project. While the adsorption of most volatile trace gases shows a negative temperature trend, the group of J. Crowley [30] recently discovered that HCl uptake on ice at [190-220K] was temperature independent. This is counter-intuitive at first sight. The author proposed that the apparent temperature trend was a combination of that of adsorption and dissociation.

We can differentiate ice-trace gas interactions in three categories:

1. Partitioning of gases to the ice. A prominant example is the partitioning of HNO_3 to the ice. The resulting loss in gas phase HNO_3 influences the equilibrium between NO and NO_2 which in turn decreases the ozone concentration as illustrated in Figure 1.5. Neu and Prather have observed a 30% decrease in ozone concentration in the presence of ice [31].

2. Chemical reaction of gases, for example reaction **1.2** discussed above.

3. Chemical reaction in the ice. For example, the photolysis of organics in snow from the cryosphere, resulting in the emission of aldehydes, thus influencing the oxidation capacity of the lowermost troposphere [32].

1.3 Amines

As we have seen in the previous section, the adsorption of acidic trace species on ice has been thoroughly investigated with respect to acid dissociation and the enhancement of the QLL [33–36]. However, only a few studies report on the interaction of ice with bases such as amines. Wernet, Nordlund et al. [37, 38] have reported that ammonia saturates the dangling OH on the surface of the ice, at 90K, and increases the coordination number of the HB network by ’pulling’ on these otherwise free OH groups. To extend the knowledge of the interaction of bases with the ice surface, we have decided to study the adsorption of hexylamine on ice under atmospheric conditions.

Amines are emitted from natural and anthropogenic sources such as the ocean, wildfires, livestock farming or rocket fuel burning [39]. In the continental boundary layer, ambient concentrations of aliphatic amines have been reported to be <0.025-0.35 ppb, in comparison to 25 ppb for ammonia [40]. While ammonia is the principal atmospheric base [41], the total amine mass has been measured to represent 14-23% that of ammonia [42] in the plume downwind of a cattle farm in California. Similarly to ammonia, aliphatic gaseous amines may neutralize atmospheric acids and transition from the gas to the particle phase by forming alkyl-ammonium salts. In the gas phase, amines undergo rapid oxidation reactions (mostly with OH radical, lifetime on the order of hours), contributing to secondary organic aerosol formation. Together with ammonia, amines substantially contribute to the formation of particulate matter. Their gas phase degradation products, mostly via photolysis or further OH attack [39, 43] include HCN, which is poisonous, and the long-lived N$_2$O, which is a greenhouse gas and an ozone-depleting substance (ODS) [39]. Amines are rather inert in the condensed phase [39], even though the conjugated ammonium ions are involved in aqueous phase secondary chemistry leading to the formation of nitrogen-containing organic products [44, 45].

The main application of amines in the industry is for CO$_2$ capture. Figure Figure 1.6 illustrate how the amine functional group of ethanolamine reacts with CO$_2$ from the exhaust of a power plant and allows capturing it i.e. from the gas phase to a condensed phase. A carbon capture and storage (CCS) unit, such as the one in Kårstø, Norway, emits about 1-4 ppm of amines, 2-10 ppm of NOx and 1-5 ppm of NH3 for a total of 4-20 ppm of nitrogen-containing molecules. To collect 1 million tonnes CO$_2$, the unit

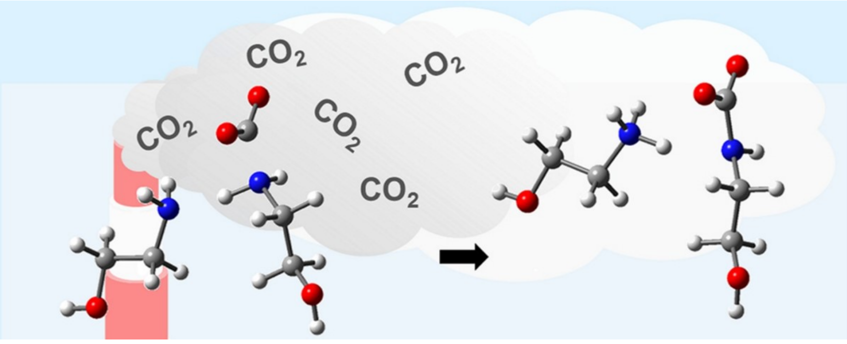

Figure 1.6: Illustration of the carbon capture process. Taken from [46]

filters 40 million tonnes of exhaust gas (hence decreasing CO_2 concentration by 2.5%), and for every 25'000 tonnes of CO_2 captured, 1 tonne of amine is emitted [47]. Nitrogen emissions may acidify surface water and lead to the eutrophication of terrestrial ecosystems [48].

Hexylamine (HA) is a medium tail-size aliphatic amine, with 6 carbon and 1 nitrogen as shown in Figure 1.7. While the nitrogen headgroup is hydrophilic, the aliphatic tail is hydrophobic, thus such molecule has the tendency to be located at the interface between water (liquid or solid) and the air and it is a good candidate for a surface science experiment. HA is not particularly abundant in the atmosphere, but it is a good representative of the amine family, which is very diverse. The vapor pressure p^0 and the Henry's law constant K_H both at 298.15 K (taken from the Supporting info in [49]) are shown in Table 1.1 together with other properties.

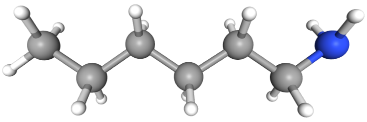

FIGURE 1.7

TABLE 1.1: Selected physical properties for hexylamine.

p^0 (298.15 K)	11.5 mbar
K_H (298.15 K)	37.5 M atm^{-1}
Molar mass	101.193 g mol^{-1}
Density	0.77 g cm^{-3}
Melting point	23.4 °C
Boiling point	131.5 °C
Solubility in water (20 °C)	12 g/L (20 °C)

1.4 ELECTRON SPECTROSCOPY

In order to study the QLL and the adsorption of trace gases, we need a surface science approach. Different techniques are available to study the ice surface and its interaction with trace gases. Neutron scattering interacts with the hydrogen nuclei on the surface and provides information about the structural properties of the water coordination as well as the radial distribution function [50]. On ice, it is sensitive to the first layer of hydrogen atoms. Sum frequency generation (SFG) is a nonlinear optical process in which two input photons generate a new photon whose energy is the sum of the two input photon energies. SFG provides information at the interface between two isotropic media and therefore it is only sensitive to the interfacial molecules. The QLL has been studied using this method [51]. A technique complementary to SFG and neutron scattering is electron spectroscopy (introduced in more detail below). The technique uses an electron analyzer to measure electrons emitted by the sample when excited by a high-energy beam such as X-ray radiation. The very short inelastic mean free path (IMFP) of electrons in matter, of the order of a nanometer, confer the surface sensitivity to the technique, however, the probing depth in this technique is still more bulk-oriented compared to neutron scattering and SFG, but in turn, also covers of expected thicknesses of the QLL.

1.4.1 *XPS*

X-ray Photoelectron Spectroscopy (XPS) is a surface-sensitive technique based on the photoelectric effect: when an electron absorbs a X-ray photon and gains enough energy to escape the surface. Because electrons interact strongly with matter, they have a very short IMFP, typically 1 nm for electrons with kinetic energy (KE_e) of 100 eV traveling in water. The IMFP is mostly sensitive to the density of the material in which it travels and relatively independent of its nature. The IMFP increases with increasing KE_e such that at KE_e =500 eV, the IMFP is closer to 2 nm. XPS provides us with chemically selective surface composition information. This includes elemental composition, relative surface concentrations and an estimate of their density profile with depth [36, 52, 53], but also probing the electronic configuration of an element such as the oxidation state of carbon in adventitious carbon. Likewise, XPS can probe the degree of protonation of acids or bases, specifically also for amines via resolving $R{-}NH_2$ and $R{-}NH_3^+$ from a deconvolution of the N 1s peak as shown on Figure 1.8 [54]. XPS spectra are obtained from measuring the kinetic energy, KE_e , of photoelectrons emitted via the photoelectric effect upon X-ray irradiation. The spectrum in Figure 1.9a, shows an example of XPS data obtained at a photon energy E_{ph} =1000 eV. From the positions of the two features present on this spectrum, we are able to calculate the apparent binding energy of the probed element:

$$BE = E_{ph} - KE_e \tag{1.3}$$

in the present case, we find BE=539.2 and 537.4 eV that we can identify to be the apparent binding energy of the O 1s in gas phase water and condensed phase water, respectively. The binding energy difference between the gas phase and the condensed phase arises from the fact that the (isolated) gas phase molecule gains a positive charge when the photoelectron leaves the molecule, increasing its binding energy while in the condensed phase, the positive charge induced by the core hole is screened by the neighboring molecules [55]. In addition, the broader distribution of electronic configurations within the neighboring water molecules leads to a distribution of slightly different binding energies, increasing the width of the photoemission peak of the condensed phase [55].

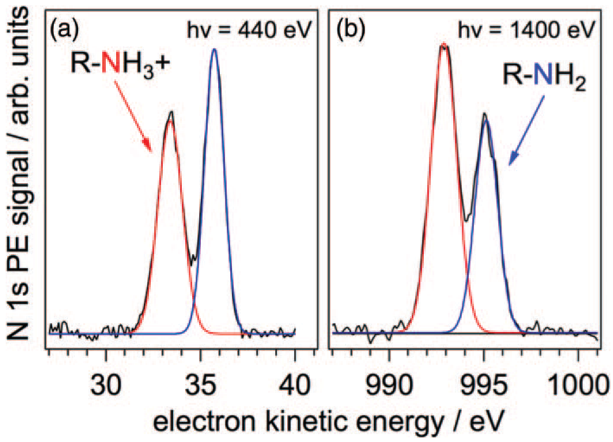

FIGURE 1.8: Liquid jet N 1s spectra of the surface of a butylamine solution at pH=pKa, acquired at photon energies (a) 440 eV and (b) 1400 eV. The measurement at 440 eV (a) is more sensitive that the one at 1400 eV (b) because electrons at 35 eV have a lower IMFP than electrons at 995 eV. Taken from [54].

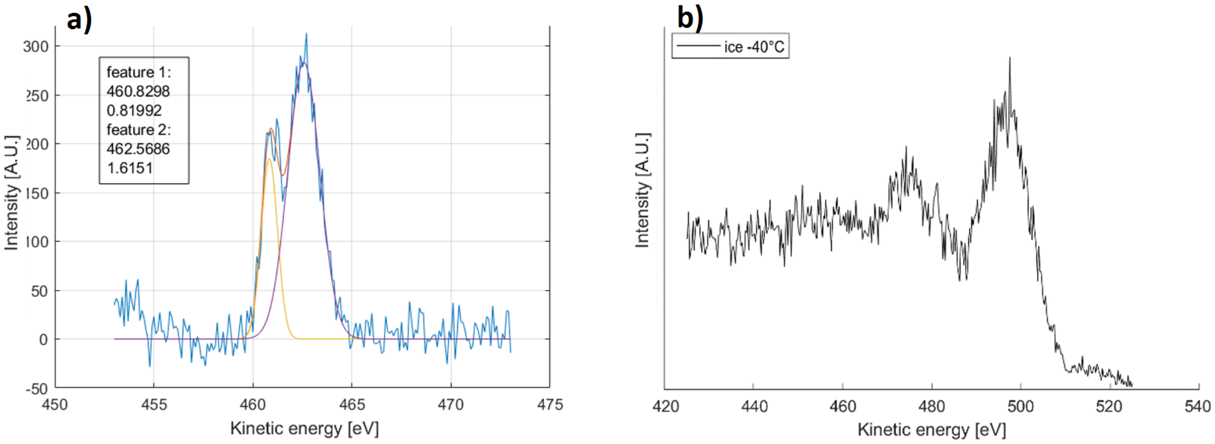

FIGURE 1.9: a): O 1s X-ray photoelectron spectrum of ice at -2.5°C measured at E_{ph} =1000 eV, fitted with 2 Gaussians (position and width are detailed in the textbox). The feature on the low kinetic energy side is attributed to the gas phase water and the feature on the high kinetic energy side is ice. b): O K edge Auger emission spectrum of ice at -40°C, taken at 536 eV excitation energy.

1.4.2 *XAS and PEY-XAS*

X-ray absorption spectroscopy (XAS) takes advantage of the resonant transitions between the core electron level, O 1s in this case, and the lowermost unoccupied orbitals, and allow to probe their density of states (DOS). The core hole is then filled with electrons from valence orbitals and the energy released from this decay is emitted either as a fluorescence photon or as a so-called Auger-Meitner electron emitted from one of the valence orbitals as shown on Figure 1.10. Figure 1.9b shows the Auger spectra of ice at -40°C measured with E_{ph} =536 eV. This spectrum is composed of primary Auger emission peaks (broad features at 500 eV and 475 eV) within a large background. In electron yield (EY-XAS) or partial electron yield (PEY-XAS) mode (meaning, the emitted electrons are measured and not the fluorescence/transmitted photons), the measurement is very surface sensitive due to the short inelastic mean free path (IMFP, mean distance between 2 inelastic scattering events) of about 2 nm for electrons with a kinetic energy of about 500 eV traveling in liquid water [56].

In ice and liquid water, the short intermolecular distances and hydrogen bonds distort the molecular orbitals, or since we are talking about condensed phases, band structure (figure 13 in [57] and text below). Therefore, XAS is sensitive to the hydrogen-bonding (HB) configuration, and through calibration with pure liquid water (distorted HB network) and clean cold ice (tetrahedral HB network) references, we can measure the distortion in the HB network on the ice surface at different temperature and with different surface coverages of a trace species.

Since the pioneering work by Bluhm, many improvements have been made in measuring and interpreting the XAS spectrum of ice [57–60]. However, the effective probing depth in PEY-XAS is a key uncertainty due to the scattering of Auger electrons. Indeed, in PEY-XAS, only part of the Auger electrons are detected, based on their kinetic energy. The detection range, which we also called the kinetic energy window (KE window), is often situated on the tail of the Auger spectra (example of O KLL Auger spectra in Figure 1.9b), therefore measuring mostly secondary electrons (primary Auger-Meitner electrons that have scattered inelastically). As we will see later, the uncertainty related to electron scattering in PEY-XAS is more important than the uncertainty directly linked to the uncertainty in the IMFP.

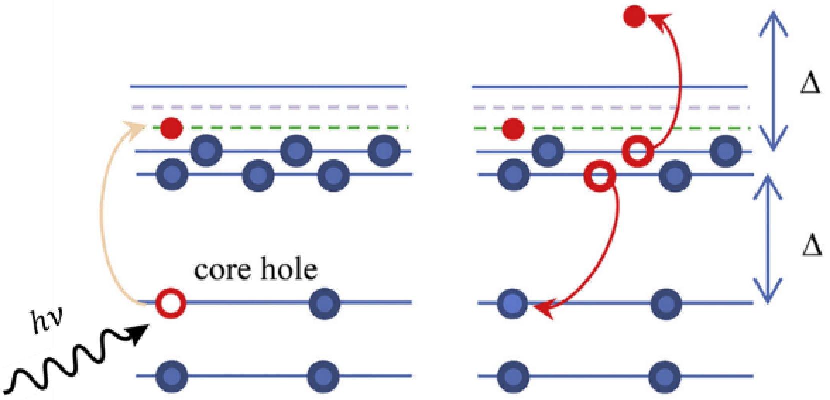

FIGURE 1.10: Illustration of an Auger emission following the promotion of an electron to the LUMO. Adapted from [56].

1.4.3 *ISS beamline*

The solid-gas interface chamber [61] at the in situ spectroscopy beamline (Swiss Light Source, Paul Scherrer Institute) is capable to operate in near-ambient pressure, allowing the study of samples in environmental conditions when traditional electron spectroscopy chambers have to operate in UHV. It is possible, for example, to measure ice in equilibrium with its vapor pressure, in the whole temperature range of its stability domain. The analyzer's detector operates in ultra-high vacuum (UHV) therefore, an aperture and a differential pumping set-up are required to connect the electron analyzer to the near ambient pressure chamber (few mbar).

Figure 1.11 shows a sketch of the sample holder inserted in the experimental chamber (top view). This sample holder has improved geometry compared to [61] that allows the coldest spot to be well centered and localized right in front of the cone aperture. The cooling efficiency is also increased and the sample can easily be cooled to less than -100 °C. We grow the ice samples by vapor deposition on this gold-coated plate cooled by a stream of N_2 gas. From the gas flux induced by the differential pumping, a low-pressure sphere with gradually increasing pressure, reaching around 99% at two times the aperture diameter, is created around the cone [58]. The property of ice to dynamically respond to pressure change is an advantage for us because it guarantees that the relative humidity at the sample spot is in equilibrium during the measurements. We have successfully maintained ice stable for 10-12 hours, as seen with the XPS intensity trend of the surface of the ice: ice that is not in thermodynamic equilibrium with the partial pressure of water either evaporates or grows. Both would lead to changes in the distance between the ice surface and the analyzer's electron inlet. Because this working distance has a strong impact on the signal intensity, the area of the O 1s photoemission signal is a good indicator of the fluctuation at the surface.

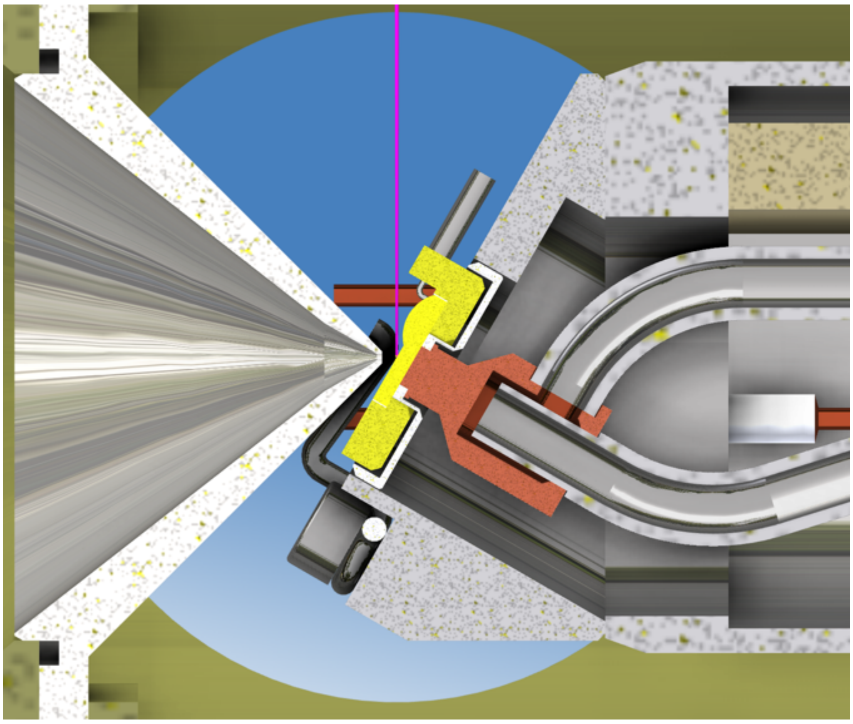

FIGURE 1.11: Top view of the sample holder inserted in the experimental chamber (blue circle). The cone of the electron analyzer is shown on the left, the X-ray beam is shown as a pink line, and the sample plate is shown in yellow in front of the cone. The cold finger is shown in red and touches the sample plate. We can see the tubings of the cold N_2 gas in the main body of the cryo-holder. We see in white the complex soldering structure sealing the cryo-holder. The sample is directly placed on a gold-covered Pt1000 sensor (resistance thermometer, shown in bright yellow) which is built into the sample plate. The cone aperture is 0.5 mm.

1.5 THESIS OUTLINE

This thesis tackles the mechanisms involved in the interactions between ice and trace gases. The focus is placed on the QLL and a careful assessment of the method (XPS and PEY-XAS) to ensure a sound interpretation of the results. The goal of the thesis is to understand how the properties of the QLL affect the adsorption and dissociation of a base such as hexylamine. This would provide insight into the proton availability at the surface of the ice and tackles the topic of acid/base chemistry on solids. The adsorption process to predict the partitioning of trace gases to ice in the atmosphere has been extensively investigated with different acids [16] however, we lack experimental data about bases, and this thesis aims at filling this gap.

1.5.1 *Chapter 1: Introduction*

This first chapter introduces ice and its special importance in the environment, provide context regarding the research background of the ice-trace gas interaction and provides an overview of the experimental techniques that I have used to study ice.

1.5.2 *Chapter 2: Second order light*

This chapter provides a characterization of the synchrotron beamline used in the present thesis and evaluates the impact of second-order light on the XPS and XAS measurements. The second-order light contributes to the systematic overestimation of the photon flux via photodiode measurement and therefore, it contributes to the uncertainty not only in PEY-XAS, but also in XPS and especially in XPS depth profiles.

1.5.3 *Chapter 3: The premelting of ice revisited with X-ray absorption spectroscopy*

The first project of this thesis was to study the premelting of pure ice using PEY-XAS and get a database of ice measurements. The goal is to develop a detailed understanding of the probing depth of PEY-XAS, and to assess the role of electron scattering. Uncertainties related to the experiment are investigated and corrected, whenever possible. we take advantage of the recent advances in the PEY-XAS technique, in order to revisit the on-set temperature and thickness of the QLL. This first project will be published as: Gabathuler, J. P., Yang, H., Manoharan, Y., Boucly, A., Alpert, P. A., Artiglia, L., Bartels-Rausch, T. & Ammann, M. "The premelting of ice revisited with X-ray absorption spectroscopy" (in preparation)

1.5.4 *Chapter 4: Adsorption of Hexylamine on ice, as seen by near ambient pressure XPS*

Looking into the adsorption of an amine allows us to broaden our understanding of the response of the ice surface to bases and to contribute to the question of interfacial acidity. Choosing the surface active hexylamine (HA), a medium tail-size aliphatic amine as an example, thus allows us to investigate the effect of the presence of the amine just at the interface, without significant burial into the top ice layers, as it could possibly be the case with ammonia. In addition, hexylamine doesn't contain oxygen, which is very convenient because HA will not interfere with the oxygen PEY-XAS or XPS measurement, as it could be the case for other trace species of interest such as HNO_3. This second project will be published as: Gabathuler, J. P., Manoharan, Y., Artiglia, L. & Ammann, M. "Adsorption of Hexylamine on ice, as seen by near ambient pressure XPS" (in preparation)

1.5.5 *Chapter 5: Additional experiments*

This chapter is dedicated to several additional works that I have done during my Ph.D. and are relevant to the thesis. This includes a study of the surface disorder as a function of temperature in liquid water, a proof of principle of the PEY-XAS depth profile which is an application of the Monte Carlo simulation presented in the QLL paper, and finally, a study of the direct impact of total pressure on the QLL. None of these studies are complete enough to constitute a publication however, they present great results and open new insights for future experiments.

REFERENCES

1. Hasted, J. *Liquid water: Dielectric properties* 255–309 (Springer, 1972).
2. Cook, R. L., De Lucia, F. C. & Helminger, P. "Molecular force field and structure of water: Recent microwave results". *Journal of Molecular Spectroscopy* **53**, 62–76 (1974).
3. Powles, J. "The structure of the water molecule in liquid water". *Molecular Physics* **42**, 757–765 (1981).
4. Brini, E., Fennell, C. J., Fernandez-Serra, M., Hribar-Lee, B., Luksic, M. & Dill, K. A. "How Water's Properties Are Encoded in Its Molecular Structure and Energies". *Chemical Reviews* **117**, 12385–12414 (2017).
5. Nonomura, Y., Saito, R. & Takahashi, A. "Friction at fingertip surface during water contact process". *Bulletin of the Chemical Society of Japan* **88**, 949–954 (2015).
6. Galamba, N. "On the hydrogen-bond network and the non-Arrhenius transport properties of water". *Journal of Physics: Condensed Matter* **29**, 015101 (2016).
7. Chaplin, M. *Water Structure and Science* `https://water.lsbu.ac.uk/water/`.
8. Bartels-Rausch, T. "Ten things we need to know about ice and snow". *Nature* **494**, 27–29 (2013).
9. Dash, J. G., Fu, H. Y. & Wettlaufer, J. S. "The Premelting of Ice and Its Environmental Consequences". *Reports on Progress in Physics* **58**, 115–167 (1995).
10. Libbrecht, K. G. "Physical Dynamics of Ice Crystal Growth". *Annual Review of Materials Research* **47**, 271–295 (2017).
11. Libbrecht, K. G. "An experimental apparatus for observing deterministic structure formation in plate-on-pedestal ice crystal growth". *arXiv preprint arXiv:1503.01019* (2015).
12. Libbrecht, K. G. *Snow crystals* `www.snowcrystals.com`.
13. Kietzig, A.-M., Hatzikiriakos, S. & Englezos, P. *Physics of ice friction* 081101–081101 (2010).
14. Joly, J. "The phenomena of skating and Professor J. Tomson's thermodynamic relation". *Scientific Proceeding of the Royal Dublin Society, New Series* **5**, 453–454 (1887).
15. Dash, J. G., Rempel, A. W. & Wettlaufer, J. S. "The physics of premelted ice and its geophysical consequences". *Reviews of Modern Physics* **78**, 695–741 (2006).
16. Bartels-Rausch, T., Jacobi, H. W., Kahan, T. F., Thomas, J. L., Thomson, E. S., Abbatt, J. P. D., Ammann, M., Blackford, J. R., Bluhm, H., Boxe, C., Domine, F., Frey, M. M., Gladich, I., Guzman, M. I., Heger, D., Huthwelker, T., Klan, P., Kuhs, W. F., Kuo, M. H., Maus, S., Moussa, S. G., McNeill, V. F., Newberg, J. T., Pettersson, J. B. C., Roeselova, M. & Sodeau, J. R. "A review of air-ice chemical and physical interactions (AICI): liquids, quasi-liquids, and solids in snow". *Atmospheric Chemistry and Physics* **14**, 1587–1633 (2014).

17. Constantin, J. G., Gianetti, M. M., Longinotti, M. P. & Corti, H. R. "The quasi-liquid layer of ice revisited: the role of temperature gradients and tip chemistry in AFM studies". *Atmospheric Chemistry and Physics* **18**, 14965–14978 (2018).
18. Gladich, I., Pfalzgraff, W., Marsalek, O., Jungwirth, P., Roeselova, M. & Neshyba, S. "Arrhenius analysis of anisotropic surface self-diffusion on the prismatic facet of ice". *Physical Chemistry Chemical Physics* **13**, 19960–19969 (2011).
19. Wang, P. K. *Physics and dynamics of clouds and precipitation* (Cambridge University Press, 2013).
20. Abbatt, J., Beyer, K., Fucaloro, A., McMahon, J., Wooldridge, P., Zhang, R. & Molina, M. "Interaction of HCl vapor with water-ice: Implications for the stratosphere". *Journal of Geophysical Research: Atmospheres* **97**, 15819–15826 (1992).
21. Seinfeld, J. H. & Pandis, S. N. *Atmospheric Chemistry and Physics: From Air Pollution to Climate Change* p.181 (1998).
22. McNeill, V. F., Loerting, T., Geiger, F. M., Trout, B. L. & Molina, M. J. "Hydrogen chloride-induced surface disordering on ice". *Proceedings of the National Academy of Sciences of the United States of America* **103**, 9422–9427 (2006).
23. Huthwelker, T., Ammann, M. & Peter, T. "The Uptake of Acidic Gases on Ice". *Chemical Reviews* **106**, 1375–1444 (2006).
24. Kong, X., Waldner, A., Orlando, F., Artiglia, L., Huthwelker, T., Ammann, M. & Bartels-Rausch, T. "Coexistence of Physisorbed and Solvated HCl at Warm Ice Surfaces". *J Phys Chem Lett* **8**, 4757–4762 (2017).
25. Moussa, S. G., Kuo, M. H. & McNeill, V. F. "Nitric acid-induced surface disordering on ice". *Physical Chemistry Chemical Physics* **15**, 10989–10995 (2013).
26. Pouvesle, N., Kippenberger, M., Schuster, G. & Crowley, J. N. "The interaction of H2O2 with ice surfaces between 203 and 233 K". *Physical Chemistry Chemical Physics* **12**, 15544–15550 (2010).
27. Wettlaufer, J. S. "Impurity effects in the premelting of ice". *Physical Review Letters* **82**, 2516–2519 (1999).
28. Krepelova, A., Bartels-Rausch, T., Brown, M. A., Bluhm, H. & Ammann, M. "Adsorption of Acetic Acid on Ice Studied by Ambient-Pressure XPS and Partial-Electron-Yield NEXAFS Spectroscopy at 230-240 K". *Journal of Physical Chemistry A* **117**, 401–409 (2013).
29. Devlin, J. P. & Kang, H. "Comment on "HCl adsorption on ice at low temperature: a combined X-ray absorption, photoemission and infrared study" by P. Parent, J. Lasne, G. Marcotte and C. Laffon, Phys. Chem. Chem. Phys., 2011, 13, 7142". *Physical Chemistry Chemical Physics* **14**, 1048–1049 (2012).
30. Zimmermann, S., Kippenberger, M., Schuster, G. & Crowley, J. N. "Adsorption isotherms for hydrogen chloride (HCl) on ice surfaces between 190 and 220 K". *Physical Chemistry Chemical Physics* **18**, 13799–13810 (2016).

31. Neu, J. & Prather, M. "Toward a more physical representation of precipitation scavenging in global chemistry models: cloud overlap and ice physics and their impact on tropospheric ozone". *Atmospheric Chemistry and Physics* **12**, 3289–3310 (2012).

32. Dominé, F. & Shepson, P. B. "Air-snow interactions and atmospheric chemistry". *Science* **297**, 1506–1510 (2002).

33. Kong, X., Waldner, A., Orlando, F., Artiglia, L., Huthwelker, T., Ammann, M. & Bartels-Rausch, T. "Coexistence of Physisorbed and Solvated HCl at Warm Ice Surfaces". *J Phys Chem Lett* **8**, 4757–4762 (2017).

34. Bartels-Rausch, T., Orlando, F., Kong, X., Artiglia, L. & Ammann, M. "Experimental Evidence for the Formation of Solvation Shells by Soluble Species at a Nonuniform Air–Ice Interface". *ACS Earth and Space Chemistry* **1**, 572–579 (2017).

35. Krepelova, A., Newberg, J. T., Huthwelker, T., Bluhm, H. & Ammann, M. "The nature of nitrate at the ice surface studied by XPS and NEXAFS". *Physical Chemistry Chemical Physics* **12**, 8870–8880 (2010).

36. Krepelova, A., Bartels-Rausch, T., Brown, M. A., Bluhm, H. & Ammann, M. "Adsorption of Acetic Acid on Ice Studied by Ambient-Pressure XPS and Partial-Electron-Yield NEXAFS Spectroscopy at 230-240 K". *Journal of Physical Chemistry A* **117**, 401–409 (2013).

37. Wernet, P., Nordlund, D., Bergmann, U., Cavalleri, M., Odelius, M., Ogasawara, H., Näslund, L. Å., Hirsch, T. K., Ojamäe, L., Glatzel, P., Pettersson, L. G. M. & Nilsson, A. "The Structure of the First Coordination Shell in Liquid Water". *Science* **304**, 995–999 (2004).

38. Nordlund, D., Ogasawara, H., Wernet, P., Nyberg, M., Odelius, M., Pettersson, L. & Nilsson, A. "Surface structure of thin ice films". *Chemical physics letters* **395**, 161–165 (2004).

39. Ge, X., Wexler, A. S. & Clegg, S. L. "Atmospheric amines – Part I. A review". *Atmospheric Environment* **45**, 524–546 (2011).

40. Cornell, S., Jickells, T., Cape, J., Rowland, A. & Duce, R. "Organic nitrogen deposition on land and coastal environments: a review of methods and data". *Atmospheric Environment* **37**, 2173–2191 (2003).

41. Tanner, R. L. in *Acidic precipitation* 1–19 (Springer, 1990).

42. Sorooshian, A., Murphy, S. M., Hersey, S., Gates, H., Padro, L. T., Nenes, A., Brechtel, F. J., Jonsson, H., Flagan, R. C. & Seinfeld, J. H. "Comprehensive airborne characterization of aerosol from a major bovine source". *Atmos. Chem. Phys.* **8**, 5489–5520 (2008).

43. Carl, S. A. & Crowley, J. N. "Sequential Two (Blue) Photon Absorption by NO2 in the Presence of H2 as a Source of OH in Pulsed Photolysis Kinetic Studies: Rate Constants for Reaction of OH with CH3NH2, (CH3)2NH, (CH3)3N, and C2H5NH2 at 295 K". *The Journal of Physical Chemistry A* **102**, 8131–8141 (1998).

44. Noziere, B., Dziedzic, P. & Córdova, A. "Products and kinetics of the liquid-phase reaction of glyoxal catalyzed by ammonium ions (NH4+)". *The Journal of Physical Chemistry A* **113**, 231–237 (2009).

45. Galloway, M. M., Chhabra, P. S., Chan, A. W. H., Surratt, J. D., Flagan, R. C., Seinfeld, J. H. & Keutsch, F. N. "Glyoxal uptake on ammonium sulphate seed aerosol: reaction products and reversibility of uptake under dark and irradiated conditions". *Atmospheric Chemistry and Physics* **9**, 3331–3345 (2009).

46. Kim, S., Shi, H. & Lee, J. Y. "CO2 absorption mechanism in amine solvents and enhancement of CO2 capture capability in blended amine solvent". *International Journal of Greenhouse Gas Control* **45**, 181–188 (2016).

47. Knudsen, S., Karl, M. & Randall, S. "Summary report: Amine emissions to air during carbon capture. Phase I: CO2 and amines screening study for effects to the environment." *NILU OR* (2009).

48. Karl, M., Brooks, S., Wright, R. & Knudsen, S. "Amines worst case studies. Worst case studies on amine emissions from CO2 capture plants (Task 6)." *NILU OR* (2008).

49. Ge, X., Wexler, A. S. & Clegg, S. L. "Atmospheric amines – Part II. Thermodynamic properties and gas/particle partitioning". *Atmospheric Environment* **45**, 561–577 (2011).

50. Head-Gordon, T. & Hura, G. "Water structure from scattering experiments and simulation". *Chemical reviews* **102**, 2651–2670 (2002).

51. Sanchez, M. A., Kling, T., Ishiyama, T., van Zadel, M. J., Bisson, P. J., Mezger, M., Jochum, M. N., Cyran, J. D., Smit, W. J., Bakker, H. J., Shultz, M. J., Morita, A., Donadio, D., Nagata, Y., Bonn, M. & Backus, E. H. G. "Experimental and theoretical evidence for bilayer-by-bilayer surface melting of crystalline ice". *Proceedings of the National Academy of Sciences of the United States of America* **114**, 227–232 (2017).

52. Waldner, A., Artiglia, L., Kong, X. R., Orlando, F., Huthwelker, T., Ammann, M. & Bartels-Rausch, T. "Pre-melting and the adsorption of formic acid at the air-ice interface at 253 K as seen by NEXAFS and XPS". *Physical Chemistry Chemical Physics* **20**, 24408–24417 (2018).

53. Bartels-Rausch, T., Orlando, F., Kong, X., Artiglia, L. & Ammann, M. "Experimental Evidence for the Formation of Solvation Shells by Soluble Species at a Nonuniform Air–Ice Interface". *ACS Earth and Space Chemistry* **1**, 572–579 (2017).

54. Brown, M. A., Redondo, A. B., Jordan, I., Duyckaerts, N., Lee, M.-T., Ammann, M., Nolting, F., Kleibert, A., Huthwelker, T., Mächler, J.-P., Birrer, M., Honegger, J., Wetter, R., Wörner, H. J. & Bokhoven, J. A. v. "A new endstation at the Swiss Light Source for ultraviolet photoelectron spectroscopy, X-ray photoelectron spectroscopy, and X-ray absorption spectroscopy measurements of liquid solutions". *Review of Scientific Instruments* **84**, 073904 (2013).

55. Fransson, T., Harada, Y., Kosugi, N., Besley, N. A., Winter, B., Rehr, J. J., Pettersson, L. G. M. & Nilsson, A. "X-ray and Electron Spectroscopy of Water". *Chemical Reviews* **116**, 7551–7569 (2016).

56. Ammann, M., Artiglia, L. & Bartels-Rausch, T. in *Physical Chemistry of Gas-Liquid Interfaces* (eds Faust, J. A. & House, J. E.) 135–166 (Elsevier, 2018).

57. Nilsson, A., Nordlund, D., Waluyo, I., Huang, N., Ogasawara, H., Kaya, S., Bergmann, U., Naslund, L. A., Ostrom, H., Wernet, P., Andersson, K. J., Schiros, T. & Pettersson, L. G. M. "X-ray absorption spectroscopy and X-ray Raman scattering of water and ice; an experimental view". *Journal of Electron Spectroscopy and Related Phenomena* **177**, 99–129 (2010).

58. Bluhm, H. "Photoelectron spectroscopy of surfaces under humid conditions". *Journal of Electron Spectroscopy and Related Phenomena* **177**, 71–84 (2010).

59. Frank Ogletree, D., Bluhm, H., Hebenstreit, E. D. & Salmeron, M. "Photoelectron spectroscopy under ambient pressure and temperature conditions". *Nuclear Instruments and Methods in Physics Research Section A: Accelerators, Spectrometers, Detectors and Associated Equipment* **601**, 151–160 (2009).

60. Niskanen, J., Fondell, M., Sahle, C. J., Eckert, S., Jay, R. M., Gilmore, K., Pietzsch, A., Dantz, M., Lu, X., McNally, D. E., Schmitt, T., Vaz da Cruz, V., Kimberg, V., Gel'mukhanov, F. & Föhlisch, A. "Compatibility of quantitative X-ray spectroscopy with continuous distribution models of water at ambient conditions". *Proceedings of the National Academy of Sciences* **116**, 4058–4063 (2019).

61. Orlando, F., Waldner, A., Bartels-Rausch, T., Birrer, M., Kato, S., Lee, M. T., Proff, C., Huthwelker, T., Kleibert, A., van Bokhoven, J. & Ammann, M. "The Environmental Photochemistry of Oxide Surfaces and the Nature of Frozen Salt Solutions: A New in Situ XPS Approach". *Topics in Catalysis* **59**, 591–604 (2016).

62. Gabathuler, J. P., Yang, H., Manoharan, Y., Boucly, A., Alpert, P. A., Artiglia, L., Bartels-Rausch, T. & Ammann, M. "The premelting of ice revisited with X-ray absorption spectroscopy" (in preparation).

63. Gabathuler, J. P., Manoharan, Y., Artiglia, L. & Ammann, M. "Adsorption of Hexylamine on ice, as seen by near ambient pressure XPS" (in preparation).

2

SECOND ORDER LIGHT

2.1 Higher-order light

2.1.1 *Background*

The original idea of this project was to study the transmission function of the electron analyzer which is one of the factors affecting the measurement of the count rate of electrons as a function of the kinetic energy. The transmission function is the efficiency at which the electron analyzer measures emitted electrons. This efficiency is far from 100%, because most emitted electrons are scattered and absorbed in the sample, and among those that escape the sample, only those that are within the acceptance angle of the electron analyzer will be measured. In addition, it is possible that electrons at different kinetic energies yield a different count rate when all other parameters are unchanged. This may be particularly detrimental when performing depth profiles, which are conducted by using electrons with different energies over a large range, i.e. from 300 to 1500 eV to probe a smaller or larger depth, respectively, into the surface of a material. Furthermore, depth profiles rely on the normalization of electron intensity signals to the bulk substrate, such as water and ice, to extract information on surfactant or ionic compounds. Binding energies of oxygen from water will be different from, e.g. carbon atoms coating or sitting on the surface. Changing the electron kinetic energy (by altering photon energy) will change photoelectron energy and normalization factors at 2 different probing depths can be different.

Indeed, the shape of a depth profile, usually shown as peak intensity as a function of kinetic energy, could be affected by this difference in electron transfer efficiency causing inconsistency between different data sets. Therefore, the transmission function could be a limiting factor when reproducing depth profiles.

In this work, the transmission function of the analyzer was determined using the ratio of the 4d and 4f orbitals in a gold sample, for kinetic energies ranging from 282 to 950 eV, at pass energy 20 and 50 eV, and slits (0.9/0.9). The binding energies of Au 4d, and Au 4f are 335, and 84 eV, respectively. Hence, to measure the range of KE previously mentioned, we use a photon energy ranging from 617 to 1285 eV for the Au 4d and from 366 to 1034 eV for the Au 4f. With increasing kinetic energy, the electrons have a higher IMFP, and the probing depth is larger. This procedure is standard when deriving a depth profile. The key to this measurement is the gold sample having a constant ratio of 4d and 4f with depth. After normalizing for photon flux and cross-section, the ratio should be 1, independent of the kinetic energy. Figure 2.1 shows the ratio as a function of electron kinetic energy deviated from a value of 1.0. In blue, the ratio was measured with pass energy (PE) 50 eV, and normalized to the photon flux (ϕ_{ph}) and to the cross-section (CS). The data in red shows the same analysis but with pass energy of 20 eV. In yellow, the same data as for the blue curve has beed normalized to the total cross section (CS-TOT). The general formula of the total cross section for linearly polarized light for the measurement geometry that we have at the ISS beamline is described by equation Equation 2.1:

$$\sigma_T(h\nu) = \sigma(h\nu) \cdot \frac{1+\beta(h\nu)}{4\pi} \tag{2.1}$$

where σ_T is the total cross-section, σ is the cross-section that we used in the blue and red curves, and β is the asymmetry parameter. These 3 ways of normalizing are performed to disentangle any impact of the pass energy or the total cross-section in the gold depth profile. Both cross-section and asymmetry parameter data were retrieved from the Trieste synchrotron website [1] based on an earlier publication [2].

The transmission function inferred from Figure 2.1 shows that the ratio is approximately 1 at high kinetic energy. Below about 700 eV, the ratio declines rapidly until about 400 eV, where it is less than 0.5. This means that there can be a significant underestimation of the electron intensity, which must be accounted for. Note that the red curve with (PE=20 eV) diverges at the high kinetic energy side because the pass energy of 20 eV yields fewer counts than the pass energy 50 eV and the photon flux at the corresponding photon energy for the 4d ($h\nu$=1285 eV) is low. Apart from that, the pass energy doesn't seem to play a role and there is only a small contribution from the asymmetry parameter (difference between blue and yellow curves).

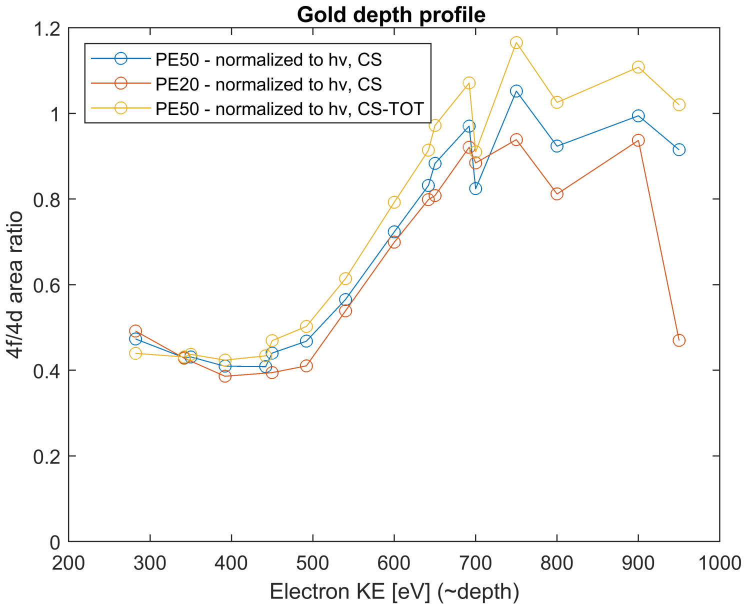

FIGURE 2.1: Evolution of the 4f/4d ratio of a gold sample as a function of kinetic energy.

In this section, we will evaluate the significance of these results in more detail and shine light on what truly happened in this gold depth profile.

In electron spectroscopy, the X-ray beam irradiates the sample which emits photoelectron via the photoelectric effect. The electron analyzer then measures the kinetic energy of electrons and the obtained spectra consist of peaks corresponding to the different species on the surface of the sample. After background subtraction, the area under a peak intensity, A, arises from different factors and can be written as:

$$A \propto \phi_{ph} \cdot n_d \cdot IMFP \cdot \sigma_T \cdot T_A \tag{2.2}$$

where ϕ_{ph} is the photon flux, n_d is the atomic number density, $IMFP$ is the inelastic mean free path of the photoelectron, σ_T is the total cross-section of 1 atom, and T_A is the transmission function of the electron analyzer. In addition, we note that scattering of primary electrons can significantly decrease the area intensity, for example through a gas phase or in an adventitious carbon covering layer. However, these can't play a role in the gold depth profile case (Figure 2.1) because the 4f and 4d orbitals are in exactly the same environmental conditions, therefore any effect will cancel out in the ratio.

While the photon flux and the total cross-section have been accounted for, the IMFP cancels out in the ratio since both measurements are performed at the same KE, and since the atomic number density is independent of the kinetic energy, it seems that only the transmission function can explain the unexpected gold depth profile seen in Figure 2.1. But how exactly did we account for the photon flux? How is the photon flux measured?

2.1.2 *Photon flux*

In order to calculate accurate depth profiles, normalization of the peak intensities to the photon flux must be performed. This is highly dependent on the accurate measurement of the photon flux itself. At the ISS beamline [3], the photon flux is measured with the *AXUV100G* photodiode from the *OPTO DIODE* company [4]. One diode is mounted along the beamline, i.e. before the experimental chamber, and another one is mounted on a sample holder. Therefore, the photon flux can be measured at the sample position, after the beam has passed through the silicon nitride (SiN_x) window that isolates the experimental chamber from the upstream high vacuum beamline. This diode converts X-ray photon flux into a measurable electrical current (typically, in the range 1-10 μA) following the relation:

$$\phi_{ph} = \frac{I_0 \cdot QE_{diode}}{E_{ph} \cdot e} \tag{2.3}$$

where E_{ph} is the photon energy in electronvolt, I_0 is the photo-current measured in amperes, $QE_{diode} = 3.6$ is the quantum efficiency of the diode in watts per amperes and $e = 1.602 \cdot 10^{-19} C$ is the elementary charge. In Figure 2.2, two photo-current measurements are shown: in red the photo-current measured in the beamline, and in blue, the photo-current measured in the chamber. The photo-current data has been transformed to photon flux units using Equation 2.3

The global shape resembles the transfer function of a band-pass filter: we first have a rising edge from 400 to 700 eV then a 's-shaped' plateau from 700 to 1100 eV and finally a cut-off energy at 1100 eV. Note that around 400 eV, the blue line has a small sharp drop in flux that is not present in the red line. This is due to the N K-edge absorption of the SiN_x window.

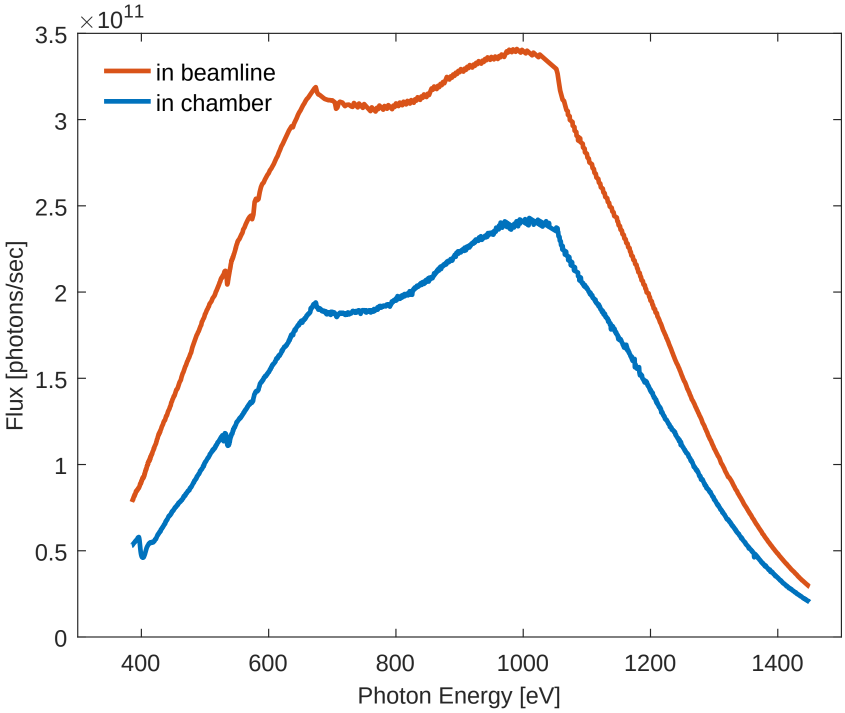

FIGURE 2.2: Photon flux measurements at the ISS beamline. The red and blue line corresponds to the photo-current measured in the beamline and in the chamber, respectively.

By taking the ratio of these two-photon flux measurements, we get the transmittance of the X-ray beam from the beamline to the chamber. This transmittance is shown as a purple line on Figure 2.3 plotted together with the transmittance calculated for a 100 nm thick Si_3N_4 layer [5], corresponding to the SiN_x window and shown in yellow. In many cases, the SiN_x window can have carbon and oxygen deposited on it from use over time. In that case, the calculated transmittance is shown as the green line and again calculated from [5].

When looking at the shape of the measured transmittance, we see that the N K-edge matches well with the expected transmittance (yellow curve) both in amplitude and absolute value. However, the global shape of the measured transmission between 500-1500 eV is quite flat when compared with the calculated transmission, and we don't see the steep slope before and after the N K-edge. As the photon energy increases, the transmittance value is lower than expected. One contributing factor to this is beam divergence, however, this should impact all photon energies equally and not affect the slope of the SiN_x window transmittance. Correcting for such beam divergence would increase the transmittance curve by an offset of $\simeq 0.25$. however, the transmittance value at low photon energy (400 to 800 eV) would then be higher than expected. When organic deposition on the window is considered, the oxygen edge at about 535 eV for the calculated transmission is much larger than the measurement. This means that the window is relatively clean in terms of oxygen contamination.

The results suggest that contamination and beam divergence are not key factors in affecting the measured transmission seen in Figure 2.3 and thus photon flux that impinges on the sample. This means that something that depends on the photon energy must have contributed to flattening the slope, by increasing the transmittance

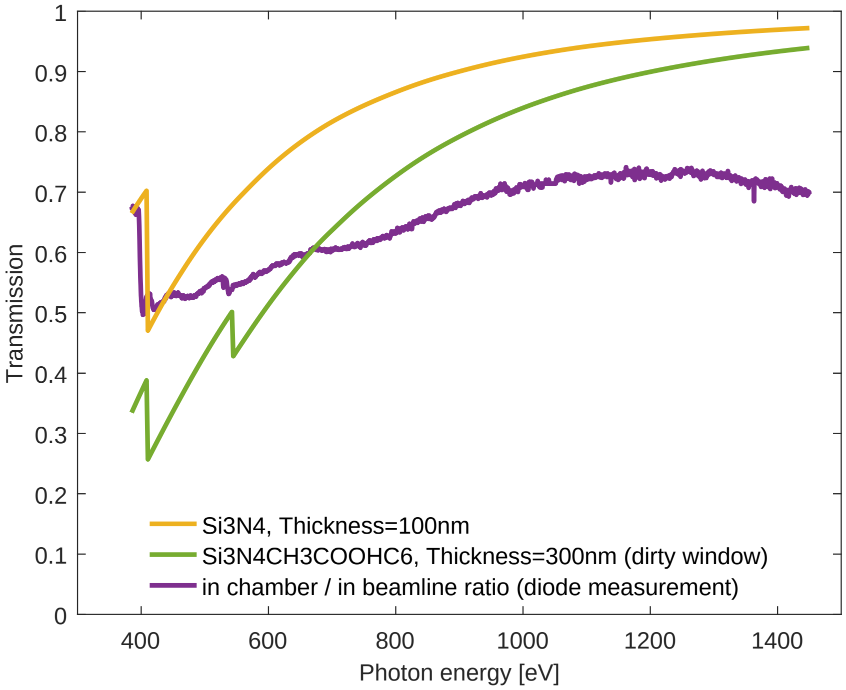

FIGURE 2.3: Transmittance of the SiN_x window as a function of the photon energy. The ratio of the photodiode measurement before/after the window is shown in purple. The expected transmittance of a 100 nm thick SiN_x window is shown in yellow. In green, the expected transmittance for a dirty SiN_x window, which would be covered with organics for a total thickness of 300 nm.

of the SiN_x window where the nitrogen should absorb and yield a steeper slope as seen in the calculated transmittance. The most meaningful hypothesis to explain such a behavior is higher-order light, discussed in the section below.

2.1.3 *Higher-order light*

The term "higher-order light" designates photons whose energies are an integer multiple of the fundamental energy, set by the monochromator. The diffracted light at the desired energy is known as the 1^{st} order light. Typically, 2^{nd} order and 3^{rd} order light have a weak intensity and can be neglected, however, this is energy-dependent and is not always the case. The In-Situ Spectroscopy (ISS) beamline uses a 600/mm spherical grating monochromator to select the photon energy needed for experiments. These gratings also transmit a fraction of the undesired higher-order light. A High Order Suppressor (HOS) can be used to remove higher order light, but due to geometrical reasons, it is not feasible to mount such a HOS at the ISS beamline. The fraction of higher-order light can be significant, especially when low-energy X-rays are used. For example at PolLux, at the beamline adjacent to ISS and using the same bending magnet, the fraction of higher-order light reaches 50% at 400 eV, as shown on Figure 2.4. In this figure, we see in blue the 1^{st} order light, that is intended for experiments, and in red and green the 2^{nd} and 3^{rd} orders, respectively. The fraction of higher orders with respect to the total flux is shown n black (value to be read on the right axis).

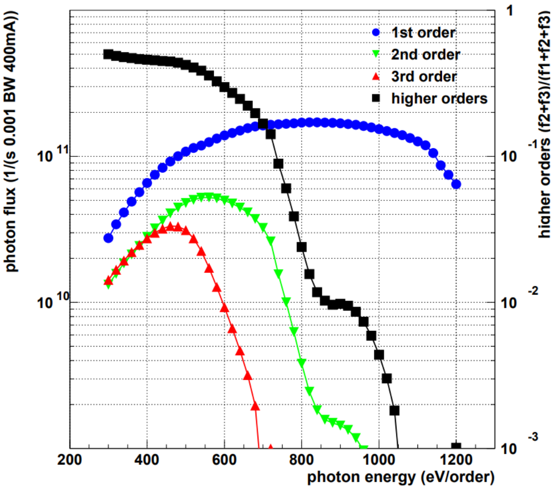

Figure 2.4: Predicted photon flux for 1st , 2nd and 3rd diffraction orders and higher-order content of the pollux beamline. Figure taken from [6]

To take into account the higher orders, Equation 2.3 can be rewritten as:

$$I_0 = (\phi^1_{ph} \cdot E_{ph} + \phi^2_{ph} \cdot 2E_{ph} + \phi^3_{ph} \cdot 3E_{ph}) \cdot \frac{e}{QE_{diode}} \tag{2.4}$$

where $\phi^n_{ph} \cdot nE_{ph}$ is the product of the photon flux and the photon energy i.e. the power of the n^{th} order. From Equation 2.4, we understand that 2nd and 3rd order light gives 2 and 3 times more current per photon than the 1st order, respectively. Hence, even a small fraction of higher order light may cause a significant error in the photon flux measurement, which is a key calibration step for some experiments in surface characterization for environmental science and catalysis. Since PolLux and ISS are twin beamlines, meaning that they both use the same bending magnet in the electron ring, it is likely that the fraction of higher-order light at ISS is similarly proportional to the first-order light. Since the photon flux is typically assessed by a photodiode that measures the total beam intensity, the measurement is systematically overestimating the 1st order flux, and more importantly, this overestimation varies with photon energy. It is suggested here that the higher-order light has flattened the transmittance slope in Figure 2.3, and as we will see later, it is responsible for the discrepancy in the Au 4f/Au 4d ratio from a value of 1.0 (Figure 2.1). Accurate photon flux calculations should properly assess the higher-order light in the X-ray beam to more reliably derive the 1st order flux from the measured photodiode current.

2.1.4 *Methods*

To disentangle the contribution of higher order light from the 1st order light in the diode measurement, we use X-ray photoelectron spectroscopy (XPS) to assess the photon flux. The photoemission spectrum is composed of peaks located at a kinetic energy $KE = h\nu - BE$, where BE is the binding energy of the orbital of interest. For each orbital, there will be as many peaks as there are orders of light in the beam, and the area of the peaks is proportional to the photon flux of the respective order. I used a gold sample and measured the Au 4f orbital in 3 kinetic energy regions, centered at:

$$\begin{cases} KE_1 = E_{ph} - BE \\ KE_2 = 2E_{ph} - BE \\ KE_3 = 3E_{ph} - BE \end{cases} \tag{2.5}$$

where BE = 84 eV is the binding energy of the main peak of Au 4f. An example of the measurement at $E_{ph} = 500\,eV$ is shown on Figure 2.5. Note the different x-axis range, y-axis intensity range, and lower signal-to-noise ratio in Figure 2.5c.

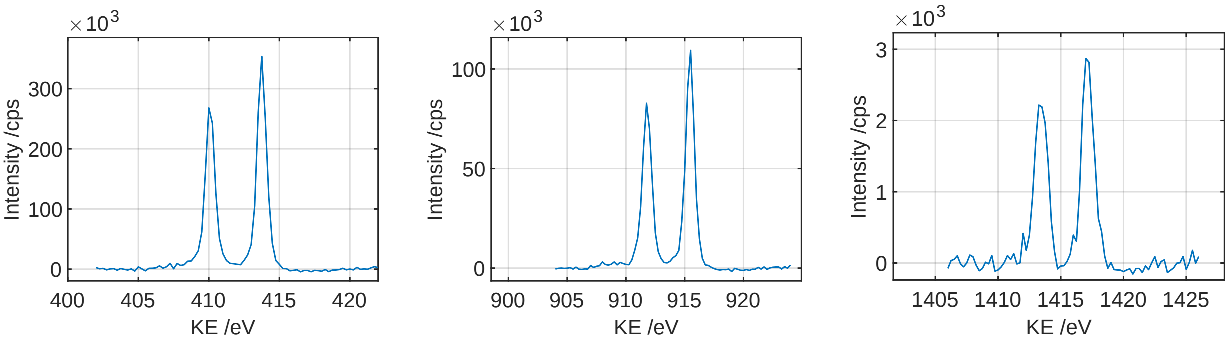

(a) first order
(b) second order
(c) third order

FIGURE 2.5: Au 4f photon-emission showing the three photon energies contained in the beam when the monochromator is set at 500 eV. Background subtracted.

To avoid as much as possible any surface contamination, that could interact with the beam and impair the precision of the higher order composition in the photon flux, I started by plasma-cleaning the gold foil 5 times. Then I inserted the gold sample into the chamber using a sample holder that can be heated with an infrared laser. I dosed 0.6 mbar of hydrogen, and heated the sample to 300 °C and then to 450 °C for about three minutes. After I stopped dosing the hydrogen, I started to dose 0.22 mbar of oxygen and kept this pressure throughout the experiment. I set the laser power to 50% and the temperature sensor was indicating a sample temperature of $\sim$ 320 °C. The combined effect of temperature and oxygen significantly reduced the carbon deposition as a consequence of beam-induced gas phase reactions.

After this cleaning procedure, I acquired Au 4f first, second, and third order photoemission varying the photon energy between 375 and 1000 eV, in order to map the contribution of higher-order light to the total photo-current measured with the diode. A linear background is subtracted from the photoemission spectra and the peak area is extracted. The photoemission areas are normalized to the total cross-section at the corresponding photon energy and to the IMFP of electrons at the corresponding KE.

2.1.5 *Results and discussion*

The normalized areas are shown on Figure 2.6. Note the logarithmic scale. The y-axis is labeled as photon flux with arbitrary units, since the normalized areas are proportional to the photon flux through Equation 2.2. We see that the 2nd order light contribution is relevant below 750 eV, while the 3rd order only contributes below 500 eV. This figure is similar to Figure 2.4, only that here the higher orders are a bit more pronounced. The 100 nm SiN_x window strongly absorbs in the region from 400 to 700 eV (see Figure 2.3) and we can see the nitrogen edge at 400 eV on the 1st order photon flux. The transmittance of the SiN_x then increases from 400 to 1000 eV and is almost fully transparent above 1000 eV. Consequently, 1st order light in the region from 400 to 700 eV is more absorbed than the 2nd order (whose photon energy is from 800 to 1400 eV) and the window acts as an amplifier on the HO light fraction at such low excitation energies.

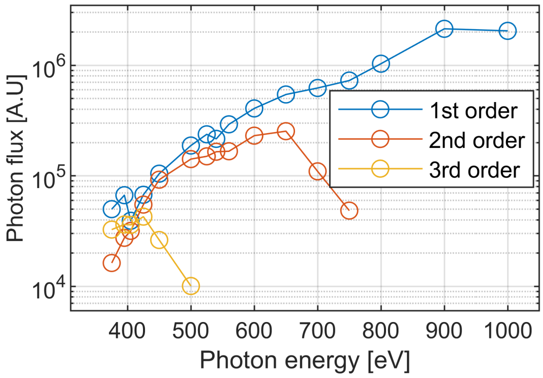

FIGURE 2.6: Photon flux of the 1st , 2nd and 3rd order retrieved from Au 4f photoemission peaks. Note the logarithmic scale

Figure 2.7 shows the relative contribution of higher order light to the total photon flux. There is a steep increase in the 2nd and 3rd order fraction as the 1st order is being absorbed at the nitrogen edge. A similar effect is visible at the oxygen edge (535 eV), probably due to some oxygen contamination.

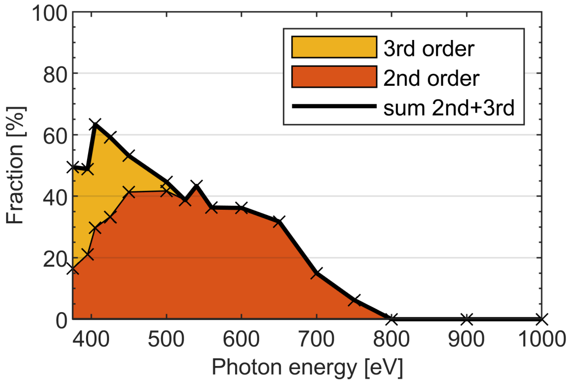

FIGURE 2.7: Fraction of 2nd order light and 3rd order with respect to the total flux. The 1st order corresponds to the white area in the graph.

Now that we know the relative amount of higher order light in the beam, we can calculate the 1st order only photon flux based on the photodiode measurement. We must still measure the photo-current with the photodiode because the photon flux changes slightly from beamtime to beamtime. But now that we know the relative amount of higher order light in the beam, and assuming that the proportions are constant with time we can calculate the overestimation that the photodiode produced, using Equation 2.4:

$$overestimation = \frac{\phi^1_{ph} + 2 \cdot \phi^2_{ph} + 3 \cdot \phi^3_{ph}}{\phi^1_{ph}} \tag{2.6}$$

At low photon energy in the range from 400 to 700 eV, the 2$^{\text{nd}}$ and 3$^{\text{rd}}$ order are quite intense and this overestimation can be substantially larger than 1, leading to an erroneous depth profile. As previously described, depth profiles are measured as a ratio, $\frac{A}{B}$, where the photoemission intensities of elements A and B are normalized by their respective photon flux. Since these two species have different binding energies, we need to use different photon energies to measure them at the same kinetic energy (we want to measure the ratio at the same probing depth). To correct this ratio, we need to multiply it by the ratio of the respective overestimation. The correction factor (CF) is:

$$CF = \frac{\phi^1_{ph}(h\nu_a) + 2 \cdot \phi^2_{ph}(h\nu_a) + 3 \cdot \phi^3_{ph}(h\nu_a) \quad \cdot \quad \phi^1_{ph}(h\nu_b)}{\phi^1_{ph}(h\nu_a) \quad \cdot \quad \phi^1_{ph}(h\nu_b) + 2 \cdot \phi^2_{ph}(h\nu_b) + 3 \cdot \phi^3_{ph}(h\nu_b)} \tag{2.7}$$

where $(h\nu_a)$ and $(h\nu_b)$ are the photon energies used for element A and B, respectively. Equation 2.7 is represented on Figure 2.8 for different binding energy differences (DeltaBE).

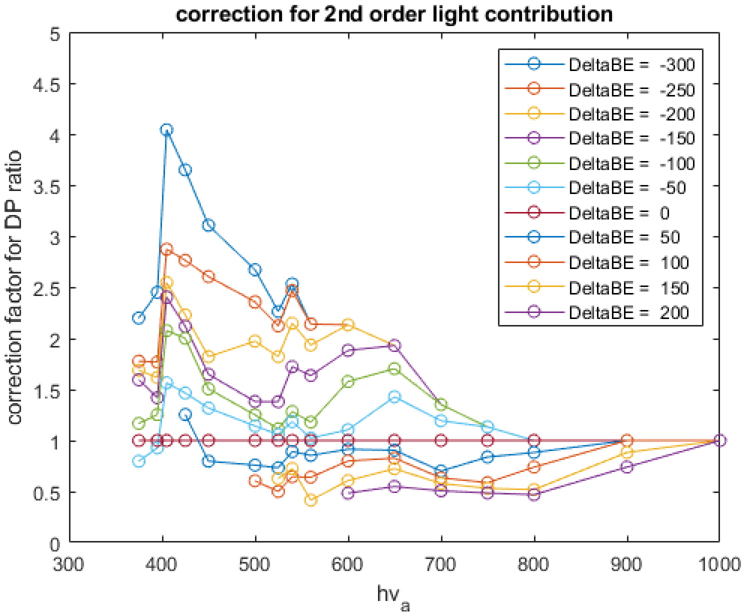

FIGURE 2.8: Correction factor to be applied to a depth profile ratio to correct for higher order light errors.

The correction is applied to the gold depth profile from Figure 2.1. The binding energy difference between Au 4f and Au 4d is Δ_{BE} = -250 eV and we have $h\nu_a = KE + 84$ eV. Therefore, we need to multiply the 4f/4d ratio by the yellow line in

Figure 2.8 labeled Δ_{BE}=-250. Figure 2.9 shows the gold depth profile before and after the correction is applied. We see that the low ratio in the KE range from 300 to 600 eV is nicely compensated by the 2-2.5 that the correction factor suggests at the corresponding photon energy range (384 to 684 eV).

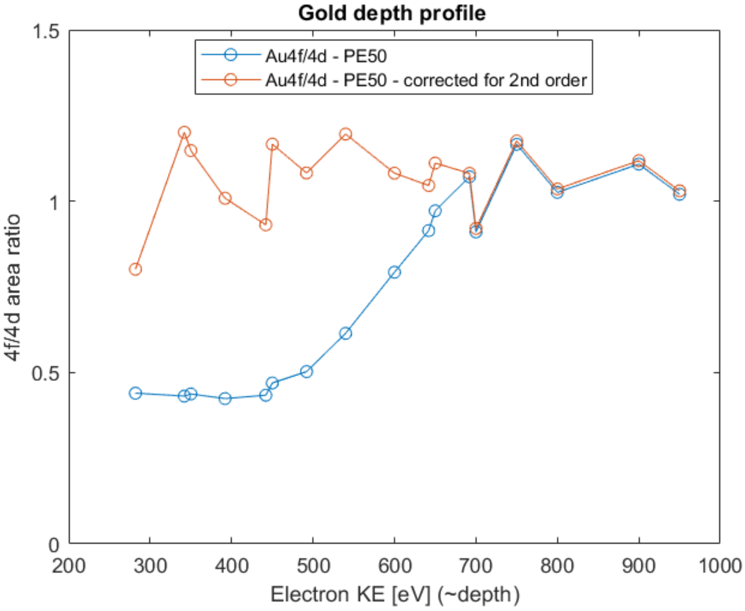

FIGURE 2.9: Gold depth profile corrected for the higher order light contribution.

2.1.6 *Conclusion*

The measured transmittance curve in figure Figure 2.3 is flat compared to the calculated transmittance and that is due to higher order light. Using the the relative 1st , 2nd and 3rd orders intensity measured on a gold sample, a correction factor has been derived and successfully corrected the 4f/4d gold depth profile (Figure 2.9). The transmission function of the analyzer doesn't seem to play a significant role in the detection of electrons, at least not within the kinetic energy range considered here and at the level of precision of these experiments.

References

1. `https://vuo.elettra.eu/services/elements/WebElements.html`.
2. Yeh, J. & Lindau, I. "Atomic subshell photoionization cross sections and asymmetry parameters: 1 Z 103". *Atomic data and nuclear data tables* **32**, 1–155 (1985).
3. Orlando, F., Waldner, A., Bartels-Rausch, T., Birrer, M., Kato, S., Lee, M. T., Proff, C., Huthwelker, T., Kleibert, A., van Bokhoven, J. & Ammann, M. "The Environmental Photochemistry of Oxide Surfaces and the Nature of Frozen Salt Solutions: A New in Situ XPS Approach". *Topics in Catalysis* **59**, 591–604 (2016).
4. `https://optodiode.com/photodiodes-axuv-detectors.html`.
5. `https://henke.lbl.gov/optical_constants/filter2.html`. Lawrence Berkeley National Laboratory's Center for X-Ray Optics.
6. Flechsig, U., Nolting, F., Fraile Rodriguez, A., Krempask, J., Quitmann, C., Schmidt, T., Spielmann, S. & Zimoch, D. *Performance measurements at the SLS SIM beamline* in *AIP Conference Proceedings* **1234** (2010), 319–322.

3

THE PREMELTING OF ICE REVISITED WITH X-RAY ABSORPTION SPECTROSCOPY

This chapter is adopted from the manuscript in preparation, which will be published as: Gabathuler, J. P., Yang, H., Manoharan, Y., Boucly, A., Alpert, P. A., Artiglia, L., Bartels-Rausch, T. & Ammann, M. "The premelting of ice revisited with X-ray absorption spectroscopy" (in preparation)

3.1 The premelting of ice revisited with X-ray absorption spectroscopy

Ice is ubiquitous in the environment and plays an important role in atmospheric chemistry. On a molecular level, the ice surface has been investigated intensively notably due to the premelting effect close to the melting point. Using partial electron yield X-ray absorption spectroscopy (PEY-XAS), we have investigated the structure of the hydrogen-bonding (HB) network in the first few molecular layers of the ice surface. In the context of our experimental methods and results, we provide a detailed data analysis to better elucidate the absolute thickness of the quasi-liquid layer (QLL) on ice and its corresponding uncertainties. We have also developed a new Monte Carlo simulation of electron scattering in matter to determine the probing depth in PEY-XAS and reduce the associated uncertainty. The main result of this analysis of the scattering effects is that the probing depth in PEY-XAS increases as the measuring KE window is set further away from the primary Auger emission energy, and decreases when the gas phase pressure above the sample rises. Overall, the more reliable analysis shows a QLL thickness of 0.5 nm at -10°C and of 2 nm at -1°C.

3.1.1 *Introduction*

Ice covers on average 10% of the Earth's surface throughout the year as ice caps, sea ice, glaciers, permafrost, and snow cover [1], and a seasonal maximum of 40% of the land being covered by ice or snow [2]. In the atmosphere, the glaciation of clouds is important for precipitation, and cirrus clouds covering substantial areas of the troposphere trap long-wave radiation. Thus, ice is important in the climate system of the Earth [3–5]. Cirrus clouds host ice particles in significant numbers to influence atmospheric chemical composition through gas phase adsorption or aerosol scavenging [6–8]. For example, global transport models show that the presence of ice in the upper troposphere decreases the lifetime of HNO_3 from 2 weeks to 1-5 days, which subsequently decreases the ozone concentrations by 20-30% [9]. In the environment, ice is a surface for multiphase chemistry [2]. For example, gas-to-particle reactions that occur on ice in polar stratospheric clouds are responsible for the activation of chlorine species and catalytic destruction of ozone in the polar winter [10–13].

Historically, phenomenological evidence has led to the idea of an interfacial disorder, as an explanation for the regelation experiment [14, 15]. This interfacial phenomenon is often called premelting or "quasi-liquid layer" (QLL) as the assumption is to describe it as a homogenous layer, whose thickness D(T) expands towards bulk melting as the temperature T approaches the triple point temperature T^0 from below. The onset temperature T_{onset}, as well as the precise functional form of D(T), is still under debate. If the presence of an interfacial liquid layer between the solid and the gas phase reduces the surface energy, then the ice will spontaneously melt, even in a region of the phase diagram that does not allow the liquid to exist, until the energy spent on melting equals the energy gained from reducing the surface energy [16, 17]. Indeed, the presence of an interfacial layer whose thickness increases with temperature has been verified with many experiments [18–33].

Although the QLL is thought to be very thin, it has a large range of impacts, such as the capability to facilitate the formation of snowballs, the slipperiness of ice, halogen activation sustaining ozone depletion and even cloud electrification [16, 34, 35]. Atmospheric ice has been studied for a long time, and the mechanism of adsorption and the chemistry of trace species on the ice surface have been intensively investigated [6, 8, 36–39]. There is evidence that disordered water molecules on the ice surface can influence the adsorption of atmospheric trace gases [32, 40–45].

Despite progress in characterizing the QLL [6, 16, 34, 46], there remains significant uncertainty on the onset temperature and thickness of the QLL [32, 42, 47, 48], which confounds predicting its behavior under various temperatures. The QLL increases in thickness with increasing temperature but it has also been suggested to increase with the coverage of adsorbates. A wealth of publications have studied the QLL using a variety of techniques including proton backscattering, nuclear magnetic resonance, and many others detailed in Sazaki et al. [49]. However, there is as much as two orders of magnitude difference in the reported QLL thickness from employing various experimental techniques [6]. Discrepancies are related to the uncertainty in the probing depth of the methods and artefacts may occur through interactions of the probe with ice [20, 23, 31, 44, 50–52].

One of these techniques is X-ray absorption spectroscopy (XAS), which allows probing the energy levels of the lowest unoccupied molecular orbitals (LUMOs) by exiting core electrons with x-rays into these orbitals. The core vacancy resulting from the absorption must be filled with an electron from the valence band. The energy difference is released either by a photon (fluorescence) or transferred to another electron called an Auger electron which is then ejected from the atom/molecule. In the case of gas phase water, the O K-edge XAS spectrum has 2 sharp features at 534 and 536 eV corresponding to the transition from O 1s (K shell) to the 4 a1 and 2 b2 orbitals followed by even sharper Rydberg orbital features which are mostly composed of 3p and 4p orbitals (Figure 10 in [53]). In ice and liquid water, the short intermolecular distances and H-bonds distort the molecular orbitals, (figure 13 in [53] and text below). Instead of the sharp features of the gas phase XAS, we see a *pre-edge* at 535 eV, and a broad *main* and *post-edge* in the region 536-545 eV (figure 29 in [53]). Figure 1C in [54] or Figure 18 in [55] shows the XAS spectrum of water in the solid, liquid, and gas phase states, for comparison.

Since LUMOs are involved in forming hydrogen bonds, we observe changes in energy and intensity of the resonant transitions in the XAS spectrum of water as the hydrogen-bonding (HB) network modifies. Liquid water has been described to have a more pronounced pre-edge and main to post-edge ratio compared to ice [53, 56]. Although the pre-edge is associated with unsaturated OH (not involved in an H-bond, also termed dangling OH) [57, 58] present in bulk liquid and on the surface of the ice, John Tse precises that the pre-edge can vary in width and amplitude depending on the distribution of the electronic transitions, and that the crystalline ice typically leads to weaker but broader pre-edge [59]. Hence, the pre-edge feature is not a concise indicator of the magnitude of the local disorder within the hydrogen-bonded network [59]. The main edge is associated with weak asymmetric configurations (liquid-like) while the post-edge relates to the strong symmetric, tetrahedral structure (ice-like) of hexagonal ice [54]. The XAS spectra of water (independent of phase) feature an isosbestic point at around 539 eV [60], meaning [61] that the density of states (DOS) distributes between the main-edge and the post-edge depending on the H-bond network configuration.

In partial electron yield x-ray absorption spectroscopy (PEY-XAS), we obtain the XAS spectra by measuring the intensity of Auger electron emission as a function of photon energy. Because electrons have an inelastic mean free path (IMFP) of about 2 nm, PEY-XAS probes the top few molecular layers of ice, giving information on the coordination in the hydrogen-bonding network within the surface region of ice [53]. In 2002, Bluhm et al. studied for the first time the premelting of ice as a function of temperature, using PEY-XAS. They measured an onset temperature of around 253K (-20°C) and a thickness of about 2 nm near the melting point [56]. This same technique has been routinely used in recent work [42, 45, 47, 62–64] to measure how adsorbed species can perturb the structure of the surface of the ice.

Until now, the escape depth of electrons in PEY-XAS has been assumed to be ED=$\cos(\alpha)\cdot$IMFP, where α is the angle between the normal of the surface of the sample and the electron detection axis, and IMFP refers to the inelastic mean free path of electrons at the kinetic energy at which they were collected for the acquisition of the XAS spectra. The IMFP is a strong function of kinetic energy and increases from about 1 nm at 100 eV to around 4 nm at 1000 eV. In addition, IMFP values have a relatively high uncertainty of about 30% [65]. In PEY-XAS, the electrons are measured within an acceptance kinetic energy range that we refer to as the kinetic energy window (KE window), which is often at significantly lower KE than the primary Auger electrons. The primary O KLL Auger electrons used for the acquisition of O K-edge XAS have KE of 450-500 eV, and typical KE windows are around 400 eV (412 to 437 eV in [56]). Therefore, some of the measured Auger electrons may have scattered, losing part of their kinetic energy (on average, 60 eV per scattering event) and therefore stem from substantially deeper (factor up to 2-3) within the ice surface [66, 67]. Therefore, ignoring electron scattering results in a considerable underestimation of the probing depth. In the previous studies based on PEY-XAS of ice surfaces, the probe depth was not well defined, which calls for a better assessment to improve the estimates of QLL thickness. In addition, because electron scattering also occurs in the gas phase, there is a need to assess the role of the gas phase pressure in terms of the probing depth [47, 65, 68]. Gas phase water molecules between the ice surface and the detector can also scatter electrons, decreasing their energy through inelastic collisions prior to being detected. Therefore, while the effect of scattering in the condensed phase leads to an increased probe depth, in the case of scattering in the gas phase, a measured reduced electron energy may not always translate to their origin being at a greater depth below the ice, as will be shown in this work.

We present new data on the temperature dependence of the hydrogen-bonding network at the air-ice interface using PEY-XAS. We use this data to derive the QLL thickness as a function of the temperature following a procedure that allows carefully estimating uncertainties. This procedure includes a careful estimation of the photon flux at the sample spot considering second-order light artefacts and gas phase absorption, the analysis using pre-edge and main-to-post-edge ratio to derive the disorder, and the implementation of a newly developed Monte Carlo simulation that mimics the mechanics of electron transport in our experiment. From the simulation, we derive the probing depth of the electrons of interest taking the kinetic energy window and gas phase pressure into consideration. We have found that electron scattering is a major uncertainty in PEY-XAS, enough to substantially change the interpretation and conclusions of XAS spectra.

3.1.2 *Methods*

3.1.2.1 *Experimental setup*

Experiments were conducted at the in situ spectroscopy (ISS) beamline at the Swiss Light Source (SLS) at the Paul Scherrer Institute. A detailed description of the experimental setup is available in Orlando et al. [64]. The X-rays enter the experimental chamber via a 100nm thick silicon nitride window (Si_3N_4). The emitted electrons reach the electron analyzer through the aperture of a cone. A differentially pumped electrostatic lens system ensures UHV condition on the analyzer side, while the experimental chamber can be pressurized up to $\sim$10 mbar. The aperture had a diameter of 0.5 mm and a working distance (focal distance, distance between focus of the electron optics and the aperture) of 1 mm.

In the experimental chamber, ice was grown from vapor deposition onto a sample holder. The sample holder was a gold-coated copper plate cooled with a flow of cooled gas on the reverse side of the plate. The temperature was measured with a PT-1000 thermometer attached on the side of the holder. A gas inlet allowed water vapor to enter the chamber from two temperature-controlled reservoirs containing highly purified water (impurities < 5ppb, Sigma-Aldrich, Product Number: 14211-1L-F). The water was subjected to 3 freeze-pump-thaw-cycles to remove any dissolved gases. The two reservoirs were connected to the sample chamber via either a 2.0 mm or 0.8 mm diameter capillary. The desired water vapor pressure in the chamber was achieved by using either one of the capillaries and adjusting the reservoir temperature. Then, the temperature of the sample holder could be set in order to achieve supersaturated conditions with respect to ice and drive ice crystal growth. After a suitable amount of ice formed as seen from an endoscope camera mounted on the window port of the chamber, the sample holder temperature was adjusted to the equilibrium conditions given by the vapor pressure of ice [69] resulting in a stable ice surface without net evaporation or growth. To document ice stability between each XAS measurement, we used x-ray photoelectron spectroscopy (XPS) to monitor the O 1s signal from the gas phase and the ice. In Parallel, we routinely acquired C 1s spectra to make sure that the adventitious carbon is lower than a tenth of the oxygen signal. XPS of O 1s and C 1s were measured with a photon energy of 1000 eV, giving electron kinetic energy of 465 eV and 270 eV, with an associated probing depth of 2 nm and 1.3 nm, respectively. The pass energy for these measurements was set to 20 eV to allow resolving the gas phase and condensed phase contribution to the O 1s spectrum, and the different components of C1s. Slits were fully open (1/1) to maximize the counts. We used a residual gas analyzer (RGA) connected to the second differential pumping stage downstream of the electron sampling aperture to monitor the gas phase and notice leaks or other eventual contaminations.

3.1.2.2 *PEY-XAS of ice*

Auger yield x-ray absorption spectra were measured using X-rays at photon energies from 515 eV to 560 eV with 0.25 eV steps at the absorption edge from 529 to 542 eV and 0.5 eV steps elsewhere. At each photon energy, the electron analyzer measures the kinetic energy of electrons in the kinetic energy range from 425 eV to 525 eV. Figure 3.1 displays the typical data obtained from an ice sample. The image at the bottom shows the electron counts (color-coded) for a specific kinetic energy (y-axis) as a function of photon energy. We can see two oblique lines with two different slopes corresponding to traveling photoelectron peaks. The line crossing the image from hv=515 eV and KE=485 eV until hv=555 eV and KE=525 eV, thus with a slope of -1, corresponds to photoemission from the O 2s valence level. Also, more faintly, but still with the same slope, the other valence level peaks (ending with O 1b1) are visible. The most intense line with a slope of -2 is due to photoemission from the O 1s core level excited by the second order light (thus photons with double energy compared to that adjusted at the monochromator and plotted on the x-axis). The Auger electron peaks appear as horizontal lines because they have a constant kinetic energy independent of the photon energy responsible for the initial core-level excitation. The most visible Auger emission line on the image in Figure 3.1 is at 500 eV, corresponding to the sharp gas phase feature that we see in Figure 1(a) of [70]. On that figure (Figure 1(a) of [70]) we can also see the Auger spectrum of liquid water which is similar to that of gas-phase water, but with broader features. Broadening could come from increased scattering in the condensed phase due to higher density, different HB configurations that lead to broadening in the valence level energies, and interatomic Coulomb decay (involvement of neighboring atoms in the Auger process) [70]. In addition, we notice that the Auger spectrum of liquid water seems to change with temperature (still on Figure 1(a) of [70]) and I have observed a similar trend in my data see Figure 3.14(a) however, this might simply be an artefact from gas phase scattering, as we will discuss later in Section 3.1.3.2. Among the few studies that have published Auger spectra for ice, we can cite [71] where figure 2 shows experimental ice Auger spectra compared to the experimental gas-phase spectra. The main difference between gas phase and condensed phase Auger spectra is the broadening of the Auger features. Similar to liquid water, the Auger spectrum of ice consists of multiple broad transitions spread between 450 eV and 500 eV [71–74].

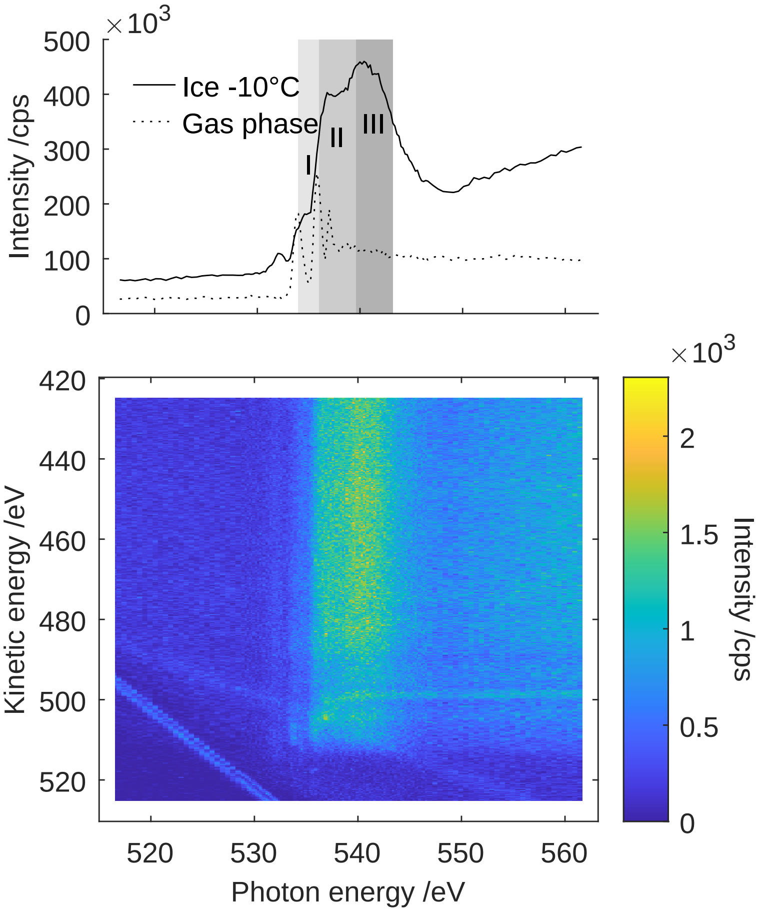

FIGURE 3.1: (bottom) PEY-XAS data of ice at -10°C shown as an image with the photon energy in the x-axis and the electron kinetic energy in the y-axis. The intensity of measured electrons for a specific photon energy and electron kinetic energy is color-coded, the color bar is shown on the right. Multiple features are present in this image, see the description in the text. (top) PEY-XAS spectrum integrated from the image below, shown together with a gas phase spectrum for reference. The grey-shaded rectangles labeled 'I', 'II', and 'III' corresponds to the area of the spectrum where we observe a change between the liquid and solid state of water.

From the image shown on Figure 3.1 (bottom), the PEY-XAS spectrum is obtained by integrating the intensity along the KE-axis over part or the full kinetic energy range (Figure 3.1 (top)). The PEY-XAS spectra of ice consist of a background from 515 to 530 eV, followed by a small bump which is attributed to C=O, thus oxygenated adventitious carbon. The absorption edge starts with a shoulder at 535 eV (that we call the pre-edge, labeled 'I' here) followed by the main edge (II) and the post-edge (III). As we have seen in the introduction, their ratio (main-to-post-edge ratio) represents the ratio of hydrogen bonds populations in configurations with weak asymmetric bonds (liquid-like) to those with strong symmetric hydrogen bonds (ice-like) [54, 75, 76].

3.1.2.3 *PEY-XAS analysis*

After the integration of the signal, a series of processing steps are necessary in order to analyse the PEY-XAS spectra. The first step is to average repetitions, to get more

SNR. The averaged spectrum is then normalized to the photon flux. The photon flux contains a large fraction of higher order light (see Section 2.1) and the first order flux that we need to normalize the spectra is calculated from the photocurrent, see supporting Figure 3.9. In addition, gas phase X-ray absorption in the path from the SiN_x window to the sample is taken into account (see supporting Figure 3.10). From this point, we remove the gas phase contribution from the PEY-XAS signal, which can be substantial for a warm ice sample (see supporting Figure 3.10 red spectra when the data is normalized to the first order photon flux corrected for gas phase X-ray absorption, but the gas phase Auger yield is not yet subtracted from the PEY-XAS signal). Finally, the background is subtracted and the spectrum is normalized. More details are provided in supporting Section 3.2.1.

3.1.2.4 *Monte Carlo simulation*

The MC simulation is based on the following assumptions:

- Elastic scattering is negligible (See [77] EAL∼IMFP). This is a reasonable assumption for water because oxygen has a small atomic number Z, and elastic scattering scales with Z^4.
- Straight-line approximation: Inelastic scattering does not lead to dispersion of the direction. Electrons are scattered forward, scattering only changes the kinetic energy.
- Auger electrons are only generated at three different kinetic energies.
- The electrons are emitted perpendicular to the surface, in the experiment the analyzer make a 30° angle with the surface therefor a factor cos(30°) needs to be added to the simulation results for a correct description of the experiment.

Origin To start with, we need to create an electron at a specific depth. The X-ray beam intensity decays exponentially with depth in matter; however, on the scale that we consider here i.e. a few nanometers, we can assume that the X-ray excitation is homogeneous with depth. Therefore, we assign the origin, O, of the generated electron with a uniform probability density distribution between 0 and 100 nm. In the simulation, we assume that the X-ray beam has a normal angle of incidence with respect to the beam.

Auger spectra We know from experimental measurement that the Auger spectra of Water consist of several emission peaks corresponding to different transitions in the Auger emission process. Figure 1 in [74] shows 4 well-defined peaks and the deconvolution reveals 4 others (total = 8). Carravetta [72], in his hole-mixing calculations find 14 peaks. Electronic transition rate calculations reported 16 transitions [73]. Only Liegener [71] shows experimental ice spectra and theoretical liquid. There are a few reported Auger spectra for water, mostly gas phase measurement, and they only agree on a qualitative level. Given the uncertainties and inconsistencies among data and theory, we use only the three dominating contributions, spread over the region 450-500 eV. The electrons are generated with the function Generate_auger.m (see repository) which randomly generates kinetic energy according to a distribution made of 3 Gaussians with relative height, position, and width of 1/4/10, 455 eV/475 eV/498 eV, 4 eV/3 eV/2 eV, respectively.

IMFP Now that we have created an electron at a certain depth in the ice and with a defined kinetic energy, we need to know the length of the path that it can travel before interacting inelastically with the ice (with matter). This is literally the definition of the inelastic mean free path (IMFP) and it is a central aspect in electron spectroscopy as it provides the surface sensitivity. The IMFP depends on the kinetic energy of the electron, the density of the medium, and is relatively independent of the nature of the material which is the reason why we often refer to the "universal curve": a curve with the shape of a parabola, with a minimum around 100 eV, where all IMFP measurements seem to gather. However, the exact values of the IMFP for water are controversial and the mismatch among measurements is typically ~30% (qualitatively from figure 14 in [77], maybe more quantitatively from Werner et al. [67] or Tanuma et al. [78]. Cross section data has typically 20-30% std dev. [65]). For the sake of simplicity, the simulation presented here uses the universal curve formula considering only the kinetic energy:

$$\lambda = \frac{A}{KE^2} + B\sqrt{KE} \tag{3.1}$$

where A=641 and B=0.096 for inorganic compounds [79]. This universal curve formula for inorganic compounds is in relatively good agreement with the TPP-2M formula (data retrieved frorm QUASES software) and with Shinotsuka [80] as shown in supporting Figure 3.12. In spite of the uncertainty related to the absolute values of the IMFP, this is a suitable and simple-to-implement basis for the purpose of this work.

DIIMFP After having a means to know the distance an electron travels until an inelastic scattering event occurs, we now need to assess the KE it looses in that. The differential inverse inelastic mean free path (DIIMFP) is the probability for an electron to lose a certain amount of kinetic energy T upon scattering, for a given initial kinetic energy KE. The integral of the DIIMFP over the energy loss $\langle T_{loss} \rangle$, gives the inverse IMFP λ^{-1} [67]. The DIIMFP can be estimated from the universal cross-section (UCS) or calculated from optical data. TPP-2M formula for the IMFP was used to estimate the absolute value of DIIMFP [81]. Sessa's database [82] contains both UCS and optical data for gold. This data can be used to see and estimate the uncertainty, ~50%. As for the IMFP, we see that this input also brings in substantial uncertainties. For water, there is no optical data (in Sessa's database) so we will use the UCS curve in this simulation, as a reference to how much energy is lost at each scattering event, which is sufficient for the purpose of these simulations.

Scattering Now that we have all the inputs, we can run the simulation. The electron is generated at an origin O and it travels towards the surface. The probability to *scatter*, anywhere in the path from the current electron depth d to the surface is $p_s(d) = 1 - e^{-\frac{d}{\lambda}}$. Similarly, the probability to *not scatter* in the path from the current electron depth d to the surface is: $p_{ns}(d) = e^{-\frac{d}{\lambda}}$. The simulation generates a random number uniformly distributed in the interval [0 1] using the MatLab function rand(). This random value is stored in the variable p_rand, and if p_rand>p$_{ns}(d)$, the electron at depth d undergoes a scattering event, which triggers four steps: (1) the count of scattering events for this electron increases by 1, (2) the depth of the electron is decreased by the length of the free path $FP = IMFP(KE) \cdot (-ln(p\_rand))$, (3) the KE is decreased by the energy loss which is chosen randomly in the UCS distribution of water [82], and finally (4) the IMPF is updated according to the new KE. Note that because p_rand>p_{ns}, the FP cannot be longer than d. The loop continues until the KE is smaller than the arbitrary number 100 eV or in the event of p_rand<$p_{ns}(d)$ which is the case corresponding to the electron reaching the surface. In such an event, the origin of the electron, the KE at the surface and the number of scattering events, and the KE at the surface are saved in a table – for later analysis.

3.1.3 *Results and discussion*

3.1.3.1 *XAS of ices*

Figure 3.2 shows examples of measured PEY-XAS spectra of ice at -10°C, -2°C, -1°C, and of a liquid water film at +0.5°C. All spectra consist of a background from 516.6 to almost 530 eV, a small bump at ~532 eV corresponding to oxygenated carbon contamination, then we have the pre-edge, main-edge, and post-edge (I, II, and III as described in Figure 3.1, top). The data were processed as briefly explained in Section 3.1.2.3 or in more detail in the supporting Section 3.2.1. Without background subtraction, all backgrounds would have the same slope, as seen in Figure 3.8, where the spectra have been normalized to the background region. Most importantly, when analyzing XAS spectra, it is important to normalize the spectra in a way that the tails align [54] otherwise relative feature intensities may change significantly and the isosbestic point may not exist as seen in figure S1,a) in the supporting materials of [54] and in Figure 3.8. Our data seems to have an isosbestic point at 539.6 eV. However, this value is dependent on the background treatment and is, to some extent, arbitrary. Different studies report the isosbestic point for ice at 538.8 eV [76], 539.1 eV [54], 538.4 eV or 538.8 eV [83]. The ice and liquid spectra resemble a lot to figure 1c in [54]. Both the ratio of absorption at the main edge to that at the post-edge and the magnitude of

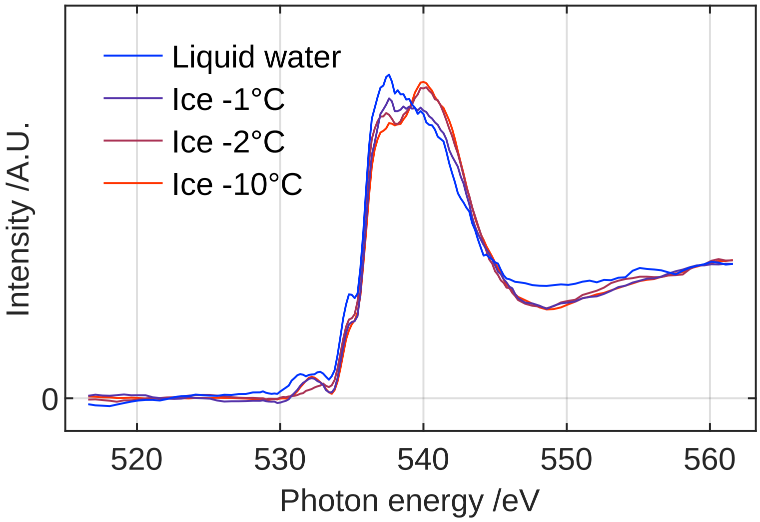

FIGURE 3.2: PEY-XAS spectra of ices at different temperatures. The data have been analyzed as described in the supporting Section 3.2.1 and Section 3.2.1. Increasing temperature is color-coded from red to blue.

the absorption feature at the pre-edge have been related to surface disorder [53]. In Figure 3.2, we clearly see a decrease in main-to-post-edge ratio, implying a hydrogen bonding structural change as a function of temperature. On the other hand, we can hardly see any substantial change in the pre-edge region. This is very similar to the Bluhm 2002 data [56], where no explicit change is directly apparent between the different spectra at different temperature. We also note that the shape in the pre-edge region around 535 eV is affected significantly by the subtraction of the gas phase contribution[1], and also the presence of oxygenated carbon contamination leading to a variable contribution at around 532 eV. Bluhm et al. [84] have observed a correlation between the presence of contaminations and the apparent intensity of the pre-edge.

Figure 3.3 shows the PEY-XAS spectra of ice at -10°C (same data as in Figure 3.1 and Figure 3.2). The data is analyzed following the procedure described in Section 3.2.1 except for the kinetic energy window used to integrate the signal which is not 425-480 but 425-470 and 470-525 as indicated in the legend. The inset on the left is an illustration of the different paths that the electrons might have taken in the two different measurements. The colors of the inset are matching with those in the legend. As already defined in Figure 3.1 I, II, and III describe the pre-edge, the main-edge, and the post-edge; respectively.

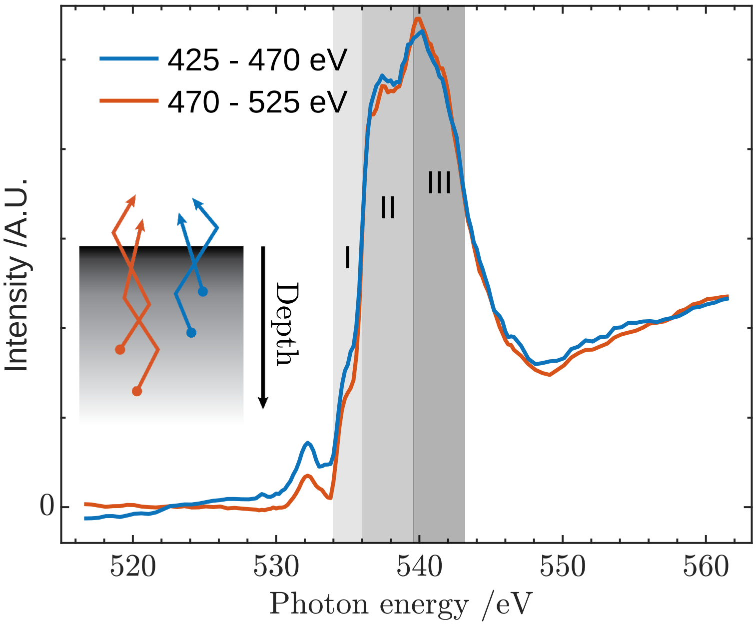

FIGURE 3.3: PEY-XAS spectra of Ice -10°C taken with different Kinetic Energy window. The inset is an illustration of the different paths that the electrons might have taken in the two different measurements. The colors are matching.

The two spectra in Figure 3.3 have globally the same shape, however, we can observe that the main-to-post-edge ratio is slightly lower on the red spectra, indicating a more tetrahedral hydrogen-bonding network. The different slopes of the low energy background gives some indication of the uncertainty of the overall processing of the spectra. Note that subtracting a sloping background, the contrast between the red and

---

[1] which does not lower the spectra completely to the linear background level as explained in Section 3.1.2.3 because of the 5 points smoothing

the blue spectrum would get even larger. We assume that the Auger emission spectrum of ice is within 450-500 eV, which corresponds to the range of energy differences between the K and L shells. In matter, an electron travels on average 1 IMFP ($\lambda \simeq$ 2.2 nm, at 500 eV in liquid water) before it undergoes an inelastic scattering event, upon which it loses part of its kinetic energy (on average $\langle T_{loss} \rangle \simeq$60 eV [82]). The electrons that scatter multiple times likely come from deeper in the sample being investigated [67]. Then the electrons reaching the analyzer with KE=[425-470][2] come from deeper compared to the electrons measured in the range 470-525, dominated by primary Auger electrons, for which 63% of the signal comes from within about one IMFP (about 2 nm) and 95% of the signal from about three IMFP. Thus, the measurement at KE= 470-525 is more surface sensitive, and the one at KE 425-470 probes a little bit more into the bulk. For the C=O peak, it makes sense that the blue spectrum shows more intensity since the KE window probes more of the surface, and carbon contamination species are assumed to be located at the surface. Again, we note that this assertion is depending on the shape of the background subtracted. We see that the main-to-post-edge ratio is more pronounced in the blue spectrum, even when considering the different backgounds. This more powerful observation suggests that the signal related to disorder is higher when measured with the more surface-sensitive KE window. Once again, this makes sense with respect to our sample model consisting of a QLL sitting on top of the ice. We note that here the gas phase has an identical role in the two cases. Thus the KE window is very important to determine the probe depth and retrieve the QLL thickness from the PEY-XAS data. In order to quantify the probe depth, we use the Monte Carlo model in the next section.

3.1.3.2 *MC results and discussion*

As just discussed above, the choice of the kinetic energy window impacts the PEY-XAS spectra, because part of the measured intensity can come from secondary electrons (that have scattered), such that the exact probing depth is a key uncertainty in PEY-XAS. The Monte Carlo method is particularly well suited to understand the physics of inelastic scattering, and to find the relationship between the kinetic energy and probing depth. The Monte Carlo simulation presented here (for assumptions and implementation details, see Section 3.1.2.4) generates $\sim 7 \times 10^6$ electrons with a kinetic energy KE_e spread between 450 to 500 eV. The simulation allows them to inelastically scatter until reaching the surface or losing all of their energy and being absorbed in the ice. The key advantage of the simulation is the ability to retrieve the origin distribution of the electrons detected by the analyzer. Primary electrons, the ones that have not scattered, have an origin distribution that follows an exponential decay with depth. Secondary electrons, on the other hand, have a small probability to come from the surface, because they must scatter at least once. Their origin distribution is non-trivial but easily retrievable from such a MC simulation. We present here key results from the simulation.

Figure 3.4 shows the simulation data visualized in three panels. The largest panel is a scatter plot, displaying 1×10^5 electrons with colored dots. The position of the dot on the y-axis indicates the depth, D_e from which the electron originates and the x-axis

---

[2] these electrons have lost some of their kinetic energy via inelastic scattering

coordinate corresponds to the kinetic energy KE_e measured by the analyzer. The color indicates the number of scattering events that the electron underwent. We notice from this panel that electrons that have not scattered (in black) are only distributed between 500 and 450 eV, where electrons are generated. Their contribution decays exponentially with the depth, from which they originate. We notice 2 triangular regions with low electron population: the upper right corner (small depth, small KE) and lower left corner (large depth, high KE). The reason for this is that it is not probable for an electron to come from the surface and experience multiple scattering or on the opposite to come from large depths without losing too much KE due to scattering.

The panel on the top shows the spectrum intensity that we get when we integrate all electrons on the depth axis. This spectrum contains the 3 Auger peaks that we used to generate electrons in the simulation, as well as a background resulting from the inelastic scattering. Experimental Auger spectra are shown in Figure 3.14a for comparison. Apart from scattering in the ice, this background also results from scattering in the gas phase, as discussed below. For better statistics, the top and right panels are histograms of 1×10^6 electrons.

The panel on the right side is the probing depth distribution of the kinetic energy window 430-450 eV, i.e. the electron depth distribution that we get when we integrate all electrons that are contained between the 2 red lines. We see that this distribution differs from the exponential distribution that we would expect for unscattered electrons (black dots), in the sense that the maximum of the distribution is not at the surface but rather at a depth of 2.5 nm. The reason for this is that this KE window mostly contains secondary electrons largely coming from deeper than one IMFP. The mean value of this distribution is 5.3 nm and we define this variable as the mean probing depth (MPD). The pink curve across the scatter plot is the mean value of D_e as function of KE_e . The value jumps from 1 to 2 IMFPs ($\sim$2.2 to $\sim$4.4 nm) as KE_e decreases from 500 to 475 eV because the electrons involved are either primary (black dots) or 1-time scattered secondary electrons (blue dots). on the second emission peak (475 eV) the value decreases again to somewhere between 1 and 2 IMFP because the electrons involved there is a blend of primary and 1-time scattered (not yet too many 2-times scattered electrons). The pink curve establishes the relationship between the MPD and the KE: the lower the KE, the higher the MPD. The dependence of MPD with KE for KE_e <450 eV can be approximated by:

$$MPD(KE) \simeq \lambda(KE) \cdot \left(1 + \frac{500 - KE}{\langle T_{loss} \rangle}\right) \tag{3.2}$$

where KE is the kinetic energy at which the electron is measured, λ(KE) is the IMFP, which is around 2.2 nm but slightly depends on KE, 500 is the KE of most electrons when they are generated, $\langle T_{loss} \rangle$ is the mean value of the kinetic energy loss per scattering event. In the simulation, T_{loss} is a distribution derived from the universal cross section theory, and $\langle T_{loss} \rangle$ $\sim$60 eV [67, 81]. From such representation, we understand that one can extract a subset of electrons corresponding to the experiment and get a distribution such as the one presented in the right panel. In PEY-XAS, one typically selects a KE window, which is the acceptance range for electrons to be detected. In the work presented here, the KE window is 425-480 eV. Bluhm et al. [84] chose the KE 412-437 eV, and we will see how different the probing depth associated with these KE

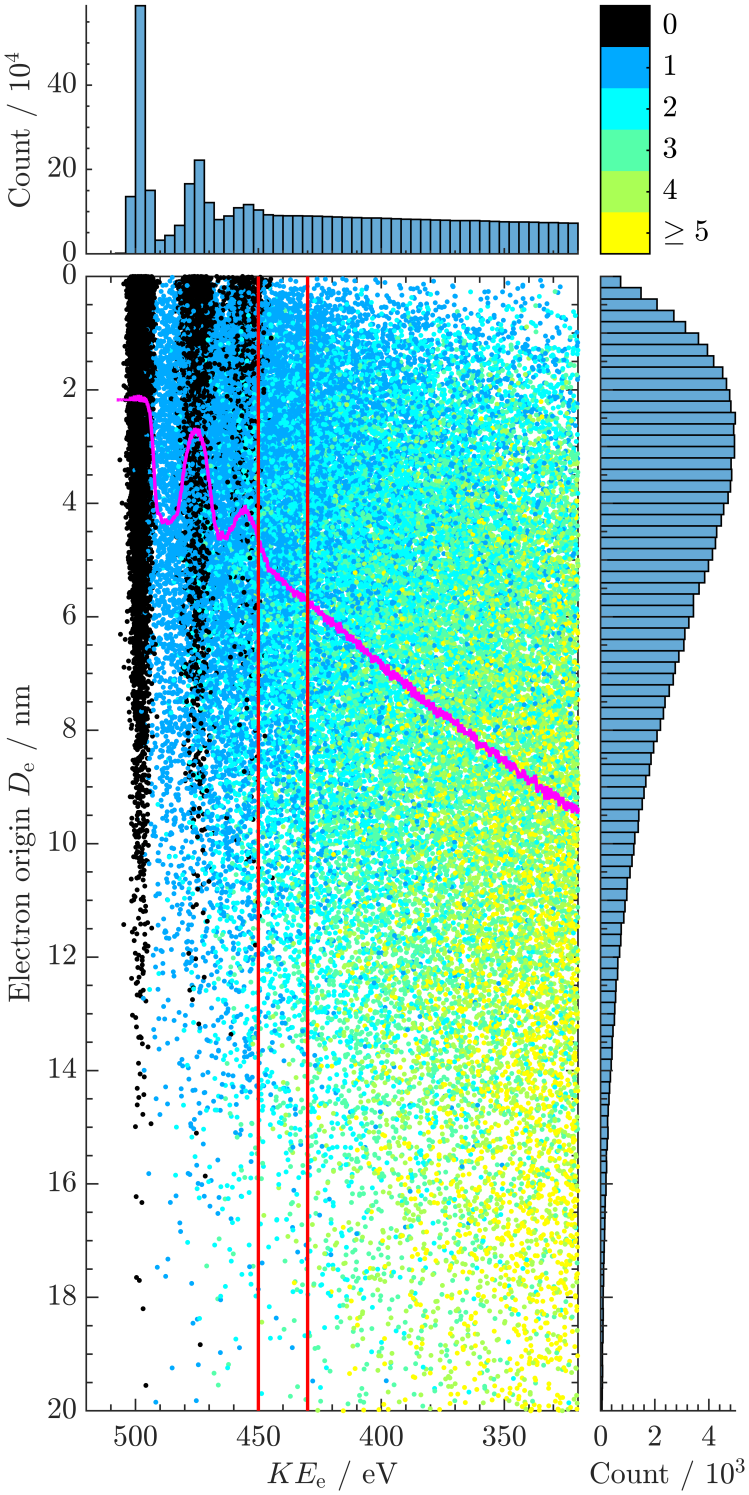

FIGURE 3.4: Simulation visualization. The main panel shows each individual electron as a dot with the color scale indicating the number of scattering events that the electron have undergone. The pink curve denotes the average depth for a fixed KE, the panel on the top is the Auger spectra integrated from the scatter plot over the whole depth and the panel on the right is the probing depth distribution for the KE window delimited by the red lines.

windows is compared to the non-scattering case.

Gas phase Impact The next relevant aspect is the gas phase and its impact on PEY-XAS depth information. Indeed, molecules at pressures in the mbar range contribute to the scattering. Since we subtract the gas phase spectrum during the analysis of the PEY-XAS spectra, we don't consider electrons generated in the gas phase in the following. The strategy of considering scattering in the gas phase is to replace it by a thin condensed phase water layer with the same number of water molecules. Suppose we want to retrieve information from a 1nm-thick surface layer with similar scattering properties and oxygen density at a KE of 350 eV. Looking at Figure 3.4, we understand that we will probe with a mean probing depth of 10nm and we won't get any signal from this layer, because there are hardly any dots in the region [0-1] nm and K=350 eV. The reason is that the Auger electrons originating in this layer did not have enough material to scatter, and thus no secondary electrons deriving from these Auger electrons can reach the analyzer with KE as low as 350 eV. Imagine now that there is 10 mbar of pressure above this layer. The same Auger electrons having escaped from the sample without scattering now have plenty of matter to scatter with, and the signal at 350 eV increases. In other words, for a kinetic energy window that contains scattered electrons[3], the pressure decreases the mean probing depth in the sample, and the measurement becomes more surface sensitive.

We have a simulation that represents electron scattering within ice, as described above (Section 3.1.3.2). We now want to add 1 mm of gas phase on top of the ice, corresponding to the distance that separates the surface of the ice and the electron-sampling aperture of the analyzer. The pressure varies from almost 0 to about 6.1 mbar when the ice temperature ranges between -40°C and 0°C. Since the total number of scattering molecules is relevant and there is only a negligible difference in cross-section per molecule between the gas and condensed phase, we may conceptually replace the gas phase by a thin layer of ice with the same number of water molecules. This layer has a thickness:

$$D = 1mm \cdot \frac{\rho_{gas}}{\rho_{ice}} \tag{3.3}$$

At -20°C, the vapor pressure over ice is 1 mbar and ρ_{gas}=8.6×10^{-4} kg m^{-3} (see details in supporting Section 3.2.4.2). With ρ_{ice}=920 kg m^{-3}, we find that D$\sim$1 nm, thus scattering over a 1 mm long path through gas at 1 mbar is equivalent to a 1 nm thick layer of ice for the purpose of the assessment of scattering. We previously considered an ice sample extending from 0 to 50 nm. Now we have a thin film of thickness D on top of it such that the ice goes to a depth of 50+D nm. Because the PEY-XAS contribution of ice at depth 50+D nm is negligible, this model is equivalent to the situation without gas phase where there would be no electrons originating from the D-mm-thick top layer, because these water molecules represent the gas phase molecules that do not contribute to the ice signal but only contribute to electron scattering. This elegant trick greatly simplifies the simulation and analysis.

In order to validate the model described in Equation 3.3, we compare the attenuation coefficient for 500 eV primary electrons. In figure 6 from [65], we can read that a 10-fold attenuation is reached when electrons travel 0.9mm in a pressure of 2.2 torr (or 3 mbar), for a KE of 450 eV. The data with KE=500 eV is not available on that figure (figure 6

---

[3] not the case at for primary Auger

from [65]), but we can estimate that the 10-fold attenuation for electrons with KE=500 eV would fall somewhere around 2.6 Torr, or 3.5 mbar. On supporting Figure 3.13, the simulation gives a 10-fold attenuation at a pressure of 5 nm_{eq}, where the calibration is 1 mbar = 1 nm_{eq}. Similarly, the simulation predicts a 10-fold attenuation with a film thickness of 5nm, see (Equation 3.3), which is the model for traveling 1 mm at 5 mbar. This means that the attenuation of 0.9 mm of 3.5 mbar vapor gas phase in [65] is equivalent to 5 nm_{eq} in the simulation. Therefore the pressure calibration should rather be:

$$D(1mbar) = \frac{1\,mm * 5\,mbar}{0.9\,mm * 3.5\,mbar} \simeq 1.6\,nm_{eq} \tag{3.4}$$

Indeed, when looking at the cross-section data, we find that the gas phase cross-section σ_{GP}= $3 \times 10^{-16}\,\mathrm{cm}^{-2}$ [85] is larger than the cross-section for ice σ_{ice}=1.5-$2 \times 10^{-16}\,\mathrm{cm}^{-2}$ [86], for electrons with KE=500 eV, which confirms the 1.6 factor found in Equation 3.4. Intuitively, we can understand that the cross-section of electrons in ice is lower than in gas-phase water because the molecules in ice are overlapping, creating hexagonal channels of perfect vacuum where electrons can freely travel as has been observed with helium atoms [22, 33].

Using this calibration, (Equation 3.4) the simulation allows us to calculate the mean probing depth of different KE windows, as a function of pressure, as shown in Figure 3.5 and establishes the relationship between pressure and MPD. While in vacuum, lowering the KE window increases the MPD (Equation 3.2), increasing the pressure decreases the MPD, for KE windows containing scattered electrons. In Figure 3.5, we can see different KE windows, corresponding to [84] (412-437 eV), [47] (430-450 eV, and the full kinetic window acquired in this work (425-525 eV). There is some noise at the high-pressure side of the graph, and this is expected because the simulation has fewer data points to calculate the MDP from. All MDP curves seem to converge towards the non-scattering case value ($\lambda = 2.2\,nm$), and this makes sense because the ratio between gas phase and ice scattering increases with pressure, such that when the pressure tends to infinity pressure, the finite number of scattering events in the gas phase forces the number of scattering in the condensed phase to tend towards 0.

The fact that the probing depth decreases with pressure is particularly relevant for interpreting the temperature dependence of the QLL thickness, because the measurement pressure increases as temperature increases. Pressure acts then as a confounding factor: the QLL thickness estimation could increase due to the shorter MPD at high pressure. For this reason, it is important to precisely quantify the impact of the gas phase on the MPD and therefore on the thickness calibration, in order to make sound conclusions.

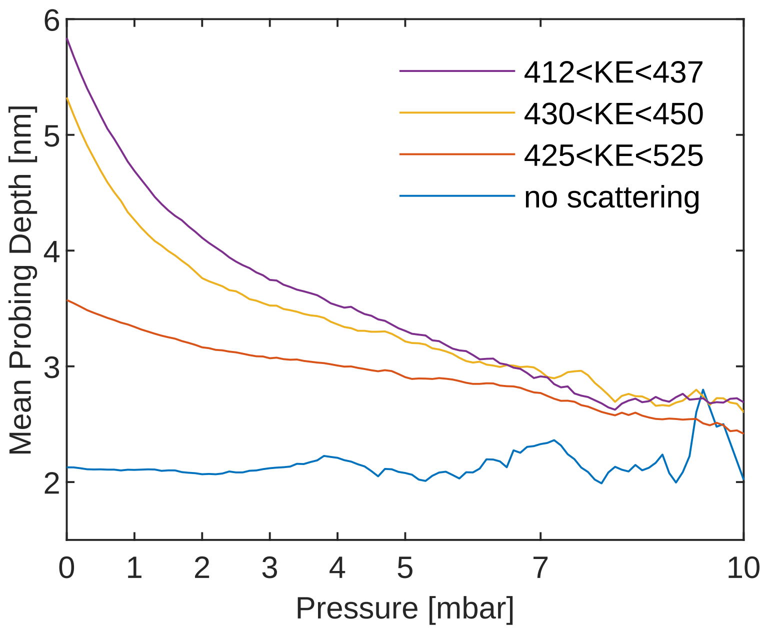

FIGURE 3.5: Mean probing depth as a function of pressure on the 1 mm path from the ice surface to the aperture of the electron analyzer. The pressure is calibrated with Equation 3.4 i.e. 1 mbar=1.6 nm$_{eq}$. The legend indicates a subset among the detected electrons with specific properties, for example, electrons that have a kinetic energy within the specified KE window or electrons that have not scattered along their path.

Supporting Figure 3.14 compares the experimental Auger spectra of ice at different pressures (data corresponding to Figure 3.2, with the additional spectra of ice at -40°C (0.12 mbar)) with the Auger spectra obtained from the Monte-Carlo simulation at the corresponding pressures. The key to understanding the probing depth in PEY-XAS is the background region of the Auger spectra. On supporting Figure 3.14, we see that it is heavily influenced by gas phase scattering. On supporting Figure 3.14a, we see the sharp gas phase peak at KE=500 eV (that we have seen in Figure 1(a) of [70]), visible from a pressure of 2.36 mbar. The wider Auger emission peaks of the ice are visible at 0.12 mbar, but are already almost fully scattered at 2.36 mbar and above. In the simulation, the Auger emission peaks stay visible even at high pressure. In addition, the variation of the Auger background with increasing pressure generally agrees between the simulation and the experiment, the most notable difference being in the shape of the background at high pressure (the simulation data produce a very 'linear' background while the experimental data yields a more 'curvy' background). Most probably, this indicates that the average loss of KE per scattering event $\langle T_{loss} \rangle \simeq$ 60 eV is overestimated. In that case, the MPD is underestimated (Equation 3.2) and the QLL thickness calibration would yield a thicker thickness estimation. Another source of uncertainty is related to the large amount of 2$^{\text{nd}}$ order light, which contribute to the auger yield and could potentially impact the shape of auger spectra. Nevertheless, the simulation allows to reproduce the general behavior of the background of the Auger spectra due to gas phase scattering.

Calibration curves Suppose now that we have a system consisting of a layer of thickness D, containing atoms A, sitting on top of a bulk containing atoms B. The relative contribution of A to the total signal is obtained by integrating the probing depth distribution from 0 to D. In the case where electrons do not scatter, one can derive analytically:

$$\frac{I_A}{I_A + I_B} = \frac{1}{\lambda} \int_0^D e^{-\frac{z}{\lambda}} dz = 1 - e^{-\frac{D}{\lambda}} \tag{3.5}$$

where λ is the IMFP of electron at KE=500 eV. The factor $\frac{1}{\lambda}$ is a normalization factor necessary to ensure that for $D \rightarrow \infty$, $\frac{I_A}{I_A+I_B} \rightarrow 1$. For scattered electrons, we can use the probing depth distribution that the MC simulation provides for a specific KE window and pressure, (one example of probing depth distribution is shown in Figure 3.4, left panel) and integrate it along the depth axis until the integral (expressed in % of the total integral) equal signal A (the relative contribution of A to the total signal). If signal A = 50%, then the depth at which the integral reaches 50% is the median of the distribution. Figure 3.6 shows the calibration curves that allow converting the signal A, into the thickness of layer A. For example, the QLL signal[4] relative to the total signal ($I_{QLL} + I_{ice}$) as measured in PEY-XAS. In UHV and considering only non-scattered electrons (green line), the simulation reproduces the analytical calculation (Equation 3.5, black line) and covers the kinetic energy windows where an analytical solution is not trivial.

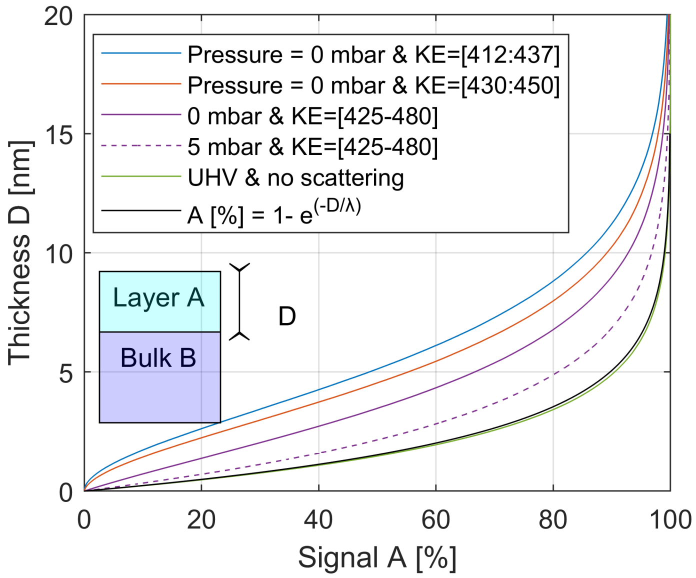

FIGURE 3.6: Calibration curves to convert the signal A, derived from a PEY-XAS measurement and expressed in [%], into the thickness D of layer A. Derived from the simulated probing depth distributions.

In 2002, Bluhm et al. [56] measured the QLL on ice with PEY-XAS, using a KE window from 412 to 437 eV. According to the simulation, the thickness of the QLL is given by the blue curve for this KE window and in UHV, and the scattering effect

---

[4] The liquid-like character that we can measure on ice with PEY-XAS originates from the QLL that we assume to be a fully liquid layer

increases the calculated thickness by a factor ~ 3 compared to the case when one would not consider scattering (green curve). In 2017, Bartels-Rausch et al. [47], investigated the formation of solvation shells on ice with PEY-XAS, using a KE window that was either 430 to 450 eV or 450 to 470 eV (not clear, since both are mentioned in the main text) so the PEY-XAS probing depth might have been underestimated by a factor 2 to 3.

The precise knowledge of scattering in matter allow to derive the curves from Figure 3.6 and therefore PEY-XAS can probe different depths by choosing the right kinetic energy window.

3.1.3.3 *QLL thickness using the simulation results*

Data from a large dataset (including the spectra from Figure 3.2) are deconvoluted [87][5] and the Gaussian peak model (Section 3.2.3) allows to assign the contributions to water molecules in dangling OH (pre-edge), disordered (main edge) or tetrahedral (post edge) configurations. The disorder of the hydrogen-bonding network can be observed both as an increase in the pre-edge and as an increase in the main to post-edge ratio (see Figure 3.2. Only the data averaged from at least 2 PEY-XAS spectra having a fair reproducibility (see supporting Section 3.2.1) are further processed. One can calculate the proportion of 'pure liquid' within the probing depth (which depends on the KE window and pressure) as follow:

$$SignalA[\%] = \frac{I - I_{cold}}{I_{liq.} - I_{cold}} \tag{3.6}$$

where I is the intensity of the pre-edge or main-to-post edge ratio (depending on what observable we wish to base the calculation), and the subscripts *cold* and *liq.* indicate the intensity of this same observable for reference cold ice (-40°C, assumed to have no QLL) and liquid water, respectively. We then use the calibration curves (Figure 3.6) from MC simulation to convert this information into the QLL thickness, with the assumption that the QLL is a homogeneous liquid layer.

Figure 3.7 shows the QLL thickness calculated from different methods. In blue empty circles, the measured pre-edge intensity data is directly converted to thickness without considering electron scattering; in blue empty triangles, the pre-edge intensity data is converted into thickness considering electron scattering, but no MDP reduction due to the presence of the gas phase molecules; in blue filled circles, the pre-edge intensity data is converted into thickness considering the full electron scattering calibration; in red filled circles, the main-to-post-edge ratio data is converted into thickness considering the full electron scattering calibration; and finally, in green empty circles, Bluhm's data from 2002 (pre-edge intensity data converted to QLL thickness without considering electron scattering).

All data sets are fitted with the theoretical shape of the QLL [16]:

$$Thickness = A \cdot t^{-\frac{1}{3}} - B \tag{3.7}$$

---

[5] inspired by [53] and [60].

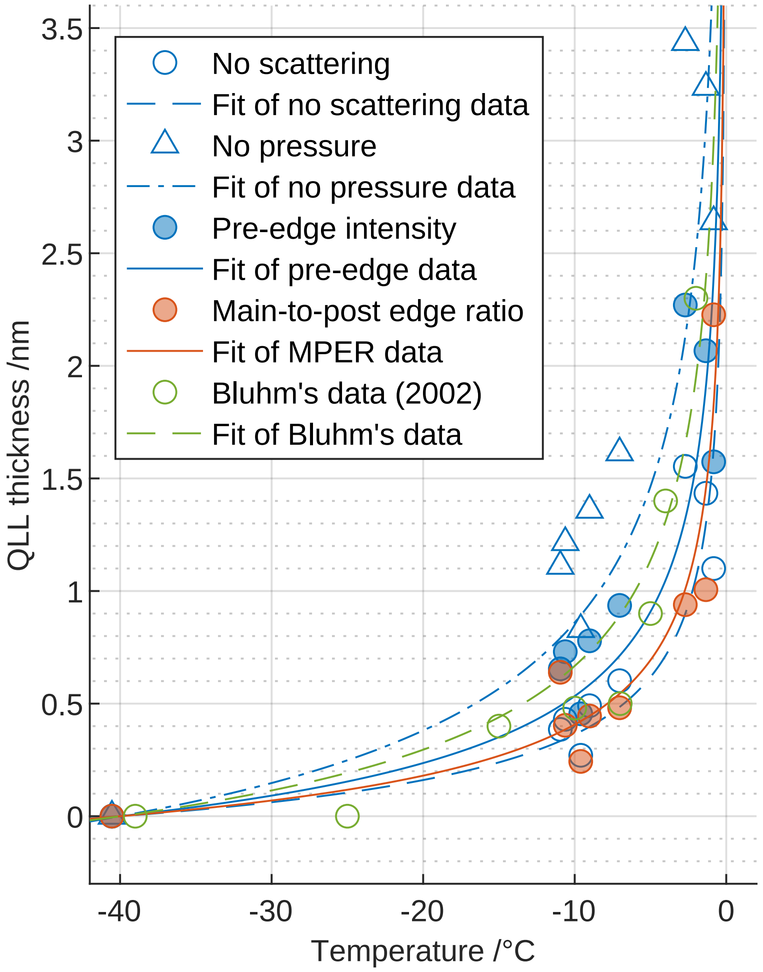

FIGURE 3.7: QLL thicknesses calculated from (in blue) the pre-edge intensity and (in red) the main-to-post-edge ratio together with (green) Bluhm's data [84]. The empty circles designate analysis without considering electron scattering in the probing depth assessment, the empty triangle refers to the analysis of the data taking into consideration electron scattering in the ice only (no gas phase scattering), and the filled circle designates the improved analysis considering electron scattering both in the ice and in the gas phase. Fit according to the theoretical shape of the QLL temperature dependence [16] is shown for each data set.

where $t = (T_m - T)/T_m$ is the reduced temperature, A is a constant. B is set such that the QLL thickness equals 0 at -40°C.

The improved data analysis (including electron scattering) provides a larger thickness estimation than the analysis ignoring electron scattering (blue-filled circles compared to empty blue circles).

Carbon is always present in uncontrolled trace amounts, see supporting Section 3.2.3 and is known to affect the PEY-XAS measurement [56]. The deconvolution results are very sensitive to the input parameters and a slight change in position in 1 gaussian can greatly affect the amplitude of the others. The pre-edge intensity is probably the feature that is the most exposed to deconvolution error, as it is in between the gas phase emission peaks and in between the C=O and main edge. The main-to-post-edge ratio provides a more reliable observable. On Figure 3.7, the QLL thicknesses calculated with the main-to-post-edge ratio (red filled circles) are the most consistent: increasing with temperature (when the QLL thickness calculated with the pre-edge intensity is decreasing from -3°C to -1°C). Regarding the pre-edge intensity derived QLL thickness, there is good agreement between Bluhm and this work when scattering is not taken into account (empty blue and green circles). We can also note in the graph that if Bluhm would have used the calibration curve for the kinetic energy range that he used (412-437 eV), his data points would be shifted upwards. The difference between the filled blue and red circles, i.e. between our improved analysis using both pre-edge intensity and main-to-post-edge ratio, gives an idea of the uncertainty of our analysis. In particular, the pure ice and liquid references are critical since the QLL signal is interpreted relatively to these measurements. In addition, since the pre-edge is associated with the dangling OH at the very surface of the ice, it might be better to measure this signal at a KE closer to the emission KE (close to 500eV). This observable might then give a more reliable signal.

If we rely on the main-to-post-edge ratio results (red data points in Figure 3.7), we find about the same results as reported by Bluhm [84] at around -10°C and a rather thinner thickness between -10 and 0°C. Molecular dynamics simulations have also reported a very thin QLL thickness [19].

3.1.4 *Conclusion and outlook*

Our data with improved probing depth calibration with respect to electron scattering and analysis suggests that the QLL thickness is rather small, and increases from 0.5 to 2 nanometers in the range from -10°C to -1°C. This suggests that in the case of clean ice, the QLL would enhance chemical interactions only when the temperature is close to the melting point and the QLL would provide less volume for quasi-aqueous chemistry on ice than previously assumed [2, 88]. Note that 0.5 nm also corresponds to the overall accuracy of the technique, given the many uncertainties described in the main text. In terms of water molecules, 0.5 nm is equal to approximately 1.5 bilayers of ice, which is already considerable for ice-air interaction. This reminds us that electron spectroscopy and especially PEY-XAS are not overly surface sensitive. However, we note that the thickness deduced here with the refined analysis is consistent with the most recent AFM [50] and SFG [32] data that may all have somewhat higher surface sensitivity.

Next, we discussed the role of choosing the kinetic energy window in the analyzer settings, and how this could be a tool instead of representing another uncertainty source. We explored the effect of gas phase pressure on the probing depth. Another consequence of the inelastic scattering contribution is that the electron kinetic energy, which we can precisely measure in PEY-XAS, contains depth information.

Impact of pressure There is an inherent link between QLL thickness and the vapor pressure: the higher the temperature the more you loosen the H-bonds and also the higher the vapor pressure is, they just go along with each other. However, gas phase scattering reduces the probing depth and therefore increases the surface sensitivity. It is hence a confounding factor and shall not be neglected. Once corrected, we can still argue that the QLL increase is due to absolute pressure: because of the mechanical collision on the surface of the ice meaning that in the environment, with 100-1000 mbar of pressure, the QLL could be much larger than the few nm that we observe in 0.1-5 mbar XAS. This makes a lot of sense when we imagine the flux of water molecules at equilibrium on the surface of the ice. At warmer temperatures, the traffic is much more intense than at low temperatures and the surface gets bombarded with molecules. Although a complete study on the effect of pressure and QLL thickness is outside the scope of this work, future experiments should be performed to investigate pressure dependence, i.e. maintaining the same water saturation pressure while the total pressure is increased and with an effort to reduce data uncertainty. More on this in Section 5.3.

PEY-XAS depth profile

In addition to improving the depth calibration and reducing the associated uncertainty, our work reminds us that PEY-XAS can be used for depth profiling i.e. by playing with the KE windows, as demonstrated in recent work on multi-layered silicon oxide samples [89, 90].

For the ice sample, this means that one could probe different regions of the interface merely with PEY-XAS. This, combined with the conventional XPS depth profile, would be very powerful to characterize acid-base chemistry on ice with raising questions of physisorption, chemisorption and solvation shells. More on this in Section 5.2.

References

1. Rignot, E., Kwok, R., Willis, J. & Velicogna, I. *Global Climate Change: Evidence.* Web Page.
2. Grannas, A. M., Jones, A. E., Dibb, J., Ammann, M., Anastasio, C., Beine, H. J., Bergin, M., Bottenheim, J., Boxe, C. S., Carver, G., Chen, G., Crawford, J. H., Domine, F., Frey, M. M., Guzman, M. I., Heard, D. E., Helmig, D., Hoffmann, M. R., Honrath, R. E., Huey, L. G., Hutterli, M., Jacobi, H. W., Klan, P., Lefer, B., McConnell, J., Plane, J., Sander, R., Savarino, J., Shepson, P. B., Simpson, W. R., Sodeau, J. R., von Glasow, R., Weller, R., Wolff, E. W. & Zhu, T. "An overview of snow photochemistry: evidence, mechanisms and impacts". *Atmospheric Chemistry and Physics* **7**, 4329–4373 (2007).
3. Cantrell, W. & Heymsfield, A. "Production of Ice in Tropospheric Clouds: A Review". *Bulletin of the American Meteorological Society* **86**, 795–808 (2005).
4. Lohmann, U. & Feichter, J. "Global indirect aerosol effects: a review". *Atmospheric Chemistry and Physics* **5**, 715–737 (2005).
5. Boucher, O., Randall, D., Artaxo, P., Bretherton, C., Feingold, G., Forster, P., Kerminen, V.-M., Kondo, Y., Liao, H., Lohmann, U., *et al.* in *Climate change 2013: the physical science basis. Contribution of Working Group I to the Fifth Assessment Report of the Intergovernmental Panel on Climate Change* 571–657 (Cambridge University Press, 2013).
6. Bartels-Rausch, T., Jacobi, H. W., Kahan, T. F., Thomas, J. L., Thomson, E. S., Abbatt, J. P. D., Ammann, M., Blackford, J. R., Bluhm, H., Boxe, C., Domine, F., Frey, M. M., Gladich, I., Guzman, M. I., Heger, D., Huthwelker, T., Klan, P., Kuhs, W. F., Kuo, M. H., Maus, S., Moussa, S. G., McNeill, V. F., Newberg, J. T., Pettersson, J. B. C., Roeselova, M. & Sodeau, J. R. "A review of air-ice chemical and physical interactions (AICI): liquids, quasi-liquids, and solids in snow". *Atmospheric Chemistry and Physics* **14**, 1587–1633 (2014).
7. Bartels-Rausch, T., Wren, S. N., Schreiber, S., Riche, F., Schneebeli, M. & Ammann, M. "Diffusion of volatile organics through porous snow: impact of surface adsorption and grain boundaries". *Atmospheric Chemistry and Physics* **13**, 6727–6739 (2013).
8. Huthwelker, T., Ammann, M. & Peter, T. "The Uptake of Acidic Gases on Ice". *Chemical Reviews* **106**, 1375–1444 (2006).
9. Neu, J. & Prather, M. "Toward a more physical representation of precipitation scavenging in global chemistry models: cloud overlap and ice physics and their impact on tropospheric ozone". *Atmospheric Chemistry and Physics* **12**, 3289–3310 (2012).
10. Müller, R., Crutzen, P. J., Grooß, J.-U., Brühl, C., Russell III, J. M. & Tuck, A. F. "Chlorine activation and ozone depletion in the Arctic vortex: Observations by the Halogen Occultation Experiment on the Upper Atmosphere Research Satellite". *Journal of Geophysical Research: Atmospheres* **101**, 12531–12554 (1996).

11. Müller, R., Crutzen, P. J., Groo, J.-U., Bürhl, C., Russell, J. M., Gernandt, H., McKenna, D. S. & Tuck, A. F. "Severe chemical ozone loss in the Arctic during the winter of 1995–96". *Nature* **389**, 709–712 (1997).
12. Poole, L. R. & McCormick, M. P. "Polar stratospheric clouds and the Antarctic ozone hole". *Journal of Geophysical Research: Atmospheres* **93**, 8423–8430 (1988).
13. Tilmes, S., Müller, R., Engel, A., Rex, M. & Russell III, J. M. "Chemical ozone loss in the Arctic and Antarctic stratosphere between 1992 and 2005". *Geophysical research letters* **33** (2006).
14. Faraday, M. *Philosophical Magazine* **17**, 162 (1840).
15. Faraday, M. "I. Note on regelation". *Proceedings of the Royal Society of London* **10**, 440–450 (1860).
16. Dash, J. G., Fu, H. Y. & Wettlaufer, J. S. "The Premelting of Ice and Its Environmental Consequences". *Reports on Progress in Physics* **58**, 115–167 (1995).
17. Henson, B. F. & Robinson, J. M. "Dependence of Quasiliquid Thickness on the Liquid Activity: A Bulk Thermodynamic Theory of the Interface". *Physical Review Letters* **92**, 246107 (2004).
18. Kvlividze, V., Kiselev, V., Kurzaev, A. & Ushakova, L. "The mobile water phase on ice surfaces". *Surface Science* **44**, 60–68 (1974).
19. Conde, M. M., Vega, C. & Patrykiejew, A. "The thickness of a liquid layer on the free surface of ice as obtained from computer simulation". *Journal of Chemical Physics* **129** (2008).
20. Döppenschmidt, A. & Butt, H.-J. "Measuring the Thickness of the Liquid-like Layer on Ice Surfaces with Atomic Force Microscopy". *Langmuir* **16**, 6709–6714 (2000).
21. Dosch, H., Lied, A. & Bilgram, J. H. "Glancing-angle X-ray scattering studies of the premelting of ice surfaces". *Surface Science* **327**, 145–164 (1995).
22. Glebov, A., Graham, A. P., Menzel, A., Toennies, J. P. & Senet, P. "A helium atom scattering study of the structure and phonon dynamics of the ice surface". *The Journal of Chemical Physics* **112**, 11011–11022 (2000).
23. Goertz, M. P., Zhu, X. Y. & Houston, J. E. "Exploring the Liquid-like Layer on the Ice Surface". *Langmuir* **25**, 6905–6908 (2009).
24. Kietzig, A.-M., Hatzikiriakos, S. & Englezos, P. *Physics of ice friction* 081101–081101 (2010).
25. Kouchi, A., Furukawa, Y. & Kuroda, T. "X-ray diffraction pattern of quasi-liquid layer on ice crystal surface" (1987).
26. Maeno, N. & Nishimura, H. "The Electrical Properties of Ice Surfaces". *Journal of Glaciology* **21**, 193–205 (2017).
27. Murata, K.-i., Asakawa, H., Nagashima, K., Furukawa, Y. & Sazaki, G. "Thermodynamic origin of surface melting on ice crystals". *Proceedings of the National Academy of Sciences* **113**, E6741–E6748 (2016).

28. Nagata, Y., Hama, T., Backus, E. H. G., Mezger, M., Bonn, D., Bonn, M. & Sazaki, G. "The Surface of Ice under Equilibrium and Nonequilibrium Conditions". *Accounts of Chemical Research* (2019).
29. Petrenko, V. F. & Ryzhkin, I. A. "Surface states of charge carriers and electrical properties of the surface layer of ice". *Journal of Physical Chemistry B* **101**, 6285–6289 (1997).
30. Pickering, I., Paleico, M., Sirkin, Y. A. P., Scherlis, D. A. & Factorovich, M. H. "Grand Canonical Investigation of the Quasi Liquid Layer of Ice: Is It Liquid?" *The Journal of Physical Chemistry B* **122**, 4880–4890 (2018).
31. Pittenger, B., Fain, S. C., Cochran, M. J., Donev, J. M. K., Robertson, B. E., Szuchmacher, A. & Overney, R. M. "Premelting at ice-solid interfaces studied via velocity-dependent indentation with force microscope tips". *Physical Review B* **63**, 134102 (2001).
32. Sanchez, M. A., Kling, T., Ishiyama, T., van Zadel, M. J., Bisson, P. J., Mezger, M., Jochum, M. N., Cyran, J. D., Smit, W. J., Bakker, H. J., Shultz, M. J., Morita, A., Donadio, D., Nagata, Y., Bonn, M. & Backus, E. H. G. "Experimental and theoretical evidence for bilayer-by-bilayer surface melting of crystalline ice". *Proceedings of the National Academy of Sciences of the United States of America* **114**, 227–232 (2017).
33. Suter, M. T., Andersson, P. U. & Pettersson, J. B. C. "Surface properties of water ice at 150–191K studied by elastic helium scattering". *The Journal of Chemical Physics* **125**, 174704 (2006).
34. Dash, J. G., Rempel, A. W. & Wettlaufer, J. S. "The physics of premelted ice and its geophysical consequences". *Reviews of Modern Physics* **78**, 695–741 (2006).
35. Rosenberg, R. "Why Is Ice Slippery?" *Physics Today* **58**, 50–54 (2005).
36. Abbatt, J. P. "Interactions of atmospheric trace gases with ice surfaces: Adsorption and reaction". *Chemical reviews* **103**, 4783–4800 (2003).
37. Bartels-Rausch, T., Bergeron, V., Cartwright, J. H. E., Escribano, R., Finney, J. L., Grothe, H., Gutierrez, P. J., Haapala, J., Kuhs, W. F., Pettersson, J. B. C., Price, S. D., Sainz-Diaz, C. I., Stokes, D. J., Strazzulla, G., Thomson, E. S., Trinks, H. & Uras-Aytemiz, N. "Ice structures, patterns, and processes: A view across the icefields". *Reviews of Modern Physics* **84**, 885–944 (2012).
38. Pouvesle, N., Kippenberger, M., Schuster, G. & Crowley, J. N. "The interaction of H2O2 with ice surfaces between 203 and 233 K". *Physical Chemistry Chemical Physics* **12**, 15544–15550 (2010).
39. Zimmermann, S., Kippenberger, M., Schuster, G. & Crowley, J. N. "Adsorption isotherms for hydrogen chloride (HCl) on ice surfaces between 190 and 220 K". *Physical Chemistry Chemical Physics* **18**, 13799–13810 (2016).
40. Bartels-Rausch, T., Orlando, F., Kong, X. R., Artiglia, L. & Ammann, M. "Experimental Evidence for the Formation of Solvation Shells by Soluble Species at a Nonuniform Air-Ice Interface". *Acs Earth and Space Chemistry* **1**, 572–579 (2017).

41. Gladich, I., Pfalzgraff, W., Marsalek, O., Jungwirth, P., Roeselova, M. & Neshyba, S. “Arrhenius analysis of anisotropic surface self-diffusion on the prismatic facet of ice”. *Physical Chemistry Chemical Physics* **13**, 19960–19969 (2011).

42. Kong, X., Waldner, A., Orlando, F., Artiglia, L., Huthwelker, T., Ammann, M. & Bartels-Rausch, T. “Coexistence of Physisorbed and Solvated HCl at Warm Ice Surfaces”. *J Phys Chem Lett* **8**, 4757–4762 (2017).

43. Krepelova, A., Bartels-Rausch, T., Brown, M. A., Bluhm, H. & Ammann, M. “Adsorption of Acetic Acid on Ice Studied by Ambient-Pressure XPS and Partial-Electron-Yield NEXAFS Spectroscopy at 230-240 K”. *Journal of Physical Chemistry A* **117**, 401–409 (2013).

44. McNeill, V. F., Loerting, T., Geiger, F. M., Trout, B. L. & Molina, M. J. “Hydrogen chloride-induced surface disordering on ice”. *Proceedings of the National Academy of Sciences of the United States of America* **103**, 9422–9427 (2006).

45. Waldner, A., Artiglia, L., Kong, X. R., Orlando, F., Huthwelker, T., Ammann, M. & Bartels-Rausch, T. “Pre-melting and the adsorption of formic acid at the air-ice interface at 253 K as seen by NEXAFS and XPS”. *Physical Chemistry Chemical Physics* **20**, 24408–24417 (2018).

46. Brini, E., Fennell, C. J., Fernandez-Serra, M., Hribar-Lee, B., Luksic, M. & Dill, K. A. “How Water’s Properties Are Encoded in Its Molecular Structure and Energies”. *Chemical Reviews* **117**, 12385–12414 (2017).

47. Bartels-Rausch, T., Orlando, F., Kong, X., Artiglia, L. & Ammann, M. “Experimental Evidence for the Formation of Solvation Shells by Soluble Species at a Nonuniform Air–Ice Interface”. *ACS Earth and Space Chemistry* **1**, 572–579 (2017).

48. Waldner, A. *Molecular level picture of the interaction between ice and trace gases* Thesis (2017).

49. Sazaki, G., Zepeda, S., Nakatsubo, S., Yokomine, M. & Furukawa, Y. “Quasi-liquid layers on ice crystal surfaces are made up of two different phases”. *Proceedings of the National Academy of Sciences* **109**, 1052–1055 (2012).

50. Constantin, J. G., Gianetti, M. M., Longinotti, M. P. & Corti, H. R. “The quasi-liquid layer of ice revisited: the role of temperature gradients and tip chemistry in AFM studies”. *Atmospheric Chemistry and Physics* **18**, 14965–14978 (2018).

51. Furukawa, Y., Yamamoto, M. & Kuroda, T. “Ellipsometric Study of the Ice Surface-Structure Just Below the Melting-Point”. *Journal De Physique* **48**, 495–501 (1987).

52. Furukawa, Y., Yamamoto, M. & Kuroda, T. “Ellipsometric Study of the Transition Layer on the Surface of an Ice Crystal”. *Journal of Crystal Growth* **82**, 665–677 (1987).

53. Nilsson, A., Nordlund, D., Waluyo, I., Huang, N., Ogasawara, H., Kaya, S., Bergmann, U., Naslund, L. A., Ostrom, H., Wernet, P., Andersson, K. J., Schiros, T. & Pettersson, L. G. M. “X-ray absorption spectroscopy and X-ray Raman scattering of water and ice; an experimental view”. *Journal of Electron Spectroscopy and Related Phenomena* **177**, 99–129 (2010).

54. Niskanen, J., Fondell, M., Sahle, C. J., Eckert, S., Jay, R. M., Gilmore, K., Pietzsch, A., Dantz, M., Lu, X., McNally, D. E., Schmitt, T., Vaz da Cruz, V., Kimberg, V., Gel'mukhanov, F. & Föhlisch, A. "Compatibility of quantitative X-ray spectroscopy with continuous distribution models of water at ambient conditions". *Proceedings of the National Academy of Sciences* **116**, 4058–4063 (2019).
55. Frati, F., Hunault, M. O. & de Groot, F. M. "Oxygen K-edge X-ray absorption spectra". *Chemical reviews* **120**, 4056–4110 (2020).
56. Bluhm, H., Ogletree, D. F., Fadley, C. S., Hussain, Z. & Salmeron, N. "The premelting of ice studied with photoelectron spectroscopy". *Journal of Physics-Condensed Matter* **14**, L227–L233 (2002).
57. Bergmann, U., Wernet, P., Glatzel, P., Cavalleri, M., Pettersson, L., Nilsson, A. & Cramer, S. "X-ray Raman spectroscopy at the oxygen K edge of water and ice: Implications on local structure models". *Physical Review B* **66**, 092107 (2002).
58. Cavalleri, M., Ogasawara, H., Pettersson, L. & Nilsson, A. "The interpretation of X-ray absorption spectra of water and ice". *Chemical Physics Letters* **364**, 363–370 (2002).
59. Tse, J. S., Shaw, D. M., Klug, D. D., Patchkovskii, S., Vankó, G., Monaco, G. & Krisch, M. "X-Ray Raman Spectroscopic Study of Water in the Condensed Phases". *Physical Review Letters* **100**, 095502 (2008).
60. Cappa, C. D., Smith, J. D., Wilson, K. R., Messer, B. M., Gilles, M. K., Cohen, R. C. & Saykally, R. J. "Effects of alkali metal halide salts on the hydrogen bond network of liquid water". *Journal of Physical Chemistry B* **109**, 7046–7052 (2005).
61. Geissler, P. L. "Temperature Dependence of Inhomogeneous Broadening: On the Meaning of Isosbestic Points". *Journal of the American Chemical Society* **127**, 14930–14935 (2005).
62. Kong, X. R., Waldner, A., Orlando, F., Artiglia, L., Huthwelker, T., Ammann, M. & Bartels-Rausch, T. "Coexistence of Physisorbed and Solvated HCI at Warm Ice Surfaces". *Journal of Physical Chemistry Letters* **8**, 4757–4762 (2017).
63. Orlando, F., Artiglia, L., Yang, H. Y., Kong, X. R., Roy, K., Waldner, A., Chen, S. Z., Bartels-Rausch, T. & Ammann, M. "Disordered Adsorbed Water Layers on TiO2 Nanoparticles under Subsaturated Humidity Conditions at 235 K". *Journal of Physical Chemistry Letters* **10**, 7433–7438 (2019).
64. Orlando, F., Waldner, A., Bartels-Rausch, T., Birrer, M., Kato, S., Lee, M. T., Proff, C., Huthwelker, T., Kleibert, A., van Bokhoven, J. & Ammann, M. "The Environmental Photochemistry of Oxide Surfaces and the Nature of Frozen Salt Solutions: A New in Situ XPS Approach". *Topics in Catalysis* **59**, 591–604 (2016).
65. Bluhm, H. "Photoelectron spectroscopy of surfaces under humid conditions". *Journal of Electron Spectroscopy and Related Phenomena* **177**, 71–84 (2010).
66. Tougaard, S. "Energy loss in XPS: Fundamental processes and applications for quantification, non-destructive depth profiling and 3D imaging". *Journal of Electron Spectroscopy and Related Phenomena* **178**, 128–153 (2010).

67. Werner, W. S. M. "Electron transport in solids for quantitative surface analysis". *Surface and Interface Analysis* **31**, 141–176 (2001).

68. Frank Ogletree, D., Bluhm, H., Hebenstreit, E. D. & Salmeron, M. "Photoelectron spectroscopy under ambient pressure and temperature conditions". *Nuclear Instruments and Methods in Physics Research Section A: Accelerators, Spectrometers, Detectors and Associated Equipment* **601**, 151–160 (2009).

69. Marti, J. & Mauersberger, K. "A survey and new measurements of ice vapor pressure at temperatures between 170 and 250K". *Geophysical Research Letters* **20**, 363–366 (1993).

70. Saak, C.-M., Unger, I., Gopakumar, G., Caleman, C. & Björneholm, O. "Temperature Dependence of X-ray-Induced Auger Processes in Liquid Water". *The Journal of Physical Chemistry Letters* **11**, 2497–2501 (2020).

71. Liegener, C.-M. & Chen, R. "Calculation of the Auger spectrum of liquid water". *The Journal of Chemical Physics* **88**, 2618–2623 (1988).

72. Carravetta, V. & gren, H. "Stieltjes imaging method for molecular Auger transition rates: Application to the Auger spectrum of water". *Physical Review A* **35**, 1022–1032 (1987).

73. Inhester, L., Burmeister, C. F., Groenhof, G. & Grubmüller, H. "Auger spectrum of a water molecule after single and double core ionization". *The Journal of Chemical Physics* **136**, 144304 (2012).

74. Siegbahn, H., Asplund, L. & Kelfve, P. "Auger-Electron Spectrum of Water-Vapor". *Chemical Physics Letters* **35**, 330–335 (1975).

75. Nilsson, A., Nordlund, D., Waluyo, I., Huang, N., Ogasawara, H., Kaya, S., Bergmann, U., Naslund, L. A., Ostrom, H., Wernet, P., Andersson, K. J., Schiros, T. & Pettersson, L. G. M. "X-ray absorption spectroscopy and X-ray Raman scattering of water and ice; an experimental view". *Journal of Electron Spectroscopy and Related Phenomena* **177**, 99–129 (2010).

76. Wernet, P., Nordlund, D., Bergmann, U., Cavalleri, M., Odelius, M., Ogasawara, H., Näslund, L. Å., Hirsch, T. K., Ojamäe, L., Glatzel, P., Pettersson, L. G. M. & Nilsson, A. "The Structure of the First Coordination Shell in Liquid Water". *Science* **304**, 995–999 (2004).

77. Ottosson, N., Faubel, M., Bradforth, S. E., Jungwirth, P. & Winter, B. "Photoelectron spectroscopy of liquid water and aqueous solution: Electron effective attenuation lengths and emission-angle anisotropy". *Journal of Electron Spectroscopy and Related Phenomena* **177**, 60–70 (2010).

78. Tanuma, S., Powell, C. J. & Penn, D. R. "Calculations of electron inelastic mean free paths. V. Data for 14 organic compounds over the 50–2000 eV range". *Surface and Interface Analysis* **21**, 165–176 (1994).

79. Seah, M. & Dench, W. "Surf. Interface Anal" (1979).

80. Shinotsuka, H., Da, B., Tanuma, S., Yoshikawa, H., Powell, C. J. & Penn, D. R. "Calculations of electron inelastic mean free paths. XI. Data for liquid water for energies from 50eV to 30keV". *Surface and Interface Analysis* **49**, 238–252 (2017).

81. Tougaard, S. “Universality Classes of Inelastic Electron Scattering Cross-sections”. *Surface and Interface Analysis* **25**, 137–154 (1997).

82. Werner, W., Smekal, W. & Powell, C. J. *Simulation of Electron Spectra for Surface Analysis (SESSA) - 2.1.1* (National Institute of Standards and Technology, Gaithersburg, MD, 2018).

83. Chen, W., Wu, X. & Car, R. “X-ray absorption signatures of the molecular environment in water and ice”. *Physical review letters* **105**, 017802 (2010).

84. Bluhm, H., Ogletree, D. F., Fadley, C. S., Hussain, Z. & Salmeron, N. “The premelting of ice studied with photoelectron spectroscopy”. *Journal of Physics-Condensed Matter* **14**, L227–L233 (2002).

85. Muñoz, A., Oller, J. C., Blanco, F., Gorfinkiel, J. D., Limão-Vieira, P. & García, G. “Electron-scattering cross sections and stopping powers in H_2O”. *Physical Review A* **76**, 052707 (2007).

86. Tımneanu, N., Caleman, C., Hajdu, J. & van der Spoel, D. “Auger electron cascades in water and ice”. *Chemical Physics* **299**, 277–283 (2004).

87. Yang, H., Boucly, A., Gabathuler, J. P., Bartels-Rausch, T., Artiglia, L. & Ammann, M. “Ordered Hydrogen Bonding Structure of Water Molecules Adsorbed on Silver Iodide Particles under Subsaturated Conditions”. *The Journal of Physical Chemistry C* **125**, 11628–11635 (2021).

88. Kuo, M., Moussa, S. & McNeill, V. “Modeling interfacial liquid layers on environmental ices”. *Atmospheric Chemistry and Physics* **11**, 9971–9982 (2011).

89. Isomura, N., Cui, Y. T., Murai, T., Oji, H. & Kimoto, Y. “X-ray absorption spectroscopy to determine originating depth of electrons that form an inelastic background of Auger electron spectrum”. *Journal of Applied Physics* **122** (2017).

90. Isomura, N., Soejima, N., Iwasaki, S., Nomoto, T., Murai, T. & Kimoto, Y. “Depth-selective X-ray absorption spectroscopy by detection of energy-loss Auger electrons”. *Applied Surface Science* **355**, 268–271 (2015).

Supporting information for the manuscript in preparation, which will be published as: Gabathuler, J. P., Yang, H., Manoharan, Y., Boucly, A., Alpert, P. A., Artiglia, L., Bartels-Rausch, T. & Ammann, M. "The premelting of ice revisited with X-ray absorption spectroscopy" (in preparation)

3.2 SUPPORTING INFORMATION

3.2.1 *PEY-XAS analysis*

There is a variability from beamtime to beamtime due to different alignments (which impacts the background), different contamination levels (adventitious carbon is know to induce disorder on the surface, and it contains oxygen which contributes to the XAS spectra), different ice thickness (which can impact charging, thermal conduction, crater size). Therefore, I choose to never mix data from different beamtimes or different ice samples. In the main text, Figure 3.2, the data is processed with the following steps:

- Import - the first step is to import the data from the h5 structure, which is the output file of the PShell software that is used to communicate with the electron analyzer. At this step, the beamline shift corresponding to the monochromator offset is corrected on the photon energy value. Here we use 1.6eV, which is a typical offset of our monochromator, based on the water gas phase 2b2 observation. In addition, the Auger kinetic energy range, in the present case [425 480] is used as the range to integrate the signal. This range ensures that no XPS is traveling through.

- Average - After importing, the repetitions that are overlapping within a tolerance of 10%/hour are selected, and averaged. This ensures that only spectra are averaged, during which the ice is stable during acquisition. Ice growing towards or retracting away from the sampling aperture would lead to loss of signal intensity.

- I0 – the spectra are normalized to the photon flux. The photon flux is measured with a photodiode (AXUV100GDS from ITW Opto Diode) at the location of the sample, usually measured in vacuum at the end of each beamtime. The photon flux measurement allows taking into account any absorption feature such as oxygen contaminations in the beamline optics, which might change from beamtime to beamtime. This specific beamline has the particularity to contain a high fraction of second order light (45

- Normalization – this step allows scaling the spectra before the gas phase subtraction.

- Water gas phase removal – this step allows removing the gas phase contribution in the PEY-XAS spectra. Indeed, the electrons are sampled from the surface of ice, but also the from the gas phase within the volume, which is intersected by the X-ray beam and which is within the acceptance volume of the analyzer. The contribution of gas phase water is removed in a way that the points between 534 and 534.4 eV are aligned with the linear pre-edge background. This is based on the assumption that oxygen in carbon-oxygen bonds does not contribute in this range and also that it is below the rise of pre-edge of the O K - edge. Nevertheless, we can see on the figure 2 that the region around 537 eV shows spiky variations – probably too much gas phase has been removed.

- Background - the background is removed as a linear fit to the region 517-530eV. Because this background range is quite short and there is a little flexibility in the slope of such fit, we allow ourselves to vary the slope of the fit such that the resulting main edge ([537.6-541.6]) to tail ([556.6-561.6]) ratio tends to 2 (as seen in [2]). One can justified this by the fact that different measurements have different background due to different alignments. Indeed, because ice quickly reacts to temperature and pressure change, it is difficult in our setup to position the ice at a distance with better than 0.1 mm accuracy. Another justification is that the background intensity consists mostly of secondary electron emitted from second-(or higher-) order light (which varies as a function of photon energy), and we know that the latter increases in proportion with respect to the first order when the water gas phase pressure increases. A larger background means a smaller main to tail ratio. With such treatment of the background, the final spectra should cross at the isosbestic point (539.6eV) and the tails should merge at 560 due to normalization [2].
- Normalization – the spectra is finally normalized to the tail [556.6-561.6eV] however, normalizing to the main edge ([537.6-541.6]) would give the same result because of the manipulation in step 6).
- Smoothing – the spectra on fig 2 has been smooth using the matlab smooth function with 5 points or 1 eV.

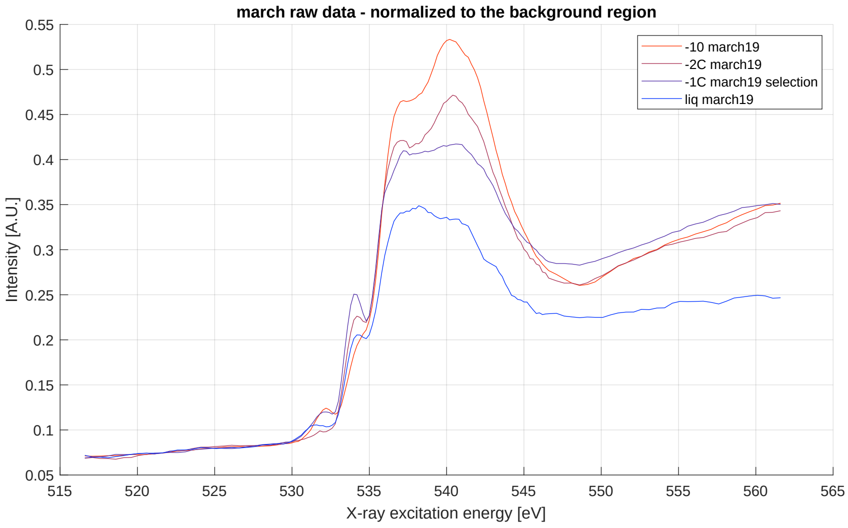

FIGURE 3.8: PEY-XAS data from Figure 3.2, normalized to the background region.

3.2.2 *2nd order light*

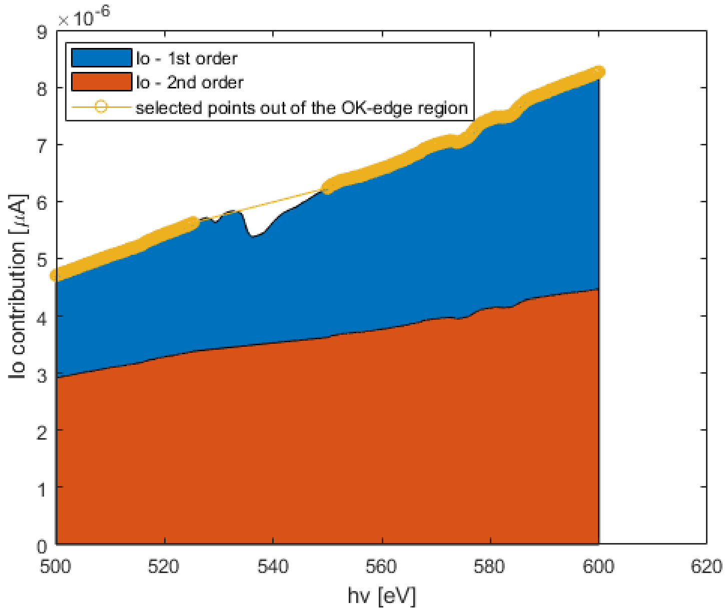

FIGURE 3.9: First and second order contribution to the photocurrent measurement, based on the second order light experiment (see Section 2.1). The red area is calculated as a fraction of the yellow line, which is the total flux without the oxygen absorption edge (the second-order light doesn't have an oxygen absorption edge at 1070 eV)

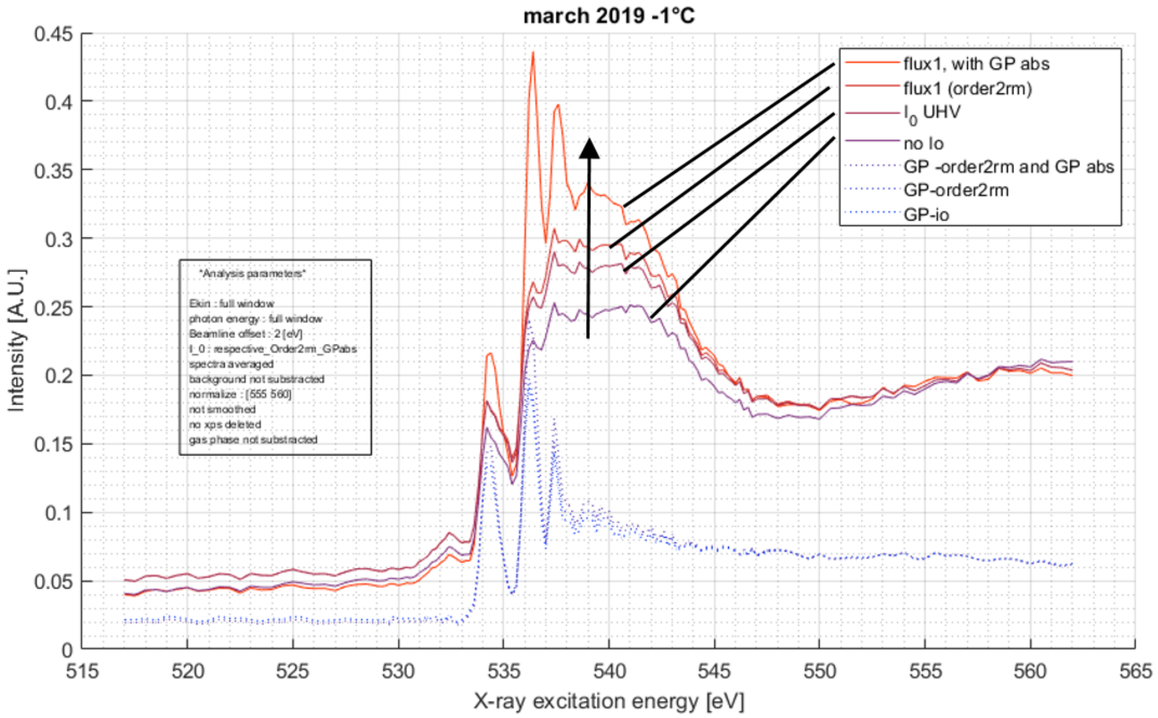

FIGURE 3.10: Photon flux normalization: impact on XAS spectra of ice at -1°C (high vapor pressure). From purple to red: no photon flux normalization, normalized to the photon flux directly from the photocurrent measurement, normalized to the photon flux corrected for the 2^{nd} order light, normalized to the photon flux corrected for the 2^{nd} order light and for the gas phase absorption.

3.2.3 *Gaussian deconvolution*

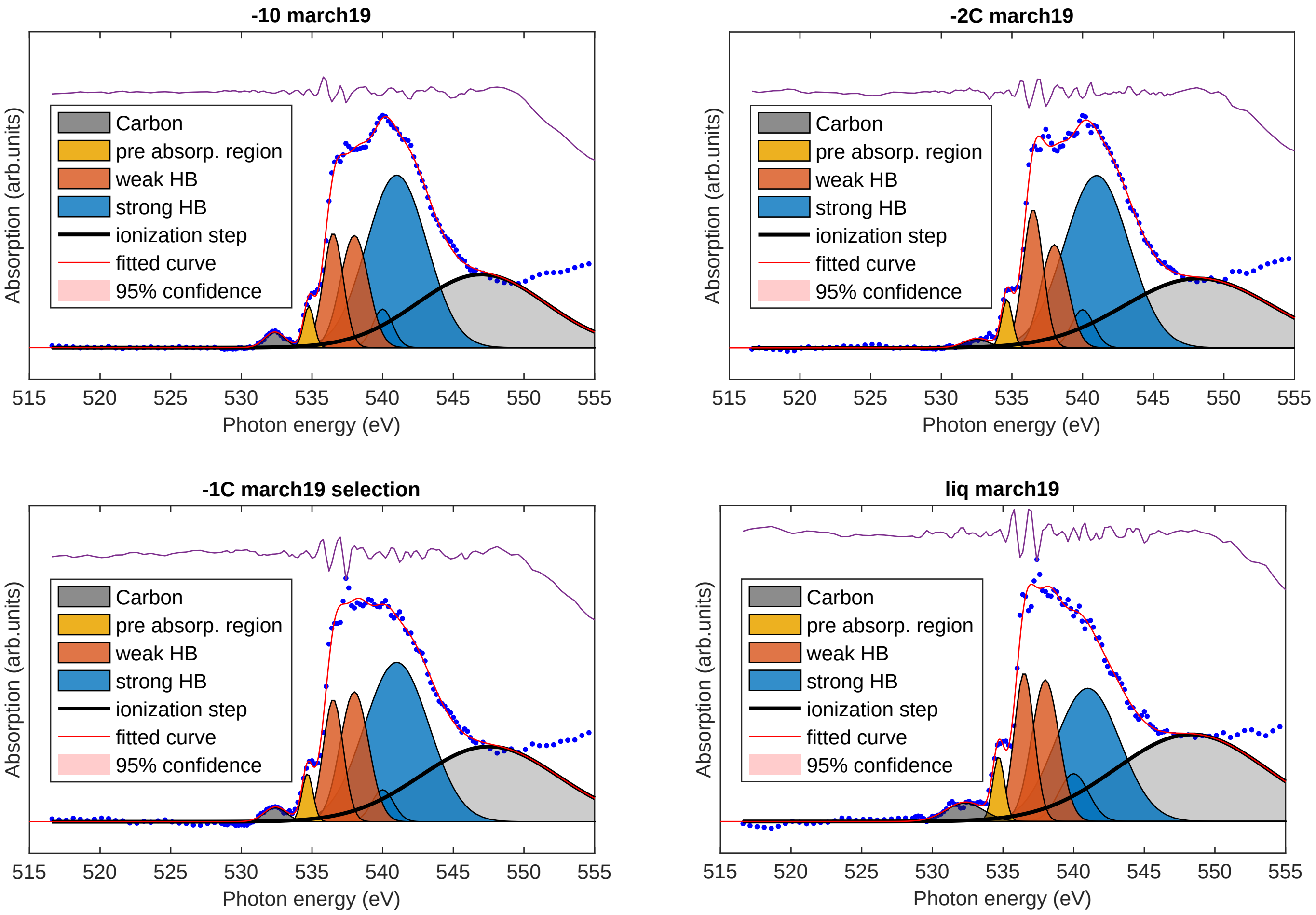

FIGURE 3.11: Deconvolution of the PEY-XAS spectra from Figure 3.2

TABLE 3.1: Fitting parameters to represent O K-edge spectra by 7 Gaussian components. The fit uses the least squares method in the range 515 eV to 545 eV.

Peak nº	1	2	3	4	5	6	7
Designation	C=O	Pre-edge	Main edge	Main edge	Post-edge	Post-edge	Back-ground
Position range [eV]	532.0-532.5	534 - 535	536.5	538	540	541	545
$\frac{\textbf{FWHM}^{a}\,[\textbf{eV}]}{\textbf{1.665}}$	1-2	0.4-1	1-10	1-10	1-10	1-10	1-10

---

[a] FWHM= 1.665*c where c is the width in the Gaussian form a*exp(-((x-b)/c)^2)

3.2.4 *MC simulation*

3.2.4.1 *IMFP*

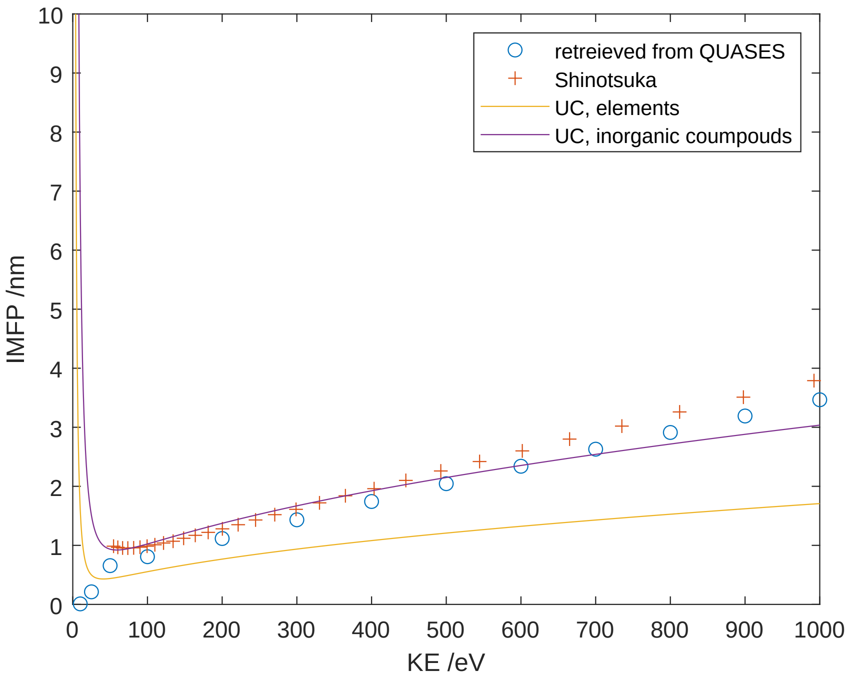

FIGURE 3.12: Comparison of IMFP formulas of water (liquid). Blue circles show the IMFP as calculated with the TPP-2M formula in the QUASES software. The Blue circles and Shinotsuka data [3] are well approximated by the universal curve for inorganic compounds (formula: UC$_{ic}$= (641/KE^2)+0.096$\sqrt{KE}$ taken from [4])

3.2.4.2 *Gas phase density calculation*

From $PV = nK_BT$:

$$\rho_{gas}^{1mbar} = \frac{nM}{V} = \frac{PM}{K_BT} = \frac{100\,Pa \cdot 0.018\,\mathrm{kg\,mol^{-1}}}{1.38 \times 10^{-23}\,\mathrm{J\,K^{-1}} \cdot 253\,\mathrm{K} \cdot 6.022 \times 10^{23}\,\mathrm{mol^{-1}}} = 8.56 \times 10^{-4}\,\mathrm{kg\,m^{-3}} \tag{3.8}$$

3.2.4.3 *Comparison simulation with Bluhm 2010*

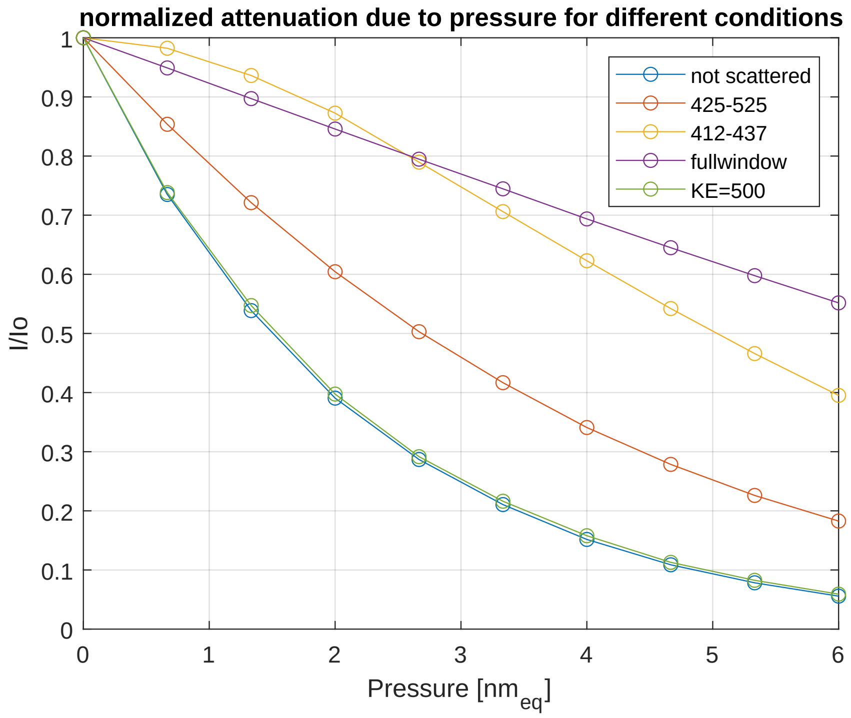

FIGURE 3.13: Normalized attenuation of the electron intensity reaching the electron analyzer as a function of gas phase pressure. Simulated with the Monte Carlo algorithm. The pressure units on the y-axis are in nm_{eq}, meaning that 1 mbar of gas phase is represented in the simulation by 1 nm of ice, see Equation 3.3.

3.2.4.4 *Comparison experiment / simulation*

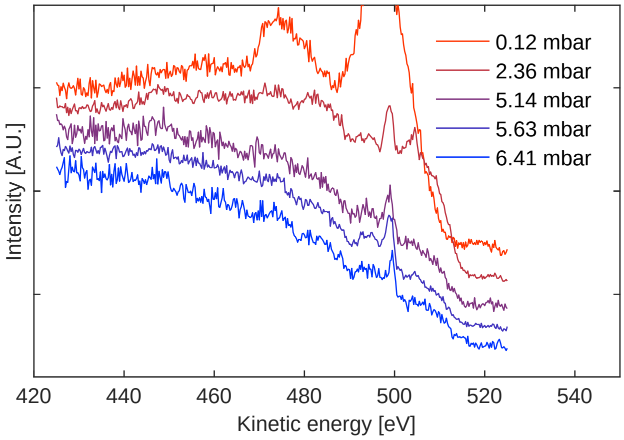

(a) Experimental O KLL Auger spectra of ice at different temperatures (pressure). Increasing temperature is color-coded from red to blue. Integrated over the whole PEY-XAS photon energy range (515-560 eV). The data are the same as in Figure 3.2 with the additional spectra of ice at -40°C (0.12 mbar).

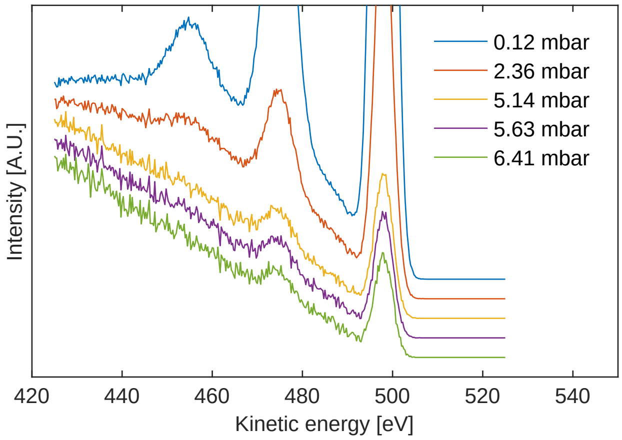

(b) O KLL Auger spectra obtained from the Monte-Carlo simulation at pressures corresponding to Figure 3.14a.

FIGURE 3.14: Experimental and simulated O KLL Auger spectra. Normalized at KE=425 eV and offset for clarity.

References

1. Gabathuler, J. P., Yang, H., Manoharan, Y., Boucly, A., Alpert, P. A., Artiglia, L., Bartels-Rausch, T. & Ammann, M. "The premelting of ice revisited with X-ray absorption spectroscopy" (in preparation).
2. Niskanen, J., Fondell, M., Sahle, C. J., Eckert, S., Jay, R. M., Gilmore, K., Pietzsch, A., Dantz, M., Lu, X., McNally, D. E., Schmitt, T., Vaz da Cruz, V., Kimberg, V., Gel'mukhanov, F. & Föhlisch, A. "Compatibility of quantitative X-ray spectroscopy with continuous distribution models of water at ambient conditions". *Proceedings of the National Academy of Sciences* **116**, 4058–4063 (2019).
3. Shinotsuka, H., Da, B., Tanuma, S., Yoshikawa, H., Powell, C. J. & Penn, D. R. "Calculations of electron inelastic mean free paths. XI. Data for liquid water for energies from 50eV to 30keV". *Surface and Interface Analysis* **49**, 238–252 (2017).
4. Seah, M. & Dench, W. "Surf. Interface Anal" (1979).

4

ADSORPTION OF HEXYLAMINE ON ICE, AS SEEN BY NEAR AMBIENT PRESSURE XPS

This chapter is adopted from the manuscript in preparation, which will be published as: Gabathuler, J. P., Manoharan, Y., Artiglia, L. & Ammann, M. "Adsorption of Hexylamine on ice, as seen by near ambient pressure XPS" (in preparation)

4.1 Adsorption of Hexylamine on ice, as seen by near ambient pressure XPS

The adsorption of trace gases on ice is important for atmospheric chemistry and there is a growing interest concerning the role of the Quasi-Liquid Layer (QLL) in the air-ice interaction. While the behavior of acids on ice has been intensively investigated, we currently lack knowledge about the adsorption of bases. Hexylamine (HA) is a simple aliphatic amine that we use to represent atmospheric bases and to study their interaction with ice. Here we present x-ray photoelectron spectroscopy (XPS) and Near Edge X-ray Absorption Fine Structure (NEXAFS) spectroscopy data to characterize the interaction of HA with the surface ice. XPS data reveal that the HA coverage already reaches monolayer saturation at a HA partial pressure of $2 \cdot 10^{-5}$ mbar. NEXAFS data reveal that the presence of HA on the ice reduces the fraction of water molecules in tetrahedral coordination, possibly due to water engaged in hydrating hexylamine and hexylammonium molecules.

4.1.1 *Introduction*

As snow on the ground or cirrus clouds in the upper troposphere, ice plays a major role in the radiative budget of the Earth because of its high albedo [1]. In addition, ice provides a large surface area for trace gas – ice interactions, which influence the chemistry of the atmosphere [2–6]. A key aspect of the ice/air system is the characteristic of ice to form a Quasi-Liquid Layer (QLL) on its surface at temperatures close to the melting point [2]. This QLL arises from the broken symmetry at the interface and is theoretically explained from surface tension thermodynamics [2]. It has been established that the QLL increases in thickness from the onset temperature, T_{onset} until the melting point, T_M or in the presence of solutes [7–10]. A decade-long debate is ongoing as to whether the QLL could represent a layer with properties similar to a bulk aqueous phase, for instance with respect to solubility of gases, acidity, or the kinetics of reactions. For example, strong acids like HCl also exist in the molecular form at the ice surface (unexpected for a bulk aqueous solution, where they are largely dissociated) and enter into the ice as dissociated ions surrounded by hydration shells, while still leaving crystalline ice in between, indicating a different picture than simple thickening of the QLL that has often been suggested before [11].

The adsorption of acidic species on ice has received considerable attention, namely, with regards to acid dissociation, QLL enhancement or the formation of solvation shells penetrating deeper in the ice [3, 5, 7, 9, 11–23]. In turn, almost no research article reports on the adsorption of bases such as amines on the surface of the ice. The only notable exception is ammonia, which has been shown to saturate the dangling OH group on the ice surface at 100 K (-173.15 °C) and to increase the overall tetrahedral coordination [24, 25]. This work aims at extending the dataset of the interaction of trace species on ice, by investigating hexylamine, a strong base representative of the amine family, at environmental temperatures. Amines are emitted from natural sources such as the ocean, wildfires, and anthropogenic sources for example livestock farming or rocket fuel burning [26]. Ambient concentrations of aliphatic amines in the continental boundary layer have been reported to be <0.025-0.35 ppb, compared to $\sim$25 ppb for ammonia [27]. In the plume downwind of a massive bovine source in California, total amine mass (i.e. the mass of all $R{-}NH_2$ molecules, where $R \neq H$) accounted for 14-23% of that of ammonia [28]. Aliphatic gaseous amines are strong bases and similarly to ammonia they may react with atmospheric acids to form alkyl ammonium salts in the particle phase. Amines in the gas phase may undergo oxidation reactions, mostly with OH radical, with a typical lifetime in the order of hours, contributing to secondary organic aerosol formation. Photolysis or further OH attack may lead to the formation of toxic HCN and of N_2O, which is a greenhouse gas and an ozone-depleting substance (ODS) in the stratosphere [29]. In the condensed phase, amines and the conjugated ammonium ions are rather inert [26], even though ammonium is involved in aqueous phase secondary chemistry leading to the formation of nitrogen containing organic products [30, 31].

Looking into the adsorption of an amine allows us to broaden our understanding of the response of the ice surface to bases and to contribute to the question of interfacial acidity. In aqueous solution, aliphatic amines are surface active due to the hydrophobic tail, with only the amine or ammonium head-group being hydrated, leading to lowering of the surface tension [32]. Choosing the surface active hexylamine (HA), a medium tail-size aliphatic amine as an example, thus allows us to investigate the effect of the presence of the amine just at the interface, without significant burial into the top ice layers, as it could possibly be the case with ammonia.

In this work, we make use of X-ray photoelectron spectroscopy (XPS) to characterize the surface of ice when exposed to different HA partial pressures. The X-rays, with incoming photon energy E_{ph}=hv [eV], excite electrons from core levels of atoms contained in the sample. Via the photoelectric effect, electrons are ejected from the atom with a kinetic energy KE=hv-BE, where BE is the binding energy related to a specific electronic level of the host atom. Because these electronic levels of each atom have specific BE values, XPS can identify the elemental composition, but also the oxidation state and the chemical environment. Due to the very short Inelastic Mean Free Path (IMFP) of electrons in condensed matter (typically 1-2 nm), XPS is remarkably surface sensitive [33].

X-ray absorption spectroscopy (XAS) has become an established tool to measure the coordination of molecules in the water system [8, 10], especially since the development of near ambient pressure photoelectron spectroscopy systems [34]. Near-edge X-ray absorption fine structure (NEXAFS) spectroscopy, generally probes the energy levels of the lowest unoccupied molecular orbitals by resonant excitation of core electrons with X-rays into these orbitals (below the ionization energy). The core vacancy resulting from the excitation is filled with an electron from a valence level. The energy difference is released either in the form of a photon (fluorescence) or transferred to another electron in one of the filled valence orbitals, which is then ejected from the atom/molecule and referred to as Auger electron. Since especially the outermost, unoccupied molecular orbitals are involved in forming hydrogen bonds, the changes in energy and intensity of these resonant transitions measured with XAS lead to fine structure at the absorption edge (and hence the term NEXAFS). In their pioneering work, Bluhm et al. used electron yield XAS (PEY-XAS, that is XAS via partial electron yield measurement) to study the premelting of ice as a function of temperature for the first time [8]. They are sensitive to the closest neighbors and for the O K-edge of water therefore reflect the very local structure of water. The probing depth of XAS in electron yield mode (PEY-XAS) is also related to the IMFP of the Auger electrons in matter, approximately 2 nm for O-KLL Auger electrons, and provides surface sensitivity to the technique. EY-XAS has been routinely used in recent studies [11, 16, 35–38] to measure how adsorbed species can perturb the hydrogen bonding structure near the surface of ice.

On the one hand, XPS provides us with chemically selective surface composition information. This includes the degree of protonation of acids or bases, specifically also for amines via resolving $R{-}NH_2$ and $R{-}NH_3^+$ from a deconvolution of the N 1s peak (Figure 1) [39]. XPS also allows quantifying surface concentration and an estimate of their density profile with depth [18, 38]. On the other hand, PEY-XAS spectroscopy allows quantifying the coordination in the hydrogen-bonding network. This provides direct insights into the perturbation that hexylamine produces to the ice surface region and completes the characterization of the physical and chemical environment.

4.1.2 *Methods*

We have conducted the experiments on ice using the In Situ Spectroscopy (ISS) beamline X07DB of the Swiss Light Source (SLS) at the Paul Scherrer Institute (PSI) in Switzerland. The Near Ambient Pressure Photoelectron spectroscopy (NAPP) endstation [37, 39] consists of a differentially pumped electron analyzer (ScientaOmicron R4000-HiPP-2) connected to a high-pressure chamber via a 0.5 mm-wide aperture cone. The chamber system used in the present work for the experiments with ice features a small volume and a flexible gas dosing system [37]. On the beamline side, a 100 nm-thick silicon nitride window connects the experimental cell to the beamline. This setup allows photoelectron spectroscopy at high pressure (up to 10 mbar), sufficient to study ice samples over a large temperature range from −100 °C to 0 °C, in equilibrium with their respective vapor pressure. The ice is grown from water vapor deposition on a sample holder, which is cooled with a variable N_2 gas flow impinging on its back. The N_2 flow itself is cooled in liquid N_2. Several gas lines allow dosing different species to the sample chamber; typically, we have a line of water to grow ice and keep it stable, a gas line to dose common gases (O_2, N_2, Ar, He, CO_2) and another line to dose trace amounts of a gas of interest, eventually from a solid or liquid source using a carrier gas. Different to the original description of the chamber [37] a 6 mm outer-diameter PFA tube has been added in the gas dosing inlet from the leak valve until just above the sample. This allows efficient transport of a sticky gas to the sample holder and decreases retention at the walls. In addition, a new design on the head of the cryo-holder ensures that the coldest spot is precisely located on a well-defined location on the sample holder. This provides reproducibility to the location where the ice nucleates and ensures that it equilibrates exactly at the measurement spot.

4.1.2.1 *Dosing of gases*

As mentioned previously, ice is grown in situ from water vapor. The water vapor is dosed from a water reservoir to the chamber via a leak valve. A capacitance manometer (MKS baratron 626A) is used to measure the pressure in the chamber with a 0.25% precision and a detection limit of 5×10^{-3} mbar [38]. At the beginning of the experiment, approximately 15 ml of liquid water (TraceSelect Ultra; Fluka) is poured into the water reservoir and is freeze-pump-thawed three times to remove any dissolved gases (mostly CO_2). First, the desired water vapor pressure (corresponding to the vapor pressure of ice at the intended temperature of the experiment) is adjusted with the leak-valve and stabilized in the chamber. Note that during experiments, the only pumping acting on the chamber is through the electron sampling aperture towards the analyzer. Next, the sample holder is retracted by 1 mm (to give room for the ice to grow) and the temperature is lowered to -80 °C to nucleate ice. At this temperature, almost all of the water coming from the dosing line deposit and contributes to the growth of ice. Once the desired ice thickness is obtained, the temperature is slowly increased towards the target temperature (here, -20 °C) during at least 30 minutes to allow the ice to recrystallize. A slight supersaturation $\sim$1% is maintained during the measurement to ensure that the ice is not evaporating by compensating for the slightly lower local pressure in front of the aperture. If the ice is growing, it will grow mostly in the regions away from the measurement spot because the pressure drop in front of the cone reduces the vapor pressure, but at the measurement position, the distance between the ice and the cone remains constant [34]. Hexylamine was dosed using the dosing system depicted in Figure 4.6. The content of the bubbler is specified in the column 'dosing' in Table 4.6. In the case of the HA aqueous solution, the vapor pressure of HA is given by the Henry's law constant ([40] however, there is a large variation reported in the literature, see [41]): at a concentration of 32 mM, we have 1 mbar in the gas phase at equilibrium. In addition, roughly 20 mbar of water are in the gas phase (because it is an aqueous solution, T = 20 °C). Argon at ambient pressure ($\sim$1000 mbar) flows through the bubbler and equilibrates with the solution. After the bubbler, we assume that the gas exchange is perfect and that argon carries 1 mbar of hexylamine or a mixing ratio of 10^{-3}, together with 20 mbar of water vapor ($\sim$2%). After that, further dilution (1-100x) at the exit of the bubbler is possible to adjust the mixing ratio of hexylamine in the dosing line to the desired value. To our knowledge, freezing-point depression data for aqueous hexylamine solutions don't exist and we have to assume that our experimental conditions are within the ice stability domain. All tubing is made of PFA to minimize the physisorption/chemisorption of hexylamine along the tubing and facilitate its admission to the chamber. Opening the leakvalve from this line such that the argon pressure in the chamber is 1 mbar allows reaching 10^{-3} to 10^{-5} mbar of HA in the chamber. The version based on HA solution (data ref. 2) was later abandoned because the depletion of HA in the bubbler was too fast compared to the duration of acquisition. With pure HA (data ref. 3-4-5), we avoid the additional 2% water in the carrier gas but we had what we think is condensation of HA in the leak valve, causing trouble for the chamber pressure stability. The vapor pressure of HA is 8.9 mbar at 20 °C, 10.0 mbar at 22 °C, and 12.08 at 25 °C [42]. The room temperature was 25 °C and we will make the assumption that the HA liquid is at 22 °C due to evaporative cooling. In the May 2022 beamtime (data ref. 7), we used an ice bath to lower the VP of HA compared to room temperature and avoid condensation in the dosing line. The vapor pressure of HA is 2.3 mbar at 0 °C [42]. In order to grow ice, and later to keep it stable, dosing water must be very precise. Because the water reservoir is at 23.15 mbar (vapor pressure of pure water kept at 20 °C), dosing water is more sensitive to the chamber pressure than dosing the HA-containing argon, whose base pressure is atmospheric pressure. For this reason, we start by dosing 1 mbar of argon from the hexylamine dosing system (with the bubbler bypassed, thus pure Ar), and then add 1 mbar of water (i.e., the water vapor pressure at the target temperature of -20 °C). We use a residual gas analyzer mass spectrometer (RGA 100, Stanford research) to monitor the evolution of the gas phase partial pressures of argon, water and eventual traces of N_2 and CO_2. The hexylamine should appear at m/z=30 according to [43] but at the low partial pressures used here, it remains below the detection limit of the RGA.

4.1.2.2 *Data acquisition and analysis*

Before the ice is prepared in situ, we characterize the sample holder surface with XPS survey spectra to ensure that the carbon contamination is low enough and that no other contaminations are present. As a rule of thumb, we consider that the gold coating is sufficiently clean when the C 1s peak amplitude is below 1/10th of that of the larger of the two Au 4f peaks. For survey scans, the pass energy is 50 eV, the photon energy is 1000 eV, the kinetic energy is swept from 255 eV to 1000 eV with a step of 0.25 eV, integration time at each step (dwell time) is 0.12 seconds. During the experiments, we scan O 1s, N 1s, and C 1s regions with respective region iterations of 1, 5, and 3, respectively, to give more acquisition time to the N 1s region, which exhibits the lowest signal-to-noise ratio. For these high-resolution core level spectra, the pass energy is 20 eV, the photon energy is 700 eV, the kinetic energy is swept in a 20 eV-wide window centered on the peak of interest with a step of 0.1 eV, and the dwell time is 0.2 seconds. We use the O 1s signal intensity to monitor the ice stability. We consider the ice stable, when the ice O 1s signal variation is less than 10% over a period of one hour. The signal intensity allows to monitor the distance between the electron-sampling aperture and the ice surface. Decreasing signal intensity is observed when the ice grows or retreats, as the ice surface would get out of the focus of the electron optics. The background in the N 1s and C 1s regions on clean ice are very important measurements because they provide the reference background to compare the data of HA on ice. Once the clean ice is stable, we start to measure the XPS regions, to get the clean ice reference. Due to the high gas phase pressure (about 2 mbar), the extent of charging of the surface of ice is remaining small, and the apparent binding energy of the aliphatic C 1s reaches a maximum of about ∼3.1 eV above the reference value of 285.0 eV [44]. After correcting for charging using the aliphatic C 1s deconvoluted from the C 1s spectra during HA dosing (there was no C 1s signal on clean ice, not even a pinch of adventitious carbon, see Figure 4.1), the condensed phase O 1s appears 532.5 eV for Feb. 2022 data (data ref. 1 to 5), and 533.0 eV in the May 2022 (data ref. 6 and 7) and also in the LJ data. More on this small variation in the discussion. This apparent binding energy value for the condensed phase O 1s was used to correct for charging in the scans where the C 1s signal is too weak.

The XPS spectra are averaged over a few hours to increase the signal-to-noise ratio (SNR). Since there is no Shirley background function in Matlab, we subtract a second-order polynomial fit of the background, as seen in Figure 4.7. Although a Shirley subtraction would be a better approach to treat XPS backgrounds, a second-order polynomial fit provides a better evaluation than a simple linear fit, especially for XPS peaks with high-intensity backgrounds in the low KE region, as is the case for O 1s measured at 165 eV. In the present work, this approach is sufficient for the purpose of comparing peak areas. After subtracting the background and correcting for the beamline offset, we perform a Gaussian deconvolution with the parameters displayed in Table 4.3.

Oxygen 1s: It is important to fit this peak with enough freedom because the gas phase component shifts differently than the condensed phase due to charging. Their relative BE difference then varies as seen in Figure 4.9.

Carbon 1s: The carbon reference BE data are taken from [44]. Here we first fit the main feature (C-C) and then use the C-C amplitude value to constrain the amplitude of the C-N peak to 1/5th of that of C-C, corresponding to the case where we have pure hexylamine. In addition, the carbon deconvolution uses 2 additional features to describe adventitious carbon. We allow a little more flexibility on the FWHM and position to fit the adventitious carbon (ice in absence of HA).

Nitrogen 1s: N 1s positions are constrained from a liquid jet XPS experiment (see Figure 4.8) and from Brown et al. [39]. In particular, the binding energy difference between $\mathrm{R{-}NH_2}$ and $\mathrm{R{-}NH_3^+}$, $\Delta_B E = 2.3\,eV$ is an important constraint for the deconvolution. On ice, the N 1s peak deconvolution is not satisfying with the 2 peaks identified in the liquid jet data, therefore we add a feature with binding energy BE=400.0 eV and leave it free to move by 0.5 eV (see discussion for its assignment). For the width, we cannot simply apply the width found in the LJ XPS data, because the energy resolution of the ISS beamline used for the experiment with ice is smaller than that of the SIM beamline used for the liquid jet XPS experiments. However, we noticed in the LJ that the width of the N 1s peak is in between those of O 1s and C 1s. Here, we set it to 0.9 to obtain consistent fit quality.

4.1.2.3 *NEXAFS*

We acquire the XAS spectra in the range from 515 to 560 eV. In order to avoid the traveling photoemission peaks due to excitation of Argon, we choose to acquire in fixed mode at a kinetic energy KE = 450 eV (window width of 5 eV at PE = 50 eV). There should be no photoemission peaks traveling in this KE window. According to Table 4.1, Ar 3p, Ar 3s are above the window, Ar 2p, Ar 2s are below.

Spectra are averages of several spectra. First, the spectra are normalized to the photocurrent. Then the beamline offset is subtracted from the photon energy axis. A series of processing steps are necessary in order to interpret the NEXAFS data. Briefly (more details are available in Section 4.3.2.3), the averaged spectrum is normalized to the photon flux. At this point, we remove the gas phase contribution. Finally, the background is subtracted and the spectrum is normalized. From the processed data, we extract information about the hydrogen-bonding network by deconvoluting the spectra with 7 Gaussians. This approach was developed by Huanyu Yang [45] and is based on other similar approaches [46, 47]. The 1st peak is associated with oxygen of oxygenated carbon contaminations, the 2nd peak represents the pre-edge feature. The 3rd and 4th peaks are fitting the main edge; the 5th and 6th peaks are fitting the post edge, the last peak is to account for the ionization edge, represented by the first half of the Gaussian. Deconvolution constraints are given in Table 4.4. The pre-edge area is the area of the second Gaussian. The main-to post-edge ratio is calculated from the ratio of the area of the 3^{rd} and 4^{th} to that of the 5^{th} and 6^{th} Gaussians.

4.1.3 *Results and discussion*

Figure 4.1 shows photoelectron spectra of the N 1s and C 1s regions of 3 series, corresponding to before, during, and after dosing 2×10^{-5} mbar of HA on the surface of ice. The spectra on the top show the deconvolution of the spectrum during dosing. O 1s data is shown in the supporting Figure 4.9. The data in Figure 4.1 represent a direct *in situ* observation of reversible adsorption of HA on ice.

The poorer signal-to-noise ratio for N 1s compared to C 1s is due to the 6 times lower concentration of N atoms, to the N 1s peak appearing on top of a substantial background resulting from the O-KLL Auger emission, and to the assumption that the N-head is pointing towards the ice and therefore is buried below a carbon layer, which attenuates the photoelectrons from the N atoms.

We use the liquid jet XPS (setup as in [48]) N 1s spectrum of a 0.1 M aqueous HA solution at pH equal to the pKa of HA (see supporting Figure 4.8) as a reference for the deconvolution of the N 1s spectra on ice. On ice, the N 1s is composed of a third component that we tentatively attribute to adsorbed neutral amine, $R{-}NH_2^{ads}$, as indicated in Figure 1. The adsorbed amine $R{-}NH_2^{ads}$, has a slightly higher binding energy than the solvated amine $R{-}NH_2$ for the same reason that gas phase water has a higher binding energy than the condensed phase water (screening of the charge created by the core hole in the condensed phase, see below). We don't expect another amine-derived nitrogen species at this BE. We have also moved spots from time to time and could not find evidence that this peak could result from beam damage effects. We

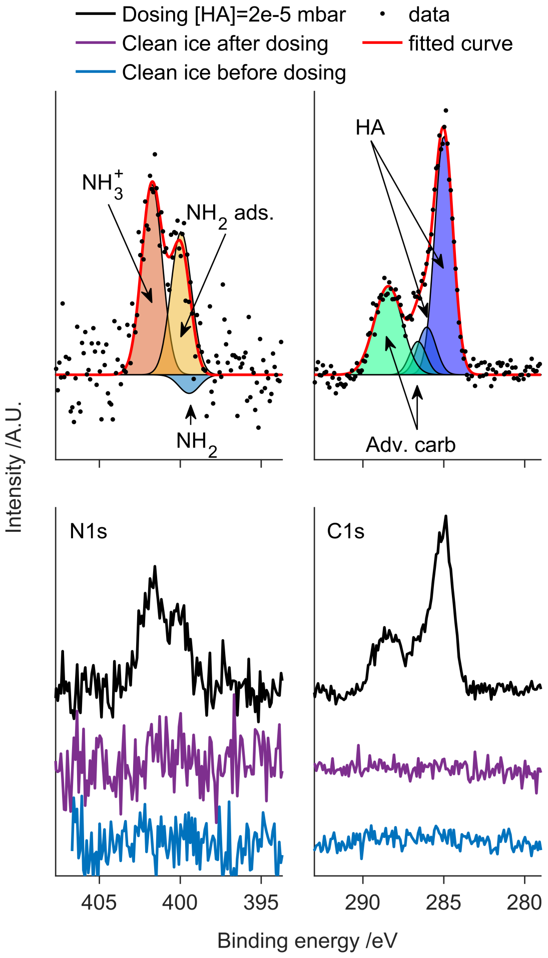

FIGURE 4.1: N 1s and C 1s spectra probing the interfacial region of ice at −20 °C (data set ref. 7). Data were acquired with 700 eV photon energy and pass energy 20 eV. The spectra on the bottom correspond to before, during, and after dosing 2×10^{-5} mbar of HA on the surface of ice. The spectra on the top show the deconvolution of the spectra during dosing (black dots are data from the black line), together with the deconvolution Gaussians and their sum (red line).

also note that after closing the leak-valve, and thus after desorbing, no N-containing species remained on the surface. The feature corresponding to the hydrated $R{-}NH_2$ is negative in this example and very small. We observe here that the peak area of the component assigned to $R{-}NH_3^+$ is slightly larger than that of $R{-}NH_2$ adsorbed meaning that the proton availability is sufficient for more than half of the adsorbed hexylamine molecules to be protonated at such surface coverage.

The C 1s spectrum is deconvoluted with 4 Gaussians as indicated with the arrows. The components from HA are deconvoluted with C-C and C-N, while the contributions from adventitious carbon are fitted with C-O and C=O as indicated in the supporting Table 4.3. The ice surface is very clean before and especially after dosing, as seen from the C 1s spectrum. This shows that the adsorption is reversible and that the concentrations are not too high such that it would leave behind non-volatile contamination traces after dosing. The observation of reversible adsorption is consistent with the behavior of other volatile organic compounds, such as acetone, alcohols or carboxylic acids [49].

The O 1s spectra shown in the supporting Figure 4.9, exhibit two components, one related to gas phase water between the sample and the electron sampling aperture and the other attributed to condensed phase water in ice. The substantial width of the condensed O 1s component results from the range of different configurations water molecules experience [50]. The binding energy difference between the condensed phase and the gas phase peak is due to the screening of the charge created by the corehole in the condensed phase [50]. Two features are apparent when considering the averaged spectra in the supporting Figure 4.9. First, the condensed phase O 1s component is lower in presence of HA, which is due to the attenuation of the photoelectrons by the layer of adsorbed HA on the ice surface (see attenuation model below). Second, the binding energy difference between the condensed phase and the gas phase components is larger in presence of HA. Several aspects make it difficult to quantitatively understand this. The pure ice is insulating, and thus the ice is charging due to photoemission, though by only a few eV due to the neutralizing effect by ions generated in the gas phase. Since the gas phase water molecules do not experience the same potential as the ice surface because they are closer to the grounded electron sampling aperture, the gas phase peak is shifting less than the condensed phase peak, which was set to 533.0 eV (literature value) to correct for the charging. Upon adsorption of HA, however, the sample gets more conductive (due to the ammonium ions). This leads to reduced charging, and thus a larger apparent BE difference to the gas phase peak. Adsorption of HA may also lead to a change in the work function at the ice surface. With an ideally conducting sample, the measured BE is only sensitive to the spectrometer work function, while within the insulating sample, it also depends on the sample work function [51–54]. Therefore the apparent differences in BE between condensed phase and gas phase peaks are difficult to understand in detail. Some widening of the ice-related peak (see supporting Figure 4.9) indicates either effect of differential charging or small variations over time during the acquisition of the series of spectra used for averaging.

The upper plot of Figure 4.2 shows the time evolution of the different XPS peaks from Figure 4.1. The area from deconvolution is normalized to the total cross-section of the respective element at hv=700 eV. These normalized intensities are then ratioed to that of O 1s of ice, measured at the same photon energy, which cancels the influence of the photon flux and of slight changes in the sample – aperture distance. However, the ratios do not directly reflect elemental ratios, as the three elements are measured with different probe depths (same photon energy, but different kinetic energy). The total hexylamine carbon, labeled "HA carbon" in Figure 4.2 represents the two peaks assigned to HA: C-C and C-N (assuming that adventitious carbon doesn't contribute to these peaks). The total hexylamine nitrogen, labeled "HA nitrogen", is the sum of the different nitrogen features i.e. $R{-}NH_2$, $R{-}NH_3^+$, and $R{-}NH_2^{ads}$. The C/O and N/O y-axis are scaled with a factor 6:1 to represent the atomic ratio of HA, keeping in mind that the signal ratio is not exactly the atomic ratio. We notice that the observed C/N ratio is indeed around 6. Adv. Carbon and $R{-}NH_2$ are not shown in this graph to improve readability. We dose 1×10^{-5} mbar for 2 hours and then 2×10^{-5} mbar for 4 hours. The lines trace again the increase of all signals from a clean background upon dosing HA and their decrease to a clean background after dosing. The C 1s and N 1s

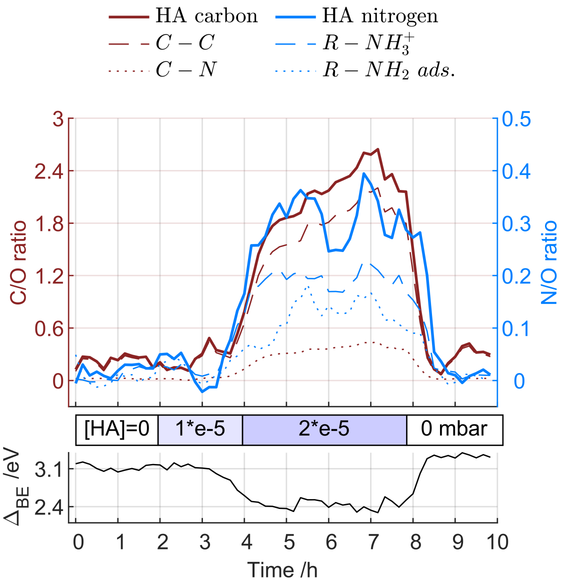

FIGURE 4.2: Time evolution of data set 7 (experiment from Figure 4.1 i.e. 2×10^{-5} mbar of HA on ice at $-20\,°C$). The time step is 10 minutes. The main panel shows C/O in brown with individual contributions from C-C and C-N. HA carbon is the sum of these 2 contributions. The N/O ratios are shown in blue with individual contributions from protonated and adsorbed HA. HA nitrogen is the sum of protonated, adsorbed and unprotonated HA. Unprotonated HA ($R{-}NH_2$) is not shown in Figure 4.2 because the signal is very noisy and doesn't significantly contribute to the total HA nitrogen. For the sake of legibility, C 1s and N 1s smoothed with 3 and 5 points, respectively. The bottom panel displays Δ_{BE}, the difference between the observed BE fitted from the ice O 1s raw data and the reference BE of 533.0 eV. The horizontal bar in the middle of the 2 panels shows the HA concentration dosed in the gas phase.

start to rise 1.5-2 hours after the start of dosing, slightly before the increase of dosing from 1 to 2×10^{-5} mbar. Most probably 2 hours is the time required to passivate the walls and establish the set partial pressure in the vicinity of the ice sample. Local adsorption equilibration occurs at a much faster time scale than this passivation of all surfaces. The first shoulder in the C/O ratio of 1.8 is due to the lower partial pressure of 1×10^{-5} mbar and the second C/O increase to 2.4 is due to the higher partial pressure of 2×10^{-5} mbar. We note that the decrease of signal upon stopping dosing is faster than the increase; obviously, the time scale for the passivation of lines before that 3-way valve bypassing the HA bubbler (see supporting Figure 4.6) is more important than the time scale of desorption from the surfaces starting from that valve through the leakvalve and down to the sample and within the sample cell.

The bottom plot in Figure 4.2 shows the BE energy difference between the gas phase and the condensed phase peaks discussed above, tentatively attributed to a combination of changes in sample conductivity and in work function, now as a function of time. Obviously, this parameter closely follows the XPS signals and seems especially sensitive to small changes early on, when the changes in the XPS signals were still within the noise.

In order to interpret the data shown in Figure 4.2, we use an attenuation model described in the Section 4.2. In this model, adsorbed hexylamine ($C_6H_{15}N$) is assumed to be homogeneously distributed on the surface, represented by a layer of hexene (C_6H_{12}) covering a layer of ammonia (NH_3), which in turn sits on top of the ice. We thus assume that the hydrophilic amine group interacts closely with ice, while the hydrophobic aliphatic tails avoid the surface. The model allows calculating the photoemission signals and taking into account their attenuation, based on the assumed structure, and also taking into account the fact that kinetic energies associated with the measurement of O 1s, C 1s and N 1s are different (and thus the corresponding inelastic mean free paths), as the photon energy was the same. The attenuation is mostly relevant for the N 1s signal and for the O 1s signal, where the difference in absence and presence of HA is obvious (see appendix, Section 4.2.2, Figure A1). Assuming a saturated monolayer surface concentration of 3.0×10^{14} molecules/cm^2 for hexylamine, based on a range of values determined for other organic gases (alcohols and acids [49]), the model returns a value for the N/O and C/O normalized signal intensity ratio: 0.13 and 1.4, respectively. Taking into account 30% uncertainty associated with the monolayer coverage value, the confidence ranges are: $0.097<N/O<0.19$ and $0.92<C/O<2.2$. more details in the appendix, Section 4.2.3. Additional systematic uncertainties arise from the model assumptions, e.g., the fact that in the model the nitrogen heads are not buried within the top water layers of ice.

From comparing the estimated ratios with those observed, we can say based on the C 1s signals that we have about 1 monolayer, taking the upper uncertainty value for the monolayer. However, even taking the upper end of the error range, the measured N/O value is too high for a monolayer. In addition, the C/N ratio is very close to 6 (the y axes in Figure 4.2 are scaled with a factor of 6 as there are 6 carbons for 1 nitrogen in HA), which suggests that the HA molecules are not all pointing down as assumed in the model(C/N$\sim$10), but rather lying sideways, leading to an equal sensitivity for N and C. We note that the melting point of HA is $-22.9\,°C$. Figure 4.3 shows in a bar graph the results from different experiments. The first three bars are liquid jet XPS data of hexylamine solution (0.1M) measured at 3 different pH (see x-ticks labels). See also supporting Figure 4.8. The prevalence of the neutral amine and the ammonium species at pH above and below the pKa of 10.2, respectively, is as expected. We note that at the same solution concentration the neutral hexylamine has a higher preference for the interface than the charged hexylammonium, mostly driven by electrostatic effects that leads to the ion being drawn further into solution, which is similar to the behavior with acids [35] [55]. For the purpose of the present study, these measurements mainly serve as reference. The 4th bar (data set 7) represents the equilibrium reached at the end of the experiment with 2×10^{-5} mbar of HA on ice at -20°C (same data as in Figure 4.1 and Figure 4.2). The 5th bar (data set 2) is from the experiments of HA on ice at -20°C with $\sim 10^{-4}$ mbarof HA and the 6th bar (data set 5) is HA on ice at -30°C, with more than 10^{-4} mbar of HA because there was significant virtual dosing (from the walls after exposure of 10^{-3} mbar).

On the liquid jet data, we see as expected that the most basic solution contains mostly unprotonated amine while the most acidic one is fully protonated. At pH=10.2=pKa, we observe that the ratio of protonated to unprotonated is roughly 1:1, as expected.

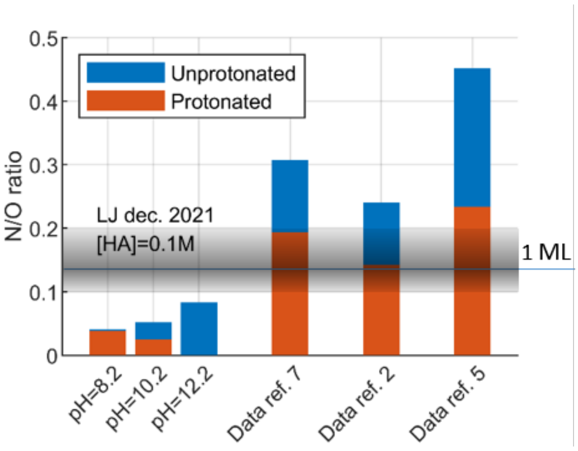

FIGURE 4.3: N/O ratios measured during different liquid jet (data labeled with pH value) and the ISS beamtimes (ice data set 7, 2 and 5). Respectively, the temperature of the ice data are -18.2°C, -19°C and -30°C and the HA dosing are 2e-5, 1e-4 and between e-4 and e-3 mbar, as described in SI 1.3. The fraction of protonated and unprotonated is indicated by the red and the blue color, respectively. The bars are ordered from left to right by increasing estimated surface concentration of HA. The shaded area indicates the expected N/O ratio for a saturated monolayer coverage, derived from the model calculation. The table in SI 2.3 summarizes the deconvolution results for the different experimental data.

Surprisingly, we see on the ice data that set 2 has lower N/O overall than data set 7, even though data set 2 has a five-time higher HA gas phase concentration, and both data sets are roughly at the same temperature. Our interpretation is that in both cases, we probably have a saturated monolayer of HA, and the difference in N/O is nothing else than the uncertainty due to the low signal-to-noise ratio of N 1s. Within this uncertainty, we can say that the amount of protonated HA is about the same in the three ice data. Only the unprotonated seems to significantly increase in the ice $-30\,^{\circ}\mathrm{C}$ data (data set 5), probably due to the higher gas phase concentration. If the protonated amine at $-20\,^{\circ}\mathrm{C}$ and low coverage seems to dominate, we observe almost equal partitioning of $\mathrm{R{-}NH_2}$ and $\mathrm{R{-}NH_3^+}$ at $-30\,^{\circ}\mathrm{C}$ and higher gas phase dosing. We see that the colder ice $-30\,^{\circ}\mathrm{C}$ leads to higher coverage of HA than the ice at $-20\,^{\circ}\mathrm{C}$. In turn, it seems, that the ice at $-30\,^{\circ}\mathrm{C}$ has the same proton availability as ice at $-20\,^{\circ}\mathrm{C}$ and that additional amine can only adsorb in the unprotonated form. The protonation of hexylamine depends on the self-ionization of water molecules to provide protons and the availability and mobility of these protons in the QLL. Above 1×10^{-4} mbar (data set 5), we probably enter the domain of hydrates or other condensed phases, such as bilayers, micelles, or other complex structures.

Figure 4.4 shows the oxygen K-edge NEXAFS spectra of HA adsorbed on ice at $-20\,^{\circ}\mathrm{C}$ and $-30\,^{\circ}\mathrm{C}$ (data set 2 and 5) together with liquid water and clean ice references.

We observe in Figure 4.4 that the liquid water spectrum differs from that of the clean ice at $-20\,^{\circ}\mathrm{C}$ in three different regions: (1) at the pre-edge (535 eV), the liquid spectrum has a little shoulder; (2) in the main edge (536-539 eV), the liquid spectrum exhibit higher absorption; (3) and at the post edge, the liquid has lower absorption than the clean ice spectrum. These differences have been interpreted as a decrease in

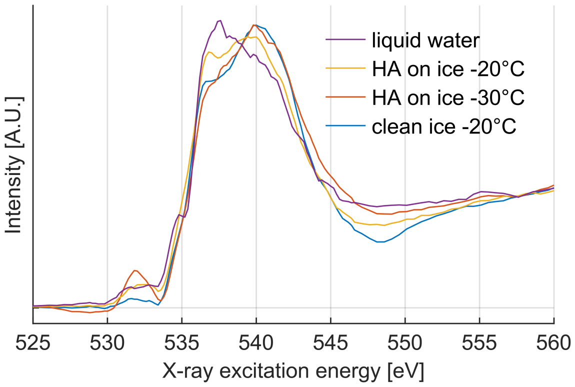

FIGURE 4.4: XAS spectra of HA adsorbed on ice at different temperatures. HA gas phase concentrations are 10^{-4} mbar for HA on ice −20 °C and between 10^{-4} and 1×10^{-3} mbar for HA on ice −30 °C. The data used in this figure are data set 1, 2, 5, 8 for liquid water, HA on ice −20 °C, HA on ice −30 °C, and clean ice −20 °C, respectively. The spectra are smoothed with 5 points (running average on 1 eV).

the number of water molecules in strong symmetric tetrahedral hydrogen bonds as in ice and an increase in weak asymmetric hydrogen bonds as in liquid water [47, 56, 57]. The HA on ice −20 °C spectrum shown in Figure 4.4 is in between the liquid and ice reference, suggesting that the hydrogen bonding structure is slighly disordered within the probing depth of the measurement. Yet, the HA on ice at −30 °C is merely identical to the ice reference, in the regions discussed above. To be more quantitative, we extract the pre-edge signal and the main-to-post-edge ratio from these spectra using the deconvolution methods described in [58] and similar to [46, 47]. The fitting parameters are described in supporting Table 4.4. After deconvolution, the pre-edge intensity is given by the area of the second Gaussian and the main-to post-edge ratio is calculated from the ratio of the 3rd and 4th to 5th and 6th Gaussians.

Figure 4.5 shows the liquid-like and the ice-like character for the different datasets (data set 1-8). On the x-axis, A and B refer to two analysis pathways to extract disorder information from NEXAFS, based on the pre-edge and main/post-edge ratio, respectively. In the bottom rectangular box labeled ‘ice-like’, we can see the ice −20 °C reference data (1), another clean ice data (6) and HA on ice at −30 °C (5). In the top box labeled ‘liquid-like’, we see the liquid reference (8) and several HA on ice at −20 °C data (2,3,4,7). See supporting Table 4.6 for the complete details about experimental conditions.

In general, we see a good correlation with temperature: the colder HA on ice at −30 °C lies in the ice-like region while the HA on ice at −20 °C has a liquid-like character, which is consistent with the temperature evolution that we observe with pure ice [8]. Surprisingly, when looking more carefully at the −20 °C data (data set 1, 2 3 4 6 7) we find that data 2 is in between data 1 and data 7, which is not the order that we would expect from the HA gas phase pressure which are 1×10^{-4} , 0 and 2×10^{-5} mbar, respectively. We can speculate that as the HA concentration increases from 0 to 2×10^{-5} mbar, the HA induces disorder on the ice surface; but as we reach a saturation level (data 2, 4, 3) the LL feature then decreases due to $R{-}NH_2$ ‘pulling’ on

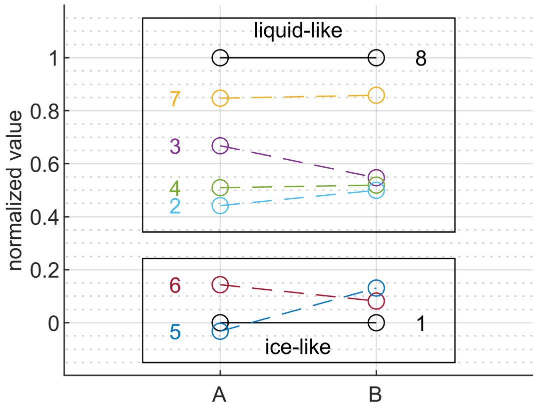

FIGURE 4.5: Liquid and ice character for different experimental conditions. On the x-axis, A and B refer to two analysis pathways to extract disorder information from NEXAFS, based on the pre-edge and main/post-edge ratio, respectively. In the bottom box labeled 'ice-like', we can see the ice −20 °C reference data (1), another clean ice data (6), and HA on ice at −30 °C (5). In the top box labeled 'liquid-like', we see the liquid reference (8) and several HA on ice at −20 °C data (2,3,4,7). See supporting Table 4.6 for the complete details about experimental conditions.

the dangling –OH of the ice, as seen in [25]. Looking at colder temperatures, we have only data ref. 5 at −30 °C which is ice-like despite the high HA (10^{-4} to 10^{-3} mbar).

For comparison, the surface disorder induced by 10^{-4} mbar of HA partial pressure on ice at -20°C (data ref. 2,3,4,7) is similar to that observed on ice at the same temperature with $\simeq 10^{-7}$ mbar of HCl partial pressure[1] [11]. A Weaker acid, HNO_3[2] dosed with a partial pressure of 1.3×10^{-3} mbar on ice at -40°C, induced a comparable[3] perturbation of the hydrogen bonding network [19] as data ref. 5 (at -30°C) from this work.

4.1.4 *Conclusions*

We have observed with in situ XPS the adsorption and desorption of HA from an ice sample at −20 °C. We have measured high coverage (about one monolayer) already at a partial pressure of 2×10^{-5} mbar. A bit more than half of the hexylamine is protonated at such coverage which suggests that protons are available on the surface of ice at −20 °C. It would be interesting to do the same experiment at a higher temperature (for example, −10 °C) to see if the thicker QLL can host more HA or if the HA penetrates deeper into the ice.

At −20 °C, the surface coverage obtained under 2×10^{-5} mbar of HA partial pressure, the HA increases the fraction of water molecules in disordered configurations, as seen

---

[1] Pressure estimated from XPS measurement and crude extrapolation from the Langmuir constant, thus highly uncertain. The same experiment with 10x lower HCl concentration didn't lead to any observable change in the O K-edge XAS.

[2] produced by NO_2 hydrolysis on ice

[3] the original publication has fitted the XAS spectra of ice + HNO_3 with a linear combination of 80% ice and 20% HNO_3 solution

with PEY-XAS. At −30 °C however, no perturbation of the hydrogen bonding network has been observed, despite the higher HA partial pressure in the gas phase.

References

1. Box, J. E., Fettweis, X., Stroeve, J. C., Tedesco, M., Hall, D. K. & Steffen, K. "Greenland ice sheet albedo feedback: thermodynamics and atmospheric drivers". *The Cryosphere* **6**, 821–839 (2012).
2. Dash, J. G., Fu, H. Y. & Wettlaufer, J. S. "The Premelting of Ice and Its Environmental Consequences". *Reports on Progress in Physics* **58**, 115–167 (1995).
3. Grannas, A. M., Bogdal, C., Hageman, K. J., Halsall, C., Harner, T., Hung, H., Kallenborn, R., Klan, P., Klanova, J., Macdonald, R. W., Meyer, T. & Wania, F. "The role of the global cryosphere in the fate of organic contaminants". *Atmospheric Chemistry and Physics* **13**, 3271–3305 (2013).
4. Grannas, A. M., Jones, A. E., Dibb, J., Ammann, M., Anastasio, C., Beine, H. J., Bergin, M., Bottenheim, J., Boxe, C. S., Carver, G., Chen, G., Crawford, J. H., Domine, F., Frey, M. M., Guzman, M. I., Heard, D. E., Helmig, D., Hoffmann, M. R., Honrath, R. E., Huey, L. G., Hutterli, M., Jacobi, H. W., Klan, P., Lefer, B., McConnell, J., Plane, J., Sander, R., Savarino, J., Shepson, P. B., Simpson, W. R., Sodeau, J. R., von Glasow, R., Weller, R., Wolff, E. W. & Zhu, T. "An overview of snow photochemistry: evidence, mechanisms and impacts". *Atmospheric Chemistry and Physics* **7**, 4329–4373 (2007).
5. Huthwelker, T., Ammann, M. & Peter, T. "The Uptake of Acidic Gases on Ice". *Chemical Reviews* **106**, 1375–1444 (2006).
6. Neu, J. & Prather, M. "Toward a more physical representation of precipitation scavenging in global chemistry models: cloud overlap and ice physics and their impact on tropospheric ozone". *Atmospheric Chemistry and Physics* **12**, 3289–3310 (2012).
7. Bartels-Rausch, T., Jacobi, H. W., Kahan, T. F., Thomas, J. L., Thomson, E. S., Abbatt, J. P. D., Ammann, M., Blackford, J. R., Bluhm, H., Boxe, C., Domine, F., Frey, M. M., Gladich, I., Guzman, M. I., Heger, D., Huthwelker, T., Klan, P., Kuhs, W. F., Kuo, M. H., Maus, S., Moussa, S. G., McNeill, V. F., Newberg, J. T., Pettersson, J. B. C., Roeselova, M. & Sodeau, J. R. "A review of air-ice chemical and physical interactions (AICI): liquids, quasi-liquids, and solids in snow". *Atmospheric Chemistry and Physics* **14**, 1587–1633 (2014).
8. Bluhm, H., Ogletree, D. F., Fadley, C. S., Hussain, Z. & Salmeron, N. "The premelting of ice studied with photoelectron spectroscopy". *Journal of Physics-Condensed Matter* **14**, L227–L233 (2002).
9. McNeill, V. F., Loerting, T., Geiger, F. M., Trout, B. L. & Molina, M. J. "Hydrogen chloride-induced surface disordering on ice". *Proceedings of the National Academy of Sciences of the United States of America* **103**, 9422–9427 (2006).
10. Nilsson, A., Nordlund, D., Waluyo, I., Huang, N., Ogasawara, H., Kaya, S., Bergmann, U., Naslund, L. A., Ostrom, H., Wernet, P., Andersson, K. J., Schiros, T. & Pettersson, L. G. M. "X-ray absorption spectroscopy and X-ray Raman scattering of water and ice; an experimental view". *Journal of Electron Spectroscopy and Related Phenomena* **177**, 99–129 (2010).

11. Kong, X., Waldner, A., Orlando, F., Artiglia, L., Huthwelker, T., Ammann, M. & Bartels-Rausch, T. "Coexistence of Physisorbed and Solvated HCl at Warm Ice Surfaces". *J Phys Chem Lett* **8**, 4757–4762 (2017).
12. Abbatt, J. P. D., Bartels-Rausch, T., Ullerstam, M. & Ye, T. J. "Uptake of acetone, ethanol and benzene to snow and ice: effects of surface area and temperature". *Environmental Research Letters* **3** (2008).
13. Abbatt, J. P. "Interactions of atmospheric trace gases with ice surfaces: Adsorption and reaction". *Chemical reviews* **103**, 4783–4800 (2003).
14. Bartels-Rausch, T., Brigante, M., Elshorbany, Y. F., Ammann, M., D'Anna, B., George, C., Stemmler, K., Ndour, M. & Kleffmann, J. "Humic acid in ice Photo-enhanced conversion of nitrogen dioxide into nitrous acid". *Atmospheric Environment* **44**, 5443–5450 (2010).
15. Bartels-Rausch, T., Eichler, B., Zimmermann, P., Gaggeler, H. W. & Ammann, M. "The adsorption enthalpy of nitrogen oxides on crystalline ice". *Atmospheric Chemistry and Physics* **2**, 235–247 (2002).
16. Bartels-Rausch, T., Orlando, F., Kong, X., Artiglia, L. & Ammann, M. "Experimental Evidence for the Formation of Solvation Shells by Soluble Species at a Nonuniform Air–Ice Interface". *ACS Earth and Space Chemistry* **1**, 572–579 (2017).
17. Kerbrat, M., Huthwelker, T., Bartels-Rausch, T., Gaggeler, H. W. & Ammann, M. "Co-adsorption of acetic acid and nitrous acid on ice". *Physical Chemistry Chemical Physics* **12**, 7194–7202 (2010).
18. Krepelova, A., Bartels-Rausch, T., Brown, M. A., Bluhm, H. & Ammann, M. "Adsorption of Acetic Acid on Ice Studied by Ambient-Pressure XPS and Partial-Electron-Yield NEXAFS Spectroscopy at 230-240 K". *Journal of Physical Chemistry A* **117**, 401–409 (2013).
19. Krepelova, A., Newberg, J. T., Huthwelker, T., Bluhm, H. & Ammann, M. "The nature of nitrate at the ice surface studied by XPS and NEXAFS". *Physical Chemistry Chemical Physics* **12**, 8870–8880 (2010).
20. McNeill, V. F., Grannas, A. M., Abbatt, J. P. D., Ammann, M., Ariya, P., Bartels-Rausch, T., Domine, F., Donaldson, D. J., Guzman, M. I., Heger, D., Kahan, T. F., Klan, P., Masclin, S., Toubin, C. & Voisin, D. "Organics in environmental ices: sources, chemistry, and impacts". *Atmospheric Chemistry and Physics* **12**, 9653–9678 (2012).
21. Moussa, S. G., Kuo, M. H. & McNeill, V. F. "Nitric acid-induced surface disordering on ice". *Physical Chemistry Chemical Physics* **15**, 10989–10995 (2013).
22. Ulrich, T., Ammann, M., Leutwyler, S. & Bartels-Rausch, T. "The adsorption of peroxynitric acid on ice between 230 K and 253 K". *Atmospheric Chemistry and Physics* **12**, 1833–1845 (2012).
23. Zimmermann, S., Kippenberger, M., Schuster, G. & Crowley, J. N. "Adsorption isotherms for hydrogen chloride (HCl) on ice surfaces between 190 and 220 K". *Physical Chemistry Chemical Physics* **18**, 13799–13810 (2016).

24. Nordlund, D., Ogasawara, H., Wernet, P., Nyberg, M., Odelius, M., Pettersson, L. & Nilsson, A. "Surface structure of thin ice films". *Chemical physics letters* **395**, 161–165 (2004).
25. Wernet, P., Nordlund, D., Bergmann, U., Cavalleri, M., Odelius, M., Ogasawara, H., Näslund, L. Å., Hirsch, T. K., Ojamäe, L., Glatzel, P., Pettersson, L. G. M. & Nilsson, A. "The Structure of the First Coordination Shell in Liquid Water". *Science* **304**, 995–999 (2004).
26. Ge, X., Wexler, A. S. & Clegg, S. L. "Atmospheric amines – Part I. A review". *Atmospheric Environment* **45**, 524–546 (2011).
27. Cornell, S., Jickells, T., Cape, J., Rowland, A. & Duce, R. "Organic nitrogen deposition on land and coastal environments: a review of methods and data". *Atmospheric Environment* **37**, 2173–2191 (2003).
28. Sorooshian, A., Murphy, S. M., Hersey, S., Gates, H., Padro, L. T., Nenes, A., Brechtel, F. J., Jonsson, H., Flagan, R. C. & Seinfeld, J. H. "Comprehensive airborne characterization of aerosol from a major bovine source". *Atmos. Chem. Phys.* **8**, 5489–5520 (2008).
29. Schade, G. W. & Crutzen, P. J. "Emission of aliphatic amines from animal husbandry and their reactions: Potential source of N2O and HCN". *Journal of Atmospheric Chemistry* **22**, 319–346 (1995).
30. Noziere, B., Dziedzic, P. & Córdova, A. "Products and kinetics of the liquid-phase reaction of glyoxal catalyzed by ammonium ions (NH4+)". *The Journal of Physical Chemistry A* **113**, 231–237 (2009).
31. Galloway, M. M., Chhabra, P. S., Chan, A. W. H., Surratt, J. D., Flagan, R. C., Seinfeld, J. H. & Keutsch, F. N. "Glyoxal uptake on ammonium sulphate seed aerosol: reaction products and reversibility of uptake under dark and irradiated conditions". *Atmospheric Chemistry and Physics* **9**, 3331–3345 (2009).
32. Kowalczuk, P. B., Zawala, J., Drzymala, J. & Malysa, K. "Influence of hexylamine on kinetics of flotation and bubble attachment to the quartz surface". *Separation Science and Technology* **51**, 2681–2690 (2016).
33. Ammann, M., Artiglia, L. & Bartels-Rausch, T. in *Physical Chemistry of Gas-Liquid Interfaces* (eds Faust, J. A. & House, J. E.) 135–166 (Elsevier, 2018).
34. Bluhm, H. "Photoelectron spectroscopy of surfaces under humid conditions". *Journal of Electron Spectroscopy and Related Phenomena* **177**, 71–84 (2010).
35. Kong, X. R., Waldner, A., Orlando, F., Artiglia, L., Huthwelker, T., Ammann, M. & Bartels-Rausch, T. "Coexistence of Physisorbed and Solvated HCl at Warm Ice Surfaces". *Journal of Physical Chemistry Letters* **8**, 4757–4762 (2017).
36. Orlando, F., Artiglia, L., Yang, H. Y., Kong, X. R., Roy, K., Waldner, A., Chen, S. Z., Bartels-Rausch, T. & Ammann, M. "Disordered Adsorbed Water Layers on TiO2 Nanoparticles under Subsaturated Humidity Conditions at 235 K". *Journal of Physical Chemistry Letters* **10**, 7433–7438 (2019).

37. Orlando, F., Waldner, A., Bartels-Rausch, T., Birrer, M., Kato, S., Lee, M. T., Proff, C., Huthwelker, T., Kleibert, A., van Bokhoven, J. & Ammann, M. "The Environmental Photochemistry of Oxide Surfaces and the Nature of Frozen Salt Solutions: A New in Situ XPS Approach". *Topics in Catalysis* **59**, 591–604 (2016).

38. Waldner, A., Artiglia, L., Kong, X. R., Orlando, F., Huthwelker, T., Ammann, M. & Bartels-Rausch, T. "Pre-melting and the adsorption of formic acid at the air-ice interface at 253 K as seen by NEXAFS and XPS". *Physical Chemistry Chemical Physics* **20**, 24408–24417 (2018).

39. Brown, M. A., Redondo, A. B., Jordan, I., Duyckaerts, N., Lee, M.-T., Ammann, M., Nolting, F., Kleibert, A., Huthwelker, T., Mächler, J.-P., Birrer, M., Honegger, J., Wetter, R., Wörner, H. J. & Bokhoven, J. A. v. "A new endstation at the Swiss Light Source for ultraviolet photoelectron spectroscopy, X-ray photoelectron spectroscopy, and X-ray absorption spectroscopy measurements of liquid solutions". *Review of Scientific Instruments* **84**, 073904 (2013).

40. Howard Rytting, J., Huston, L. P. & Higuchi, T. "Thermodynamic Group Contributions for Hydroxyl, Amino, and Methylene Groups". *Journal of Pharmaceutical Sciences* **67**, 615–618 (1978).

41. Sander, R. "Compilation of Henry's law constants (version 4.0) for water as solvent". *Atmospheric Chemistry and Physics* **15**, 4399–4981 (2015).

42. TRCVP, Vapor Pressure Database, Version 2.2P, Thermodynamic Research Center, Texas AM University, College Station, TX.

43. NIST. *webbook* Web Page.

44. Ratner, B. D. & Castner, D. G. "Electron spectroscopy for chemical analysis". *Surface analysis: the principal techniques* **2** (2009).

45. Yang, H., Boucly, A., Gabathuler, J. P., Bartels-Rausch, T., Artiglia, L. & Ammann, M. "Ordered Hydrogen Bonding Structure of Water Molecules Adsorbed on Silver Iodide Particles under Subsaturated Conditions". *The Journal of Physical Chemistry C* **125**, 11628–11635 (2021).

46. Cappa, C. D., Smith, J. D., Wilson, K. R., Messer, B. M., Gilles, M. K., Cohen, R. C. & Saykally, R. J. "Effects of alkali metal halide salts on the hydrogen bond network of liquid water". *Journal of Physical Chemistry B* **109**, 7046–7052 (2005).

47. Nilsson, A., Nordlund, D., Waluyo, I., Huang, N., Ogasawara, H., Kaya, S., Bergmann, U., Naslund, L. A., Ostrom, H., Wernet, P., Andersson, K. J., Schiros, T. & Pettersson, L. G. M. "X-ray absorption spectroscopy and X-ray Raman scattering of water and ice; an experimental view". *Journal of Electron Spectroscopy and Related Phenomena* **177**, 99–129 (2010).

48. Brown, M. A., Redondo, A. B., Jordan, I., Duyckaerts, N., Lee, M.-T., Ammann, M., Nolting, F., Kleibert, A., Huthwelker, T., Mächler, J.-P., Birrer, M., Honegger, J., Wetter, R., Wörner, H. J. & Bokhoven, J. A. v. "A new endstation at the Swiss Light Source for ultraviolet photoelectron spectroscopy, X-ray photoelectron spectroscopy, and X-ray absorption spectroscopy measurements of liquid solutions". *Review of Scientific Instruments* **84**, 073904 (2013).

49. Crowley, J. N., Ammann, M., Cox, R., Hynes, R., Jenkin, M. E., Mellouki, A., Rossi, M. J., Troe, J. & Wallington, T. J. "Evaluated kinetic and photochemical data for atmospheric chemistry: Volume V–heterogeneous reactions on solid substrates". *Atmospheric Chemistry and Physics* **10**, 9059–9223 (2010).

50. Fransson, T., Harada, Y., Kosugi, N., Besley, N. A., Winter, B., Rehr, J. J., Pettersson, L. G. M. & Nilsson, A. "X-ray and Electron Spectroscopy of Water". *Chemical Reviews* **116**, 7551–7569 (2016).

51. Greczynski, G. & Hultman, L. "X-ray photoelectron spectroscopy: Towards reliable binding energy referencing". *Progress in Materials Science* **107**, 100591 (2020).

52. Taucher, T. C., Hehn, I., Hofmann, O. T., Zharnikov, M. & Zojer, E. "Understanding Chemical versus Electrostatic Shifts in X-ray Photoelectron Spectra of Organic Self-Assembled Monolayers". *The Journal of Physical Chemistry C* **120**, 3428–3437 (2016).

53. Venkataraman, N. V., Zürcher, S., Rossi, A., Lee, S., Naujoks, N. & Spencer, N. D. "Spatial Tuning of the Metal Work Function by Means of Alkanethiol and Fluorinated Alkanethiol Gradients". *The Journal of Physical Chemistry C* **113**, 5620–5628 (2009).

54. Zojer, E., Taucher, T. C. & Hofmann, O. T. "The Impact of Dipolar Layers on the Electronic Properties of Organic/Inorganic Hybrid Interfaces". *Advanced Materials Interfaces* **6**, 1900581 (2019).

55. Lee, M.-T., Orlando, F., Artiglia, L., Chen, S. & Ammann, M. "Chemical Composition and Properties of the Liquid–Vapor Interface of Aqueous C1 to C4 Monofunctional Acid and Alcohol Solutions". *The Journal of Physical Chemistry A* **120**, 9749–9758 (2016).

56. Bluhm, H., Ogletree, D. F., Fadley, C. S., Hussain, Z. & Salmeron, N. "The premelting of ice studied with photoelectron spectroscopy". *Journal of Physics-Condensed Matter* **14**, L227–L233 (2002).

57. Niskanen, J., Fondell, M., Sahle, C. J., Eckert, S., Jay, R. M., Gilmore, K., Pietzsch, A., Dantz, M., Lu, X., McNally, D. E., Schmitt, T., Vaz da Cruz, V., Kimberg, V., Gel'mukhanov, F. & Föhlisch, A. "Compatibility of quantitative X-ray spectroscopy with continuous distribution models of water at ambient conditions". *Proceedings of the National Academy of Sciences* **116**, 4058–4063 (2019).

58. Yang, H., Boucly, A., **Gabathuler, Jérôme Philippe**, Bartels-Rausch, T., Artiglia, L. & Ammann, M. "Ordered Hydrogen Bonding Structure of Water Molecules Adsorbed on Silver Iodide Particles under Subsaturated Conditions". *The Journal of Physical Chemistry C* **125**, 11628–11635 (2021).

Appendix: Model to estimate the XPS signal intensity ratio C/O and N/O for hexylamine on ice

We assume that the nitrogen head of adsorbed hexylamine is pointing towards the interior of ice. To take into account the attenuation of the N 1s signal due to the aliphatic carbon tail above it, we make a 2-layer model shown in the figure below to represent hexylamine on ice: Hexylamine (C6H15N) -> hexene (C6H12) + ammonia (NH3). Of course, the ‘reality’ looks a bit different! At least for the hydrated RNH2 and RNH3+ the N mixes with the top layer of water.

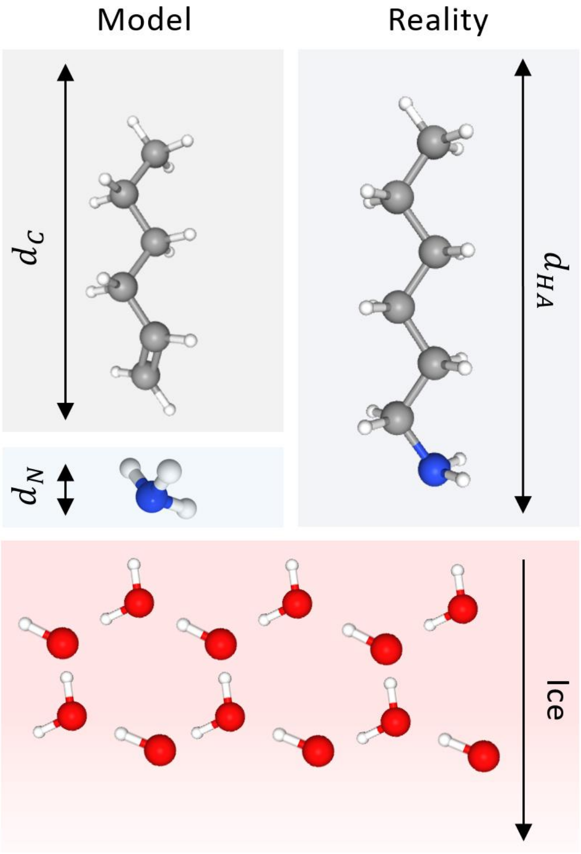

For the sake of simplicity, we set the density of hexene and ammonia to 0.77g/cm3, corresponding to that of hexylamine. We set $d_C = \frac{6}{7} d_{HA}$, and $d_N = \frac{1}{7} d_{HA}$, corresponding to the atomic ratio of C and N in HA. Naturally, we have $d_{HA} = d_N + d_C$. The IMFP at the respective KE are retrieved from QUASES software for each material at the imposed density of 0.77g/cm3. The KE is calculated for a photon energy hv=700 eV.

region	KE [eV]	IMFP in $\boldsymbol{C_6H_{12}}$	IMFP in $\boldsymbol{NH_3}$	IMFP in **Ice**	IMFP that we use:
C1s	$415\ eV$	1.436	1.47	1.785	$\lambda_{415} = 1.45\ nm$
N1s	$300\ eV$	1.137	1.165	1.425	$\lambda_{300} = 1.15\ nm$
O1s	$165\ eV$	0.768	0.791	0.992	$\lambda_{165} = 0.78\ nm$

We see that despite higher density, IMFP in ice is larger than in hexene or ammonia whose density is set to $\rho = 0.77\ g \cdot cm^{-3}$. For the sake of simplicity (to avoid triple integral) we use the IMFP of the last column. This simplification overestimates the self-attenuation in ice, if we trust the IMFP value for ice. We can then calculate the expected surface concentration as seen by the XPS measurement:

$$S_C \propto n_c \int_0^{d_C} e^{-\frac{x}{\lambda_{415}}} dx$$

$$S_N \propto n_N \int_{d_C}^{d_C+d_N} e^{-\frac{x}{\lambda_{300}}} dx$$

$$S_O \propto n_O \int_{d_C+d_N}^{+\infty} e^{-\frac{x}{\lambda_{165}}} dx$$

where $n_x = \mathrm{N_x} \cdot \rho_x \cdot \frac{Av}{M_x}$ is the atomic number density in [#/cm3], ρ_x is the density of the material [g/cm3], $\mathrm{M_x}$ is the molecular mass, and $\mathrm{N_x}$ is the number of atoms of interest in the molecule i.e. 6 for carbon in hexene, 1 for nitrogen in ammonia and 1 for oxygen in water.

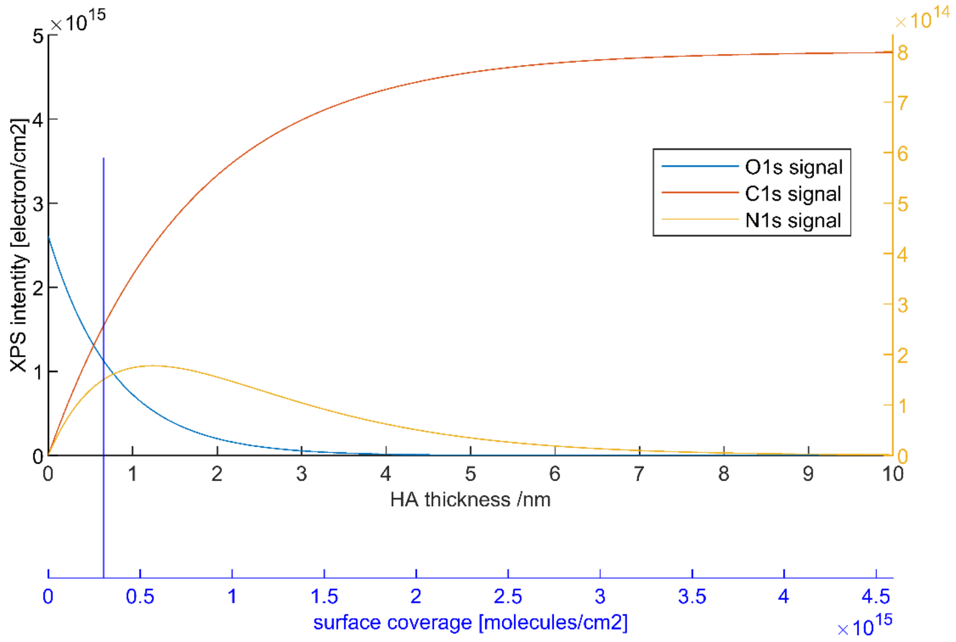

Figure A1: Calculated XPS intensity as a function of HA thickness. The blue x-axis represents the conversion of HA thickness into equivalent surface coverage. The vertical blue line indicates the thickness of HA, at which we have a saturated monolayer. The value in surface coverage is 3e14 molecules/cm2. The oxygen signal at thickness = 0 is about 2 times lower than the carbon signal at the infinite thickness. This depends on the atomic number density , which is slightly higher for hexene but is mostly due to the IMFP of oxygen electrons detected at 165eV kinetic energy. The C1s probes ~2x deeper volume.

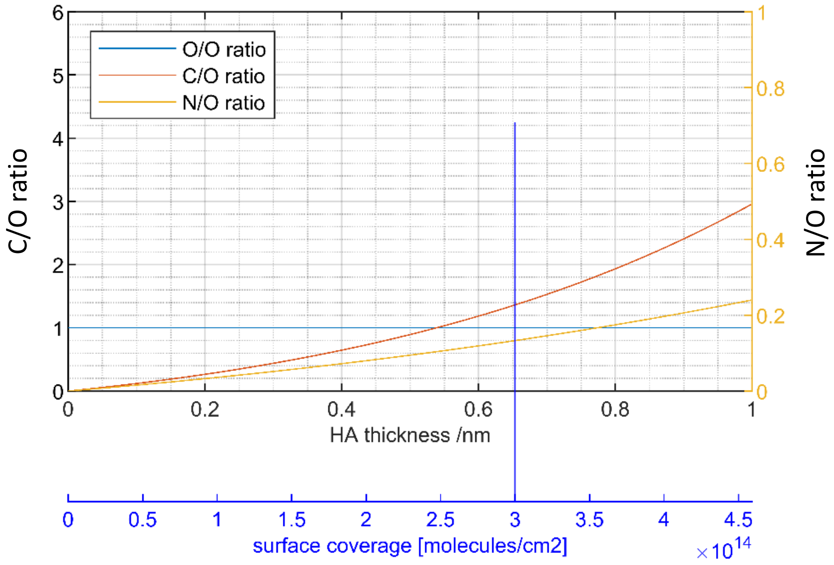

Figure A2: Calculated C/O and N/O ratio as a function of the HA thickness, or equivalent surface coverage. From the graph, we can read the value for the N/O and C/O ratio that we expect for a monolayer: 0.1348 and 1.3856, respectively. Taking into account 30% uncertainty from the monolayer coverage value, we can say 0.0970<N/O<0.1901 and 0.9211<C/O<2.1614. Intuitively, we would expect C/N ratio to be 6, but since we have more attenuation in the N signal due to the carbon covering it, this ratio is higher, around 10. On this topic, we can also consider adv. Carbon which would contribute to the C1s signal and attenuate the N1s and O1s, therefore increasing the C/O value. There could also be adventitious nitrogen, generated from beam-damaged hexylamine.

Table A1: The lower, best and higher estimate of the N/O and C/O

	Lower estimate	**Expected value**	***Higher estimate***
N/O	*0.0970*	**0.1348**	*0.1901*
C/O	*0.9211*	**1.3856**	*2.1614*

Supporting information for the manuscript in preparation, which will be published as: Gabathuler, J. P., Manoharan, Y., Artiglia, L. & Ammann, M. “Adsorption of Hexylamine on ice, as seen by near ambient pressure XPS” (in preparation)

4.3 SUPPORTING INFORMATION

4.3.1 *Dosing system*

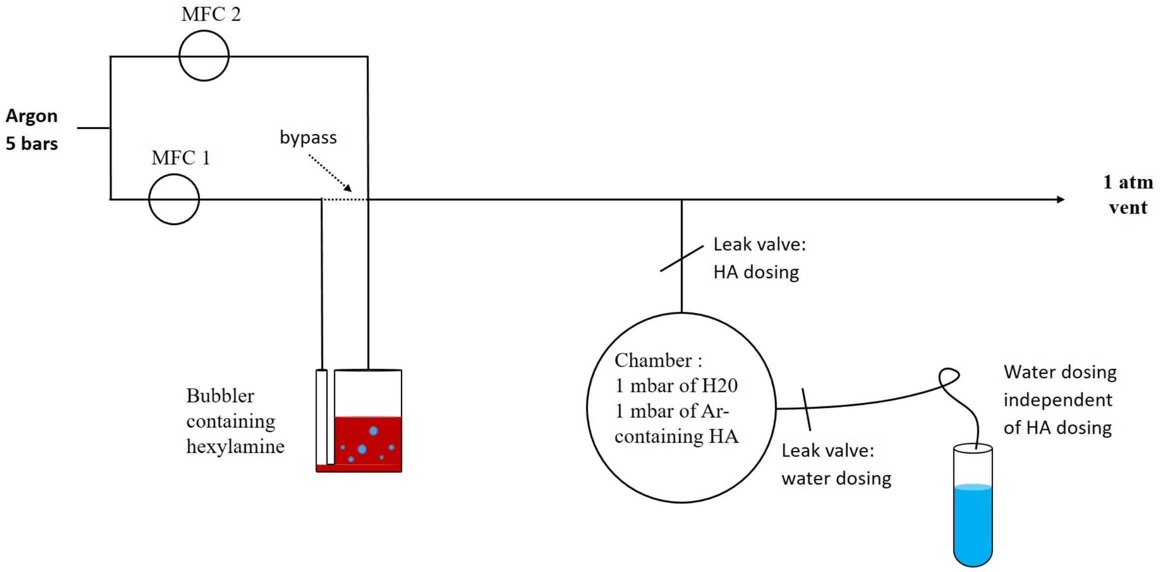

FIGURE 4.6: Dosing system that we have used to dose water vapor and hexylamine (HA) during the different experiments reported in this publication. The content and the temperature of the bubbler have been optimized from beamtime to beamtime and is specified in the column ‘dosing’ of the table in Table 4.6. The leak valve for water vapor was adjusted to maintain a constant partial pressure of H2O of 1 mbar in the chamber. The leak valve for the Ar/HA mixture was adjusted to obtain a constant partial pressure of Ar of 1 mbar in the chamber. Changing the liquid composition of the bubbler allowed to precisely control the HA gas-phase partial pressure in the range 10^{-6} to 10^{-3} mbar. The chamber’s gas then flows to the analyzer, via the cone aperture. MFC denotes mass flow controller.

4.3.1.1 *Argon*

TABLE 4.1: Argon presents XPS traveling peaks with the following binding energies:

Region:	Ar 2s	Ar 2p	Ar 3s	Ar 3p
BE [eV]	326	250	29.3	15

4.3.2 *Experiments & analysis*

4.3.2.1 *Background subtraction*

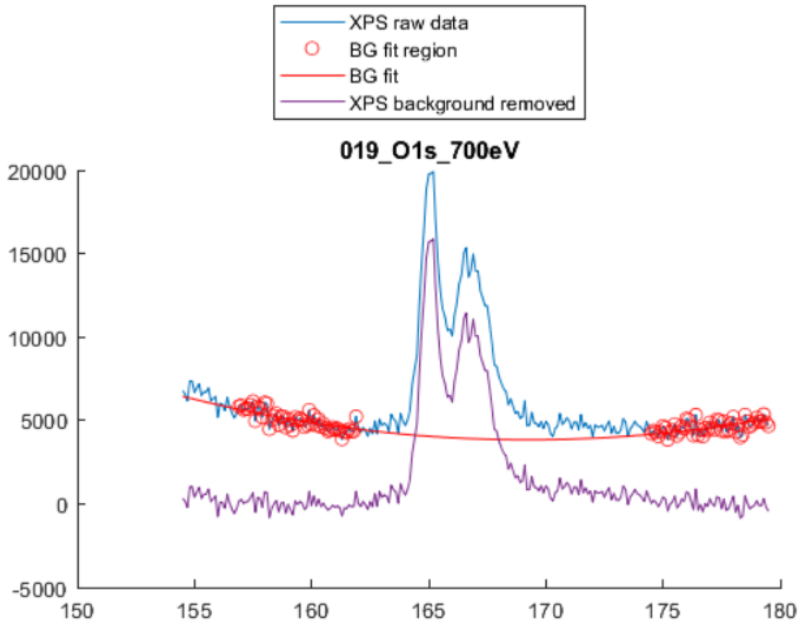

FIGURE 4.7: O 1s spectra example together with the second order polynomial fit to subtract the background

4.3.2.2 *XPS peak fitting*

TABLE 4.3: Constraints used for peak fitting with Gaussians. Binding energy positions are taken from [2].

	O 1s gas phase	O 1s ice	C 1s C-C	C 1s C-N	C 1s C-O adv.	C 1s C=O adv	N 1s NH2	N 1s NH2 ads.	N 1s NH3+
Position [eV]	535.0 ±1	532.4 ±1	285.0 ±0.05	286.0 ±0.05	286.5 ±0.10	288.25 ±0.25	399.4 ±0.05	400.0 ±0.5	401.7 ±0.05
$\frac{\textbf{FWHM}^{a}\,[\textbf{eV}]}{\textbf{1.665}}$	0.5 ±50%	1.0 ±50%	0.8 fixed	0.8 fixed	0.8 ±10%	1.0 ±50%	0.9 fixed	0.9 fixed	0.9 fixed

---

[a] FWHM= 1.665*c where c is the width in the Gaussian form a*exp(-((x-b)/c)^2)

4.3.2.3 *PEY-XAS analysis*

The NEXAFS data is processed with the following steps:

1. Import - the first step is to import the data from the h5 file structure, which is the output file of the PShell software that is used to communicate with the electron analyzer. At this step, the beamline shift corresponding to the monochromator offset is corrected on the photon energy value. Here we use 1.6 eV, which is a typical offset of our monochromator, based on the water gas phase 2b2 peak.

2. Average - After importing, the repetitions that are overlapping within a tolerance of 10%/hour are selected, and averaged. This ensures that only spectra are averaged, during which the ice is stable during acquisition. Ice growing towards or retracting away from the sampling aperture would lead to loss of signal intensity.

3. I0 – the spectra are normalized to the photon flux. The photon flux is measured with a photodiode (AXUV100GDS from ITW Opto Diode) at the location of the sample, usually measured in vacuum at the end of each beamtime. The photon flux measurement allows taking into account any absorption feature such as oxygen contaminations in the beamline optics, which might change from beamtime to beamtime. This specific beamline has the particularity to contain a high fraction of second-order light (45% at 500eV and 37% at 600eV), which may lead to underestimating such absorption features. The calculation of the first order flux as well as the gas phase absorption for the actual pressure of the experiment is performed at this step in the analysis.

4. Water gas phase removal – this step allows removing the gas phase contribution in the PEY-XAS spectra. Indeed, the electrons are sampled from the surface of the ice, but also from the gas phase within the volume, which is intersected by the X-ray beam and which is within the acceptance volume of the analyzer. The contribution of gas-phase water is removed in a way that the points between 534 and 534.4 eV are aligned with the linear pre-edge background. This is based on the assumption that oxygen in carbon-oxygen bonds does not contribute in this range and also that it is below the rise of pre-edge of the O K - edge.

5. Background - the background is removed as a linear fit to the region 517-530eV. Since the second order light produces most of the background in PEY-XAS, and its fraction may vary between experiments, we allow ourselves to vary the slope of the background fit such that the resulting main edge average intensity from 537.6 to 541.6 eV is 2.2 that of the tail from 556.6 to 561.6 eV, as calculated from the spectra of figure 1C in [3]. With such treatment of the background, the final spectra should cross at the isosbestic point (539.2eV) and the tails should meet at 560 eV after normalization [3].

6. Normalization – the spectra is finally normalized to the tail [556.6-561.6eV] however, normalizing to the main edge ([537.6-541.6]) would give the same result because of the manipulation in step 5).

7. Smoothing – the spectra in Fig. 4 has been smoothed using the Matlab® smooth function with 5 points or 1 eV.

4.3.2.4 *Deconvolution signal extraction*

TABLE 4.4: Fitting parameters to represent O K-edge spectra by 7 Gaussian components. The fit uses the least squares method in the range 515 eV to 545 eV.

Peak nº	1	2	3	4	5	6	7
Designation	C=O	Pre-edge	Main edge	Main edge	Post-edge	Post-edge	Background
Position range [eV]	532.0-532.5	534.7 (fixed)	536.2-536.5	537.7-538	539.7-540	540.7-541	545-550
$\frac{\textbf{FWHM}^{a}[\textbf{eV}]}{\textbf{1.665}}$	0.5-1	0.5	1	1.5	1	3	7

---

[a] FWHM= 1.665*c where c is the width in the Gaussian form a*exp(-((x-b)/c)^{2})

TABLE 4.6: Experimental description of the different data sets presented in the main text. RT denotes room temperature.

Data set #	**Sample**	**BT**	**Sample Temp.**	**Gas phase**	**HA dosing**	**Comment**
pH= 8.2	0.1M HA solution, pH=8.2	dec. 2021	RT	vacuum	Does not apply	Liquid jet XPS
pH= 10.2	0.1M HA solution, pH=pKa	dec. 2021	RT	vacuum	Does not apply	Liquid jet XPS
pH= 12.2	0.1M HA solution, pH=12.2	dec. 2021	RT	vacuum	Does not apply	Liquid jet XPS
1	Clean ice	23.02.2022	-19.9	1 mbar H_2O 1 mbar Ar	No dosing	Reference
2	HA on ice	24.02.2022	-19.0	1 mbar H_2O 1 mbar Ar 10^{-4} mbar HA	from 32 mM HA solution	Bubbler at RT
3	HA on ice	24.02.2022	-19.0	1 mbar H_2O 1 mbar Ar 10^{-3} mbar HA	from pure HA	Bubbler at RT. Condensation[a]
4	HA on ice	24.02.2022	-19.0	1 mbar H_2O 1 mbar Ar $\sim$ 10^{-3} mbar HA	from pure HA	Bubbler at RT. HA bypassed, dosing from the walls.
5	HA on ice	25.02.2022	-29.0	0.4 mbar H_2O 1 mbar Ar 10^{-4} to 10^{-3} mbar HA[b]	from pure HA	Bubbler at RT.
6	Clean ice	26.05.2022	-18.2	1 mbar H_2O 1 mbar Ar	No dosing	
7	HA on ice	27.05.2022	-18.2	1 mbar H_2O 1 mbar Ar $2{\cdot}10^{-5}$mbar HA	from pure HA at 0 °C	Bubbler immersed in an ice bath[c].
8	Liquid water	March 2019	+0.5°C	6.4 mbar H20	No dosing	Reference[d].

---

c [a] Condensation of HA on lines and in the leak valve, perturbating the flow to the chamber.

c [b] Dosing 10^{-4} and dosing from the walls. Dosing 10^{-4} didn't change the C 1s spectra compared to not dosing. There was 10^{3} mbar in the chamber the day before.

c [c] This seemed to be the best dosing approach for low partial pressures of HA

c [d] This liquid water reference was a thin water film condensing on the sample holder

4.3.3 *Beamtime data*

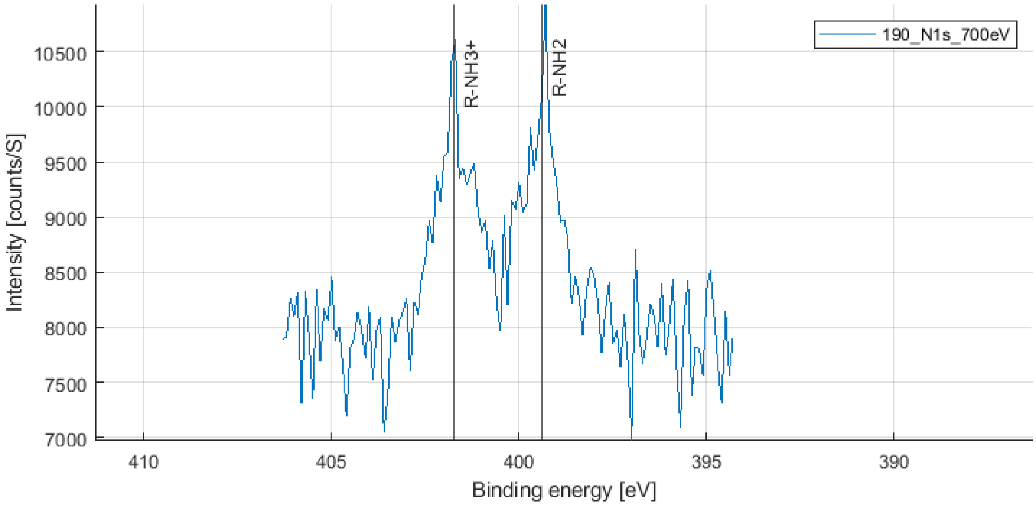

FIGURE 4.8: Liquid jet N 1s spectra of 0.1M HA solution at pH=pKa. The binding energy difference between the R$-$NH$_2$ and R$-$NH$_3^+$ is 2.3 eV, in agreement with Brown et al. [4].

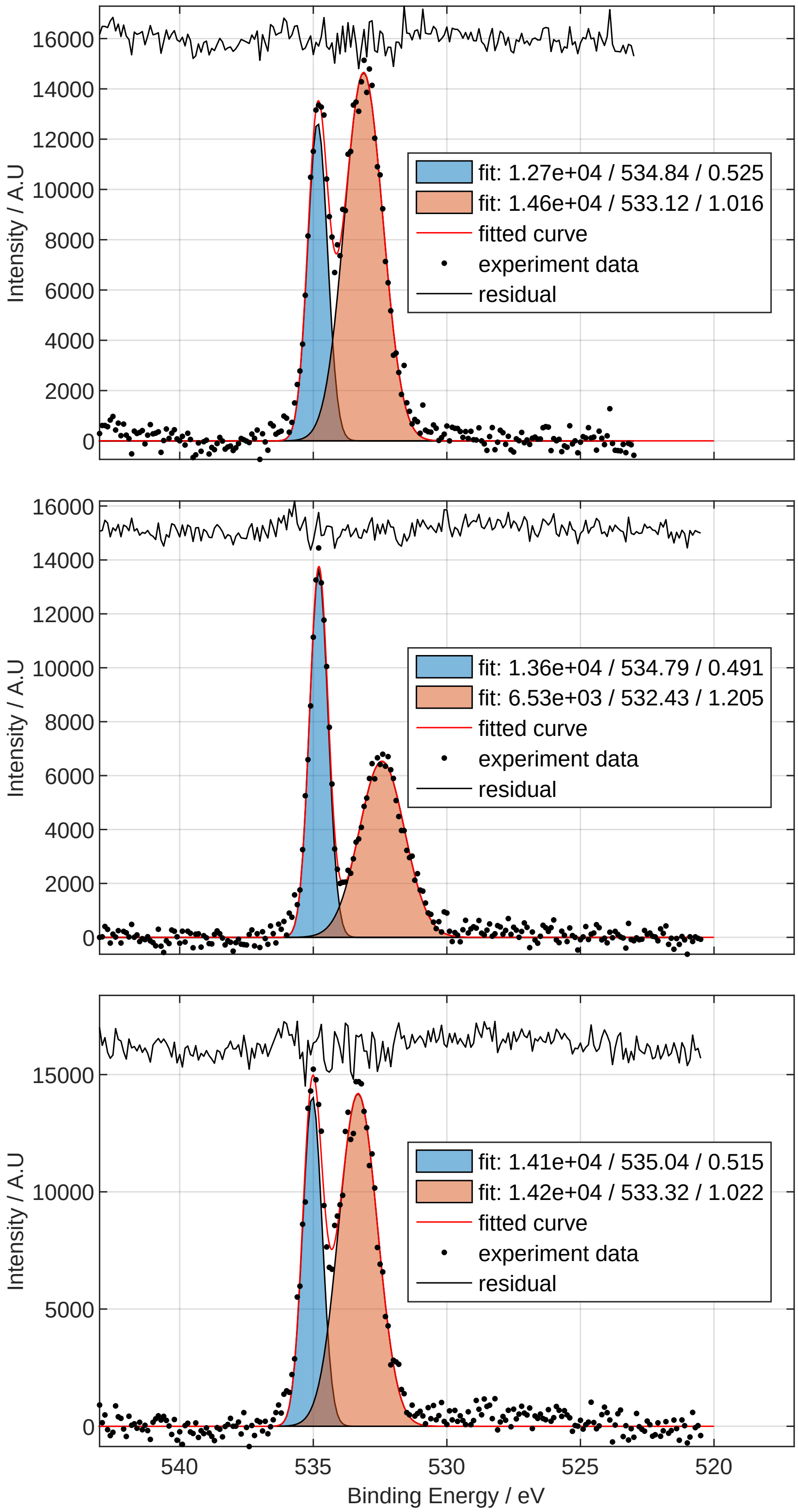

Figure 4.9: From top to bottom: fit of the O1s spectra before, during, and after dosing 2×10^{-5} mbar of HA. A lump charging correction of 3.0 eV is applied to all spectra (no fine charging correction).

4.3.3.1 *Summary N/O*

Table 4.8: Results of deconvolutions for the different experimental conditions, expressed as the ratio of the area of the N 1s component to that of the condensed phase water O 1s component. We have kept the $\mathrm{R{-}NH_2}$ peak at 399.4 eV for consistency with respect to the liquid jet analysis even though the fit is very small. We allow the fit to be negative to avoid the build-up of a signal from the noise. Figure 4.3 in the main text only shows values for the protonated and unprotonated species, respectively, where the values for the unprotonated species are the sum of the areas of the components related to $\mathrm{R{-}NH_2}$ and $\mathrm{R{-}NH_2^{ads}}$.

Data ref. #	**LJ 8.2**	**LJ 10.2**	**LJ 12.2**	**7**	**2**	**5**
R-NH3+	0.0381	0.0253	0.00031891	0.1938	0.1423	0.2340
R-NH2 ads	0	0	0	0.1244	0.1967	0.1875
R-NH2	0.0024	0.0268	0.0826	-0.0113	-0.0980	0.0299
Protonated	0.0381	0.0253	0.00031891	0.1938	0.1423	0.2340
Unprotonated	0.0024	0.0268	0.0826	0.1130	0.0987	0.2174

REFERENCES

1. Gabathuler, J. P., Manoharan, Y., Artiglia, L. & Ammann, M. “Adsorption of Hexylamine on ice, as seen by near ambient pressure XPS” (in preparation).
2. Ratner, B. D. & Castner, D. G. “Electron spectroscopy for chemical analysis”. *Surface analysis: the principal techniques* **2** (2009).
3. Niskanen, J., Fondell, M., Sahle, C. J., Eckert, S., Jay, R. M., Gilmore, K., Pietzsch, A., Dantz, M., Lu, X., McNally, D. E., Schmitt, T., Vaz da Cruz, V., Kimberg, V., Gel’mukhanov, F. & Föhlisch, A. “Compatibility of quantitative X-ray spectroscopy with continuous distribution models of water at ambient conditions”. *Proceedings of the National Academy of Sciences* **116**, 4058–4063 (2019).
4. Brown, M. A., Redondo, A. B., Jordan, I., Duyckaerts, N., Lee, M.-T., Ammann, M., Nolting, F., Kleibert, A., Huthwelker, T., Mächler, J.-P., Birrer, M., Honegger, J., Wetter, R., Wörner, H. J. & Bokhoven, J. A. v. “A new endstation at the Swiss Light Source for ultraviolet photoelectron spectroscopy, X-ray photoelectron spectroscopy, and X-ray absorption spectroscopy measurements of liquid solutions”. *Review of Scientific Instruments* **84**, 073904 (2013).

5

ADDITIONAL EXPERIMENTS

This chapter is dedicated to several additional studies that I have done during my Ph.D. and are relevant to the thesis. This chapter consists of:

1. a study of the surface disorder as a function of temperature in liquid water. This study provides additional context to the temperature dependence of the PEY-XAS spectra used to assess the QLL on ice (Chapter 3).
2. a proof-of-principle of the PEY-XAS depth profile. This section is an application of the relationship between the kinetic energy window and the mean probing depth in PEY-XAS (Equation 3.2), that has been established with the Monte Carlo simulation (Chapter 3).
3. a study of the direct impact of total pressure on the QLL. The Monte Carlo simulation results (Chapter 3) demonstrated that gas phase scattering reduces the probing depth and hence, that gas phase pressure could be a confounding factor in the assessment of the temperature dependence of the QLL (Chapter 3). This study completes the analysis of the role of the gas phase by observing its direct impact on the surface disorder.

Separated, none of these studies are complete enough to constitute a publication however, they provide additional context and open new insights for future experiments.

5.1 SURFACE DISORDER IN LIQUID WATER: A TEMPERATURE DEPENDENCE

The structure of the hydrogen-bonding network at the surface of the ice and its temperature dependence has been covered in Chapter 3. Here, I present a study of the same observable but on the liquid-gas interface. In this section, we investigate the coordination of water molecules in the hydrogen bonding network at the surface of liquid water.

Water and life are intimately linked [1]. Proteins don't fold into their functional shape and enzymes don't work in the absence of water molecules. No other liquid can replace water, and water possesses anomalous properties in comparison to other liquids such as a high boiling and melting point, a high latent heat, a high density in its liquid phase, and a high surface tension. Even more puzzling, the density increases upon cooling until it reaches a maximum at 4°C. Then, the density decreases from 4°C towards supercooled temperatures, as if tiny ice crystals were forming within the liquid but without triggering bulk crystal growth in this temperature range. These unexpected bulk properties are attributed to the specificity of water to form hydrogen bonds. If the hydrogen bonds were 7% stronger or 29% weaker, water would not be liquid at the average temperature on the surface of Earth ($\sim$ 14°C), and the temperature of maximum density (4°C) would disappear if the hydrogen bonds were just 2% weaker [2]. Most probably, life would not exist on Earth as we know if there was no hydrogen bonding between water molecules [3].

By definition, liquid water has no fixed structure: molecules are free to move within the body of the liquid and are interacting with each other by forming, breaking, and reforming hydrogen bonds. Yet, these hydrogen bonds impose a certain degree of order in this molecular jumble [4]. The lifetime of hydrogen bonds is about 0.1 ps at 100°C, 1 ps at 0°C, and 20 ps at -20°C [2]. The energy involved in forming and breaking hydrogen bonds is on average $23.3\,\mathrm{kJ\,mol^{-1}}$, corresponding to about half[1] of the enthalpy of vaporization [5]. Neutron scattering studies and results from computer simulation support the idea that a water molecule is on average bonded to 4 other water molecules in the constantly reorganizing hydrogen bonding network. Other more recent studies claim that a water molecule in liquid binds on average to only 2 other molecules and that the structure of liquid water is made of chains and rings [6]. Despite its vital importance for life, the structure of water is poorly understood [4]. To learn more about hydrogen bonds in liquid water, we take advantage of the near ambient pressure partial electron yield X-ray Absorption Spectroscopy (PEY-XAS) technique to directly probe the structure of the hydrogen bonding network, that is, the number and spatial arrangement of the hydrogen bonds within the first neighboring water molecules, as a function of temperature.

The liquid water data were acquired at the Swiss Light Source (SLS) with the liquid jet chamber [7] at the SIM beamline [8]. A linear background fitted in the range 527 to 532 eV has been removed and the spectra are normalized to the total area. No further data processing steps have been i.e. the normalization for photon flux, gas phase subtraction, higher-order light consideration, and beamline offset have not been treated. The data here is meant to be compared with itself and requires further processing in

---

[1] assuming that there are 2 hydrogen bonds for each water molecule

order to be compared with the literature data. The gas phase data were acquired at the ISS beamline [9] and have been corrected for the monochromator offset (1.6 eV).

Figure 5.1 shows, on the main panel, the PEY-XAS spectra of liquid water at two different temperatures. The red spectrum was acquired at room temperature ($\simeq 20°C$) and referred to as the "warm water" spectrum. The blue sprectrum was acquired while the water was traveling through a cooling hose whose temperature was set to $0°C$ and referred to as the "cold water" spectrum. The warm and cold water spectra are the average of 2 and 3 consecutive measurements, respectively. The background has been removed and the spectra are normalized to the total area. Shown in black on the upper plot, is the difference between the warm and the cold water spectra normalized to the post-edge intensity of the warm water spectra i.e. $\frac{Warm-Cold}{Warm(540eV)}[\%]$. In doing so, small differences are shown more clearly and allow for a better comparison of the spectral features and their intensities. The gas phase water spectrum is shown in light blue for comparison. Both warm and cold water spectra have generally similar features, which are a pre-edge at 535 eV, a main-edge at 538 eV, and a post-edge at 540 eV. See also the spectral description in Chapter 3. Small but noticeable differences are indicated by the letters A, B, and C. Features A and B in the figure seem to coincide with the gas phase peaks. This can be explained by the difference in the water vapor pressure above water as a function of temperature. Warm water has a higher vapor pressure than cold water and therefore, the gas phase contribution to the PEY-XAS in Figure 5.1 between them should not be identical. However, the liquid jet data has not been corrected for the

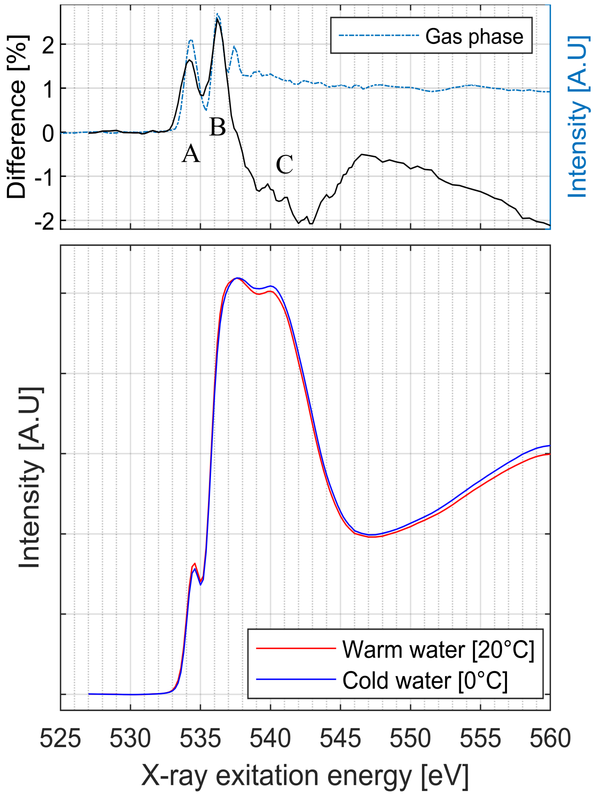

FIGURE 5.1: PEY-XAS spectra of liquid water at 0°C and 20°C. Acquired at a KE window of 412 to 437 eV

monochromator offset (if any) of this particular beamline, and it could also be that the feature in A is the pre-edge as in [10], and the feature in B might simply be an artefact from this particular normalization. Region C shows a large negative difference that is quite broad in energy range compared to features A and B. This energy range for feature C also does not coincide with any features observed in the gas phase spectrum. The spectrum of ice exhibits a more pronounced intensity in the post-edge region than in the main edge, which has been correlated with the tetrahedral coordination of the hydrogen bonds around the oxygen atom [11, 12]. Feature C occurs in this same energy range. This suggests that the hydrogen bonding network in cold water may be more 'ice-like' than the one in warm water. We note that the KE energy window used here is quite 'bulk sensitive', with a mean probing depth of about 6 nm (see Section 3.1.3.2).

The data suggest that the warm water is more disordered or 'liquid-like' than the cold water with a difference of $\simeq$ 2% relatively to the post-edge intensity in the range from 0 to 20°C. Despite differences in probing depth and data treatment, this result agrees remarkably well with the findings of Nilsson et al. [11] (XRS), Pylkkänen et al. [13] (RIXS), and Meibohm et al. [14] (transmission mode XAS) who found similar differences over a similar temperature range. Note that the 2% difference in the main-to-post-edge ratio observed here when the temperature decrease by 20°C can be extrapolated to supercooled water however, it remains small in comparison to the 25% change that we can observe between clean ice at -10°C and liquid water at 0.5°C (see Figure 3.2).

It would require more spectra over a larger temperature range to establish the temperature trend more quantitatively. It would also be interesting to compare electron yield XAS data with those obtained in either transmission or fluorescence mode to be able to assess differences in the hydrogen bonding structure between surface and bulk.

REFERENCES

1. Henry, M. “The state of water in living systems: from the liquid to the jellyfish.” *Cellular and molecular biology (Noisy-le-Grand, France)* **51**, 677–702 (2005).
2. Chaplin, M. *Water Structure and Science* `https://water.lsbu.ac.uk/water/`.
3. Luck, W. A. “Water and Ions in Biological Systems”, 95–126 (1985).
4. Ball, P. “Water - an enduring mystery”. *Nature* **452**, 291–292 (2008).
5. Suresh, S. & Naik, V. “Hydrogen bond thermodynamic properties of water from dielectric constant data”. *The Journal of Chemical Physics* **113**, 9727–9732 (2000).
6. Wernet, P., Nordlund, D., Bergmann, U., Cavalleri, M., Odelius, M., Ogasawara, H., Näslund, L. Å., Hirsch, T. K., Ojamäe, L., Glatzel, P., Pettersson, L. G. M. & Nilsson, A. “The Structure of the First Coordination Shell in Liquid Water”. *Science* **304**, 995–999 (2004).
7. Brown, M. A., Redondo, A. B., Jordan, I., Duyckaerts, N., Lee, M.-T., Ammann, M., Nolting, F., Kleibert, A., Huthwelker, T., Mächler, J.-P., Birrer, M., Honegger, J., Wetter, R., Wörner, H. J. & Bokhoven, J. A. v. “A new endstation at the Swiss Light Source for ultraviolet photoelectron spectroscopy, X-ray photoelectron spectroscopy, and X-ray absorption spectroscopy measurements of liquid solutions”. *Review of Scientific Instruments* **84**, 073904 (2013).
8. Flechsig, U., Nolting, F., Fraile Rodriguez, A., Krempask, J., Quitmann, C., Schmidt, T., Spielmann, S. & Zimoch, D. *Performance measurements at the SLS SIM beamline* in *AIP Conference Proceedings* **1234** (2010), 319–322.
9. Orlando, F., Waldner, A., Bartels-Rausch, T., Birrer, M., Kato, S., Lee, M. T., Proff, C., Huthwelker, T., Kleibert, A., van Bokhoven, J. & Ammann, M. “The Environmental Photochemistry of Oxide Surfaces and the Nature of Frozen Salt Solutions: A New in Situ XPS Approach”. *Topics in Catalysis* **59**, 591–604 (2016).
10. Bluhm, H., Ogletree, D. F., Fadley, C. S., Hussain, Z. & Salmeron, N. “The premelting of ice studied with photoelectron spectroscopy”. *Journal of Physics-Condensed Matter* **14**, L227–L233 (2002).
11. Nilsson, A., Nordlund, D., Waluyo, I., Huang, N., Ogasawara, H., Kaya, S., Bergmann, U., Naslund, L. A., Ostrom, H., Wernet, P., Andersson, K. J., Schiros, T. & Pettersson, L. G. M. “X-ray absorption spectroscopy and X-ray Raman scattering of water and ice; an experimental view”. *Journal of Electron Spectroscopy and Related Phenomena* **177**, 99–129 (2010).
12. Niskanen, J., Fondell, M., Sahle, C. J., Eckert, S., Jay, R. M., Gilmore, K., Pietzsch, A., Dantz, M., Lu, X., McNally, D. E., Schmitt, T., Vaz da Cruz, V., Kimberg, V., Gel’mukhanov, F. & Föhlisch, A. “Compatibility of quantitative X-ray spectroscopy with continuous distribution models of water at ambient conditions”. *Proceedings of the National Academy of Sciences* **116**, 4058–4063 (2019).
13. Pylkkänen, T., Sakko, A., Hakala, M., Hämäläinen, K., Monaco, G. & Huotari, S. “Temperature Dependence of the Near-Edge Spectrum of Water”. *The Journal of Physical Chemistry B* **115**, 14544–14550 (2011).

14. Meibohm, J., Schreck, S. & Wernet, P. “Temperature dependent soft x-ray absorption spectroscopy of liquids”. *Review of Scientific Instruments* **85**, 103102 (2014).

5.2 PEY-XAS DEPTH PROFILE

We have seen in Chapter 3 that the probing depth of the PEY-XAS depends on the KE window. In this section, we use this relationship to probe different depths of the ice surface with EY-XAS.

5.2.1 *Background*

X-ray photoelectron spectroscopy (XPS) and Auger electron spectroscopy (AES) are well-established measurement techniques extensively used in surface science. However, the data of interest is very often covered by a spectral background that arises from inelastic scattering in the bulk. This background is often subtracted even though it contains useful information about the bulk. For example, Tougaard [1] showed with gold samples containing copper inclusions, that the background of the Cu 2p elastic peak contained information about the structural arrangement of copper in the different gold samples. The different backgrounds are shown on Figure 5.2, where four different surface configurations of copper and gold are depicted (top) along with their corresponding spectra (graph). In configuration a, a thin copper layer is on top of a gold bulk. In this case, the copper electrons are practically not scattered. In configuration b, the copper is buried vertically within the gold, and electrons scatter along the copper depth. In configuration c, the 1 nm-thick copper layer is buried below 2 nm of gold, forcing all copper electrons to scatter through the gold. Finally, in configuration d, a bulk copper sample is covered with 2.5 nm of gold. All surface morphologies are designed to give the same Cu 2p intensity as shown in the main panel below however, the backgrounds are all very different and provide valuable information about the sample composition.

In partial electron yield X-ray absorption spectroscopy (PEY-XAS), one typically acquires the spectra by sweeping the photon energy and measuring electrons within a KE range situated somewhere in the background of the primary Auger emission. Since the background is composed of scattered electrons, i.e. electrons that have scattered at least 1 time, the probing depth is larger than if one measures primary electrons. The more electrons scatter, the deeper they likely originate from in the bulk of the sample [3]. Therefore, the electron kinetic energy that we can precisely measure in PEY-XAS contains depth information. As presented in Chapter 3, a Monte Carlo method is particularly well suited to understand the physics of inelastic scattering and find the relationship between the kinetic energy and probing depth. The simulation described in Section 3.1.3.2 gave quantitative answers regarding the probing depth as a function of the kinetic energy window.

A direct measurement of the ice surface using PEY-XAS at different probe depths can be accomplished by taking advantage of the physics of electron scattering. This technique has been successfully demonstrated on a SiO_2/Si sample [4, 5]. This section presents a study of the QLL on ice at −39 °C probed with PEY-XAS at different KE, i.e. probed at different depths. This temperature was chosen in order to avoid problems related to the ice stability since relatively colder ice evolves slower than warmer ice.

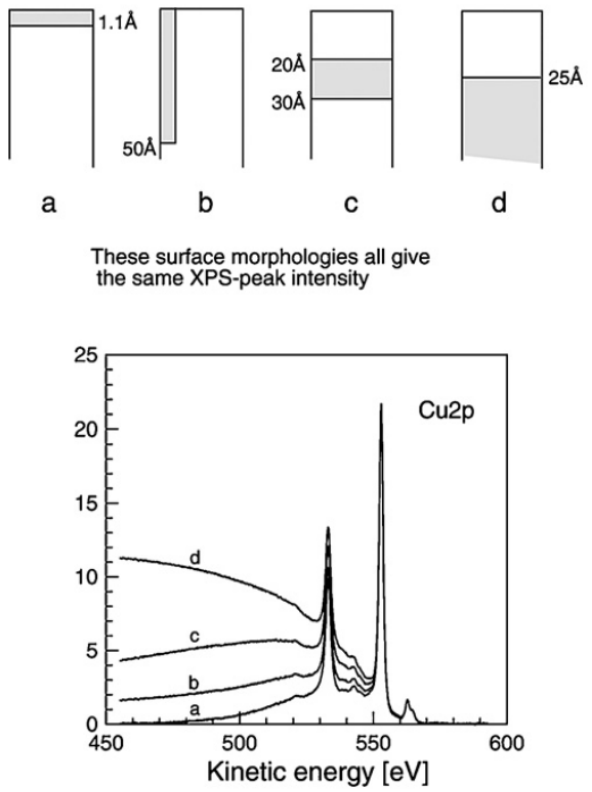

FIGURE 5.2: Four widely different surface structures of copper (light gray) in gold (white) that give identical peak intensities. Taken from [2]

This also avoids to have high water vapor pressure in the experimental chamber, as this influences the probing depth via scattering in the gas phase.

5.2.2 *PEY-XAS depth profile: experimental procedure*

This experiment was conducted at the ISS beamline [6], of the Swiss Light Source (SLS). The beamline characteristics are well suited for measuring O K-edge XAS and the experimental chamber is compatible with pressure up to tens of mbar, allowing the study on ice in equilibrium with its vapor pressure. Ice was grown *in situ* from vapor deposition and stabilized at a temperature of −39 °C. The beamline slits were fully open (1.2/1.2) to maximize the signal and the photon energy was swept from 520 to 570 eV.

The pass energy of the electron analyzer was set to 50 eV and the acquisition was running in fixed mode, meaning that the electron analyzer only measures electrons within a kinetic energy window centered at the desired KE and with a width of 5 eV . I measured PEY-XAS on the surface of ice at KE of 450, 400, 350, and 300 eV i.e. probing 4 different depths, labeled DP 1-4 on Figure 5.3. In addition to the 4 different KE windows, this figure shows the different XPS traveling peaks that we may find around the measurement parameters. In particular, the Au 4f crosses the DP1 range, however the ice should cover the gold sample holder and thus should be undetectable. These KE windows were chosen to be low enough to avoid the O 1s from the 2$^{\text{nd}}$ order light and O 2s which would appear on the O K-edge XAS spectra at KE= 500 eV . Depth profiling was stopped at DP4=300 eV to avoid the eventual C 1s peak from contamination at 250 eV.

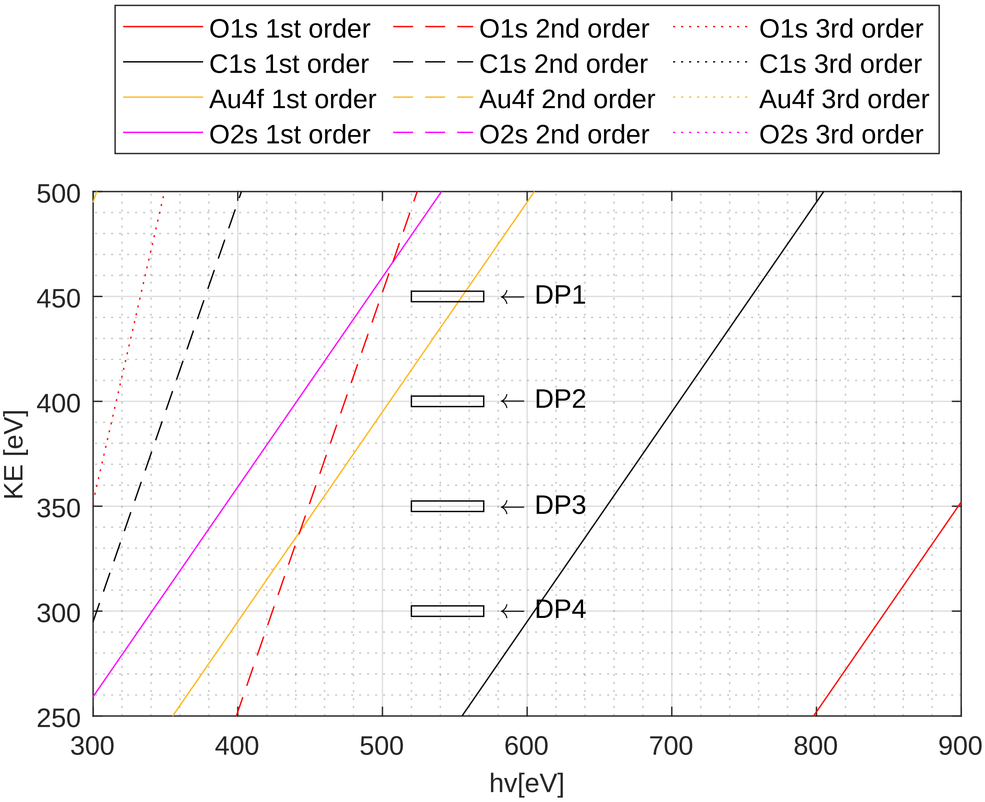

FIGURE 5.3: Map of the experiment in the kinetic energy vs photon energy space.

The Monte Carlo simulation, see Section 3.1.3.2, provides values for the mean probing depth of PEY-XAS on ice, reported in Table 5.1. I measured each KE window 2 or 3 times per round to make an average and check stability. I measured a total of 4 rounds.

TABLE 5.1: Mean probing depth (MPD) of PEY-XAS for different probing kinetic energies (KE) according to the Monte Carlo simulation.

KE [eV]	MPD [nm]
500 (no scatter)	2.2
450	4.75
400	6.85
350	8.5
300	10

5.2.3 *Results and discussion*

Figure 5.4 shows the (averaged) raw spectral data from round 4, which exhibited excellent ice stability. The different intensities are due to the decreasing background intensity as the measured KE becomes far from the emission KE of $\sim 500\,\text{eV}$.

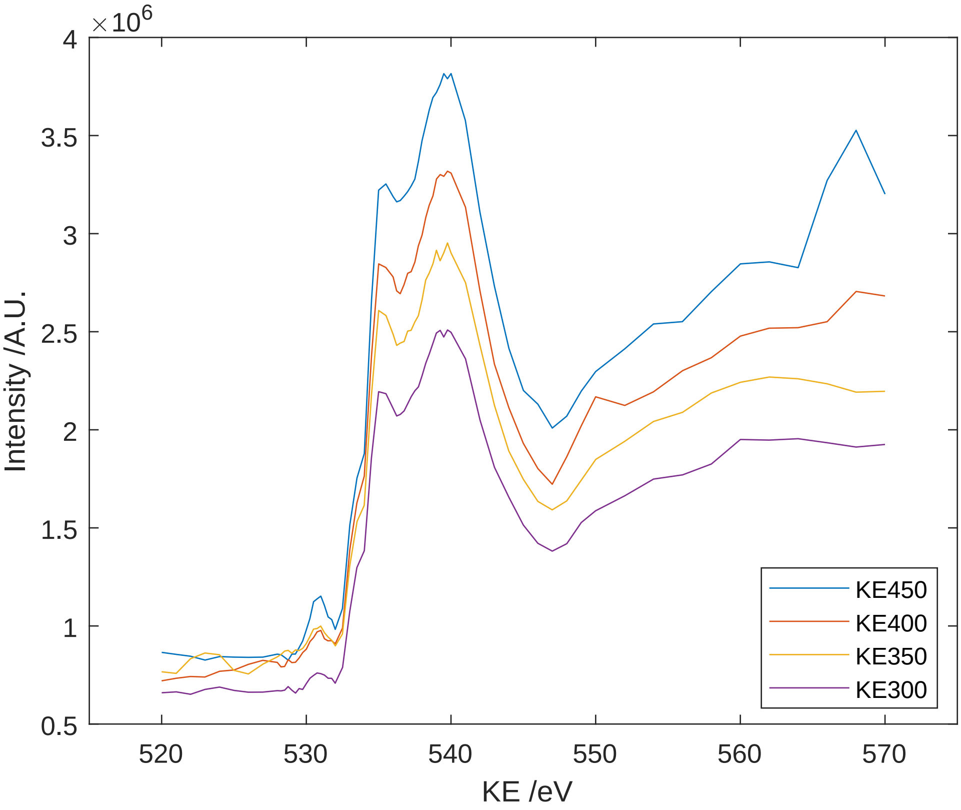

FIGURE 5.4: PEY-XAS spectra of ice for the different KE window. Round 4, raw data. Not corrected for beamline shift.

Figure 5.5 shows the area of the carbon contamination feature for the different KE windows. The different rounds are color-coded and open circle markers indicate that the ice is stable while the cross markers indicate that the ice was slightly growing or shrinking, as seen from the intensity change within the 2-3 repetitions. A linear fit is indicated with the dashed red line. The trend of the fit reveals that the carbon contamination is more intense when we measure at a high KE window as we are more sensitive to the surface because electrons at high KE are mostly primary and have not scattered. At a lower KE window, electrons may have scattered and therefore the KE window is probing more of the bulk. However, because ice is a dynamic surface, we cannot exclude that the carbon contamination is evolving with time. Indeed, from rounds 1 to 2, we see a net decrease, from rounds 2 to 3 the signal is more or less stable, and from 3 to 4 the carbon signal increase.

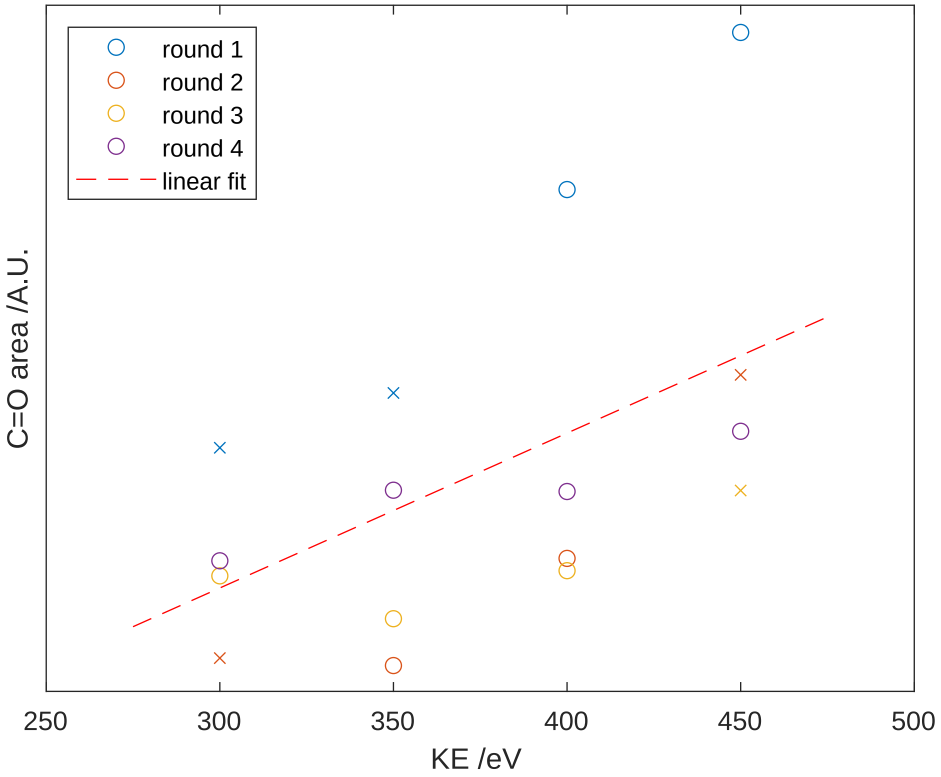

FIGURE 5.5: Carbon contamination feature for the different KE. The different rounds are color-coded. The open circles indicate that the ice is stable within the averaged iterations. The cross marker indicates that the ice was slightly moving between 2 averaged iterations. The dashed red line indicates a linear fit.

Figure 5.6 shows the ice-like feature extracted from the post-to-main-edge ratio[2] for the different probing depths. Here as well, a linear fit is indicated with the dashed red line. Despite the high scatter, we see a slope in the linear fit, indicating that the ice is more disordered at high KE or on the surface and it gets more ordered as we probe more towards the bulk with a lower KE window. This is an exciting result since the QLL is expected to be very thin at −39 °C. In fact, in Chapter 3, we have taken the surface of ice at −40 °C as a reference for bulk ice, considering the QLL thickness to be 0.

---

[2] calculated from peak heights

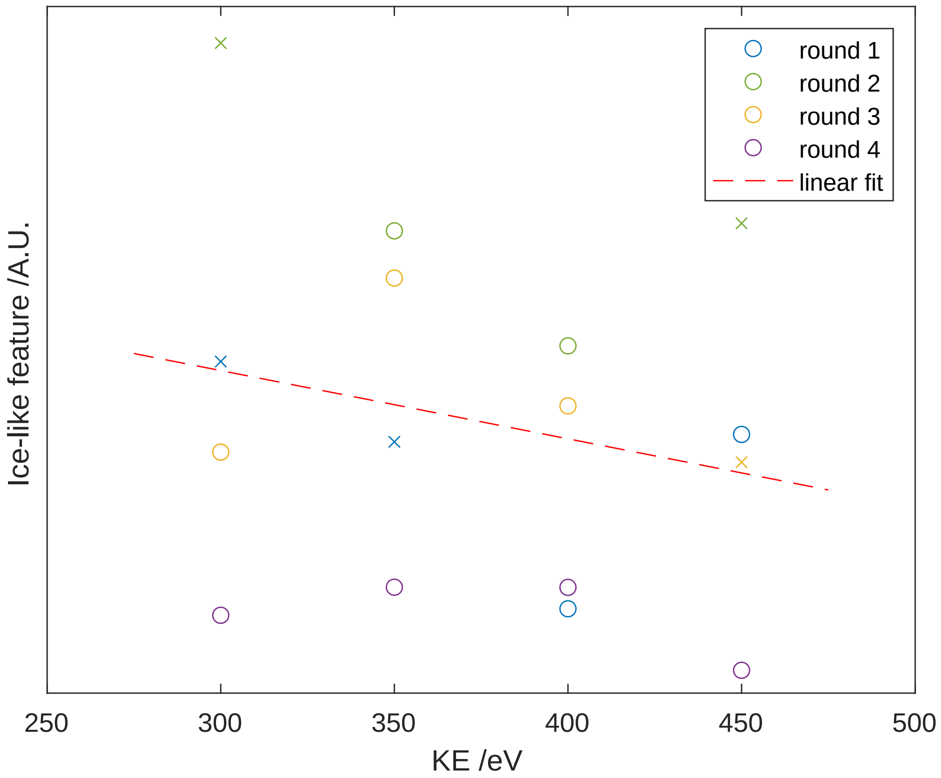

FIGURE 5.6: Ice-like feature extracted from the post-to-main-edge ratio of PEY-XAS of ice at -39°C measured at different KE. The open circles indicate that the ice is stable within the averaged iterations. The cross marker indicates that the ice was slightly moving between 2 averaged iterations. The dashed red line indicates a linear fit.

5.2.4 *Conclusion and outlook*

Despite the large scatter in the data, the different probing depths provide measurable differences that are in line with expectations. These results are a very encouraging *proof of principle* and show that PEY-XAS depth profiling is possible on environmental samples. Naturally, it would be interesting to measure the QLL at warmer temperatures as the liquid-like character would be more pronounced than here. Combined with simulations, this would allow us to assess the depth profile of the QLL and address its nature. For example, instead of being a layer as we have to assume for the interpretation of PEY-XAS, the QLL could be a local disorder exponentially decreasing with depth. If so, what exactly varies with temperature? is it the amplitude of the exponential function or its characteristic length? Such descriptions of the QLL are presented on Figure 5.7.

The PEY-XAS depth profile could also be used on more elaborated samples such as an adsorbed trace species on ice to see if we can observe differences in the physical and chemical interactions as a function of depth.

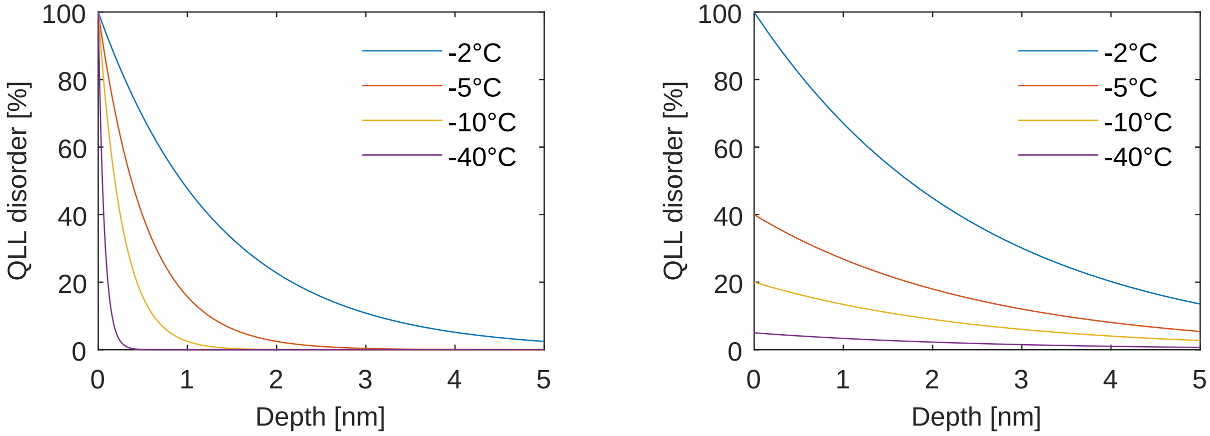

(a) The exponential characteristic length decrease with temperature.

(b) The exponential amplitude decrease with temperature.

FIGURE 5.7: Possible QLL disorder distribution as a function of depth for different temperatures, based on an exponential function. The difference between a and b are writen in the respective captions.

REFERENCES

1. Tougaard, S. "Surface nanostructure determination by x-ray photoemission spectroscopy peak shape analysis". *Journal of Vacuum Science & Technology A: Vacuum, Surfaces, and Films* **14**, 1415–1423 (1996).
2. Tougaard, S. "Energy loss in XPS: Fundamental processes and applications for quantification, non-destructive depth profiling and 3D imaging". *Journal of Electron Spectroscopy and Related Phenomena* **178**, 128–153 (2010).
3. Werner, W. S. M. "Electron transport in solids for quantitative surface analysis". *Surface and Interface Analysis* **31**, 141–176 (2001).
4. Isomura, N., Soejima, N., Iwasaki, S., Nomoto, T., Murai, T. & Kimoto, Y. "Depth-selective X-ray absorption spectroscopy by detection of energy-loss Auger electrons". *Applied Surface Science* **355**, 268–271 (2015).
5. Isomura, N., Cui, Y. T., Murai, T., Oji, H. & Kimoto, Y. "X-ray absorption spectroscopy to determine originating depth of electrons that form an inelastic background of Auger electron spectrum". *Journal of Applied Physics* **122** (2017).
6. Orlando, F., Waldner, A., Bartels-Rausch, T., Birrer, M., Kato, S., Lee, M. T., Proff, C., Huthwelker, T., Kleibert, A., van Bokhoven, J. & Ammann, M. "The Environmental Photochemistry of Oxide Surfaces and the Nature of Frozen Salt Solutions: A New in Situ XPS Approach". *Topics in Catalysis* **59**, 591–604 (2016).

5.3 IMPACT OF TOTAL PRESSURE DIRECTLY ON THE QLL

5.3.1 *Motivation*

We have seen in Chapter 3 that the probing depth of the PEY-XAS decreases as a function of gas phase pressure. Therefore, the water vapor pressure could be a confounding factor in quantifying QLL thickness using this technique since the warmer the ice surface temperature, the more surface sensitive the probing depth (red path in Figure 5.8). Figure 5.8 shows a flowchart diagram that represents the different pathways from increasing the ice temperature to the observed enhancement of the QLL. The "++" signs indicate an increase, while the "−−" sign indicates a decrease.

Another confounding factor could be the absolute pressure. Due to the very definition of pressure, i.e. the force applied on a surface due to the collision of molecules on that surface, it is reasonable to assume that pressure would have a direct effect on the QLL, as shown with the blue arrow on Figure 5.8.

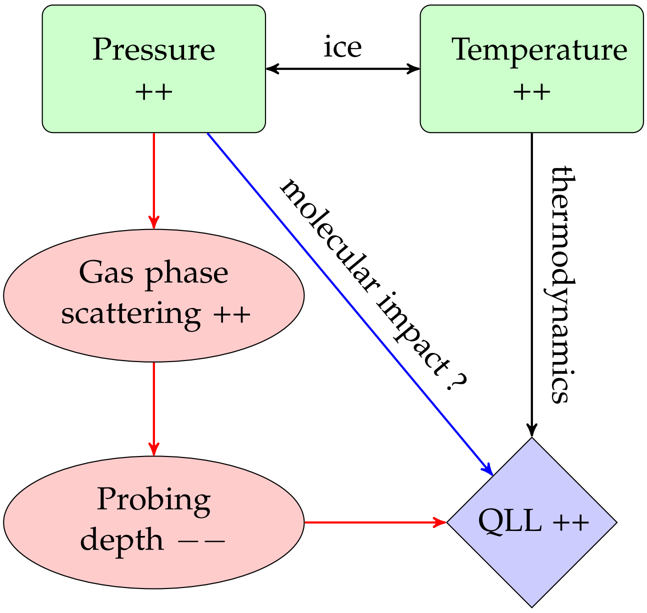

FIGURE 5.8: Flowchart representing the different pathways from the temperature increase of the ice surface (Temperature ++) to the observed enhancement of the QLL (QLL++).

Let's briefly calculate the velocities and the typical flow of molecules on the ice surface in the experimental chamber, when the temperature is close to the melting point and the ice is in equilibrium with its vapor pressure. The purpose here is to derive the rate of molecular exchange between the gas phase and surface as a function of pressure. At the melting point, the average speed of water molecules is:

$$\overline{v} = \sqrt{\frac{8k_BT}{\pi m}} = 566\,\mathrm{m\,s^{-1}} \tag{5.1}$$

where $\overline{v}$ [m s^{-1}] is the average speed of gas phase molecules, k_B= 1.38×10^{-23} J K^{-1} is the Boltzmann constant, T=273.15 K is the temperature of the ice at the triple point, and m=2.99×10^{-26} kg is the mass of the water molecule.

At equilibrium, the rate of gas phase molecules hitting and leaving the surface is the same. Assuming that all molecules land and leave with a speed perpendicular to the surface, every time a molecule hits the ice surface, it transfers a momentum $\vec{p} = m\vec{v}$ and when a molecule leaves, a momentum $\vec{p} = -m\vec{v}$ is lost such that the rate of change in momentum at equilibrium is:

$$\frac{dp}{dt} = \dot{n}m(\overline{v} - (-\overline{v})) = 2\dot{n}m\overline{v} \tag{5.2}$$

where $\dot{n} = \frac{dn}{dt}$ [s^{-1}] is the number of molecules landing and leaving a surface at equilibrium and $\overline{v}$ [m s^{-1}] is the average speed of gas phase molecules. Since:

$$P_0 = \frac{F}{A} \tag{5.3}$$

$$F = ma = m\frac{dv}{dt} = \frac{dp}{dt} = 2\dot{n}m\overline{v} \tag{5.4}$$

where P_0 [Pa] is the pressure in the gas phase and F [N] is the force applied on a surface A [m^2], we can calculate the rate of molecules exchange on a surface A=1 cm^2 for a pressure P_0=500 Pa (5 mbar) and using Equation 5.1 for the $\overline{v}$ value:

$$\dot{n} = \frac{P_0 A}{2m\overline{v}} = 1.48 \times 10^{21}\ \text{s}^{-1} \tag{5.5}$$

which is equivalent to 1.32×10^6 bilayers/s (using 1.12×10^{15} molecules/cm^2 for 1 bilayer of thickness 3.678 Å [1]).

The QLL is a very small interfacial disorder with an observed thickness in the range of just a few bi-layers as seen from PEY-XAS [2]. in view of the results of Equation 5.1 and Equation 5.5, we cannot exclude that the PEY-XAS observations are independent of the varying pressure in the range 0-5 mbar: possibly, as the temperature of the ice increases, the chamber pressure increases as well and is causing the observed surface disorder.

The goal of this section is to evaluate the direct connection between the absolute pressure and the QLL. In order to achieve that, I prepared cold ice where no QLL is measurable with PEY-XAS and I try to induce the QLL by dosing 5 mbar of nitrogen while keeping the same cold temperature. If no change in the QLL signal is observed upon dosing 5 mbar of nitrogen on the cold ice, then the impact of absolute pressure on the QLL is negligible. However, if there is indeed a change i.e. if the QLL is enhanced as the pressure increase, then the pressure is a confounding factor for the assessment of the QLL with PEY-XAS. In this case, the consequences for atmospheric chemistry are substantial: at an altitude of $\sim$ 5000 m in the troposphere, the temperature is around ~ -20 °C and the pressure is $\sim$ 500 mbar. This means that the QLL would be 100 times larger than what we observe in the experimental chamber at a temperature of -2 °C i.e. with 5 mbar. Note that the surface temperature of the ice cannot be warmed up by the warm gas flow of nitrogen, because the temperature is set by the partial pressure of water above the surface that we control very precisely. Any increase of surface temperature will immediately increase the vapor pressure and induce evaporative cooling.

5.3.2 *Methods*

This experiment was conducted at the ISS beamline [3], of the Swiss Light Source (SLS). The experimental chamber is well suited to study environmental samples under a near-ambient pressure atmosphere up to 10 mbar. A gold-coated sample holder is actively cooled with a cold nitrogen gas flow and allows to reach temperatures from 20 °C down to −150 °C in the chamber. However, the metallic soldering of the sample holder is only certified until −100 °C(!). Ice was grown *in situ* from vapor deposition and the initial plan was to stabilize it at a temperature of −40 °C. At this temperature, the vapor pressure is only 0.12 mbar and adding 5 mbar would change the pressure drop between the water reservoir and the experimental chamber, leading to a different water flow rate to the chamber and changing the equilibrium temperature by an unknown amount. In other words, the ice wouldn't be stable long enough to acquire the necessary data. One approach to solve this problem would be to increase the vapor pressure in the water reservoir by the same amount of what is added to the chamber i.e. 5 mbar, to keep the same pressure drop and hopefully have stable ice. Nonetheless, that is not what I did. Only the 0.4 mm-diameter capillary was mounted on that day and it would have taken hours to grow ice by dosing 0.12 mbar (when the second, 2 mm-diameter capillary is mounted, I can use the second water reservoir to grow ice more rapidly, while keeping the first water dosing at the equilibrium flow rate). In order to avoid the issue of ice stability, I decided to cool down the ice to −120 °C so that it is stable as a rock. The ice surface was surprisingly clean at this temperature, as shown on the survey before and after the reference PEY-XAS measurement Figure 5.9. The spectra in Figure 5.9 were acquired at 1000 eV photon energy, 50 eV pass energy and are offset for clarity. 0.75 mbar of gas phase nitrogen was dosed and according to the O 1s and N 1s photoemission peaks visible at 455 and 590 eV, the charging value was $\sim$ 10 eV. The yellow line is the difference between the spectra before and the one after hence, the small positive peak at the O 1s position and reaching $\sim 10^5$ indicates that the ice signal decreased by 10 ± 5 %. The inset shows the C 1s region of the survey before the reference PEY-XAS, without offset and reveal a remarkably clean surface: the spectrum is completely flat at 700 eV, where we would expect the C 1s photoemission peak from adventitious carbon contamination to appear.

The beamline slits were open (1/1) and the O K-edge was acquired with PEY-XAS using the KE window from 425 to 525 eV. The pass energy was set to 50 eV. In total, 3 PEY-XAS spectra were acquired: one reference spectrum with low gas phase pressure -just enough to keep charging to a reasonable value-, and two spectra with high nitrogen pressure as described in Table 5.2.

In file #50, the temperature was oscillating from −110 °C to −130 °C due to the poorly adjusted PID setting of the sealing temperature (which we have discovered was the reason for temperature oscillations half a year later, in Feb. 2022). In files #52 and #53, the flow was fixed at 6 ml/min and the temperature was stable at −137 °C. The

Table 5.2: Environmental parameters during the different measurements.

File #	Temperature	Pressure (N_2)
50	−120 °C (oscillating)	0.75 mbar
52	−137 °C	5.42 mbar
53	−137 °C	5.45 mbar

temperatures are below the limit stipulated by our technician, but if I may quote a famous scientist: *"a person who never made a mistake never tried anything new."*

— Albert Einstein

Hopefully, the soldering endured the experiment and the sample holder is still vacuum-tight.

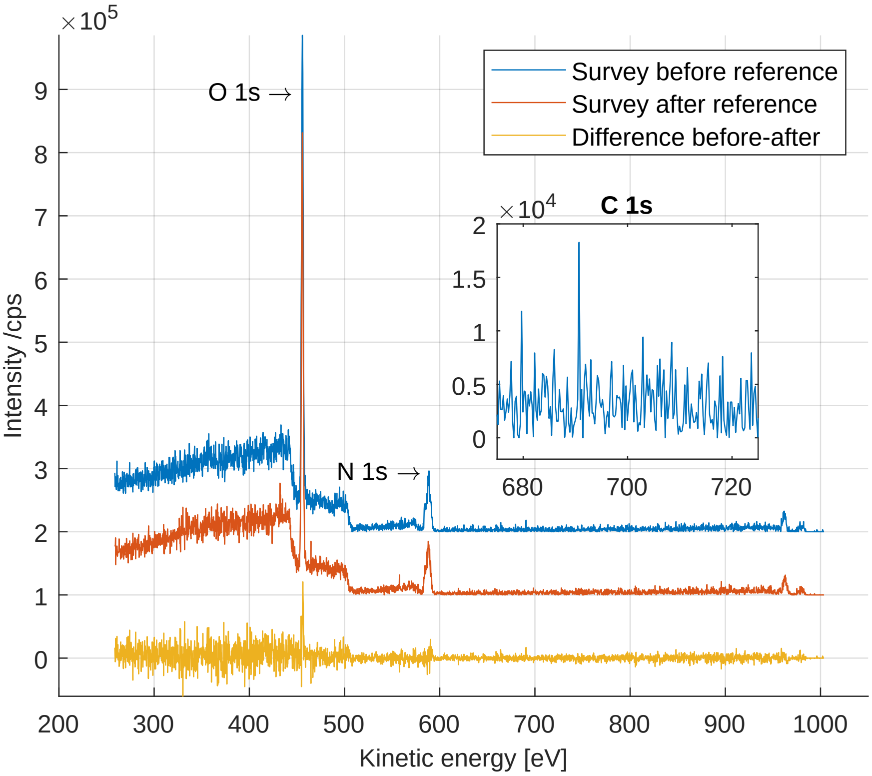

Figure 5.9: Survey spectra at 1000 eV photon energy before and after the reference PEY-XAS spectra i.e. at −120 °C and 0.75 mbar, offset for clarity. O 1s and N 1s photoemission peaks are visible at 455 and 590 eV, respectively. The inset shows the C 1s region of the survey before the reference PEY-XAS, without offset.

The ice surface during the measurements at −120 °C was very smooth and transparent as seen from the endoscope, thus for the purpose of viewing, one of the ice photographs from the end of the experiment is shown on Figure 5.10a. The ice was sublimating and tiny white spots (small islands?) appeared on the surface, increasing the contrast. The temperature was ≃−85 °C at the moment of the photograph. Figure 5.10b shows the cooling N_2-gas exhaust at the end of the experiment i.e. after 5 hours of cooling the sample holder to ≃−130 °C.

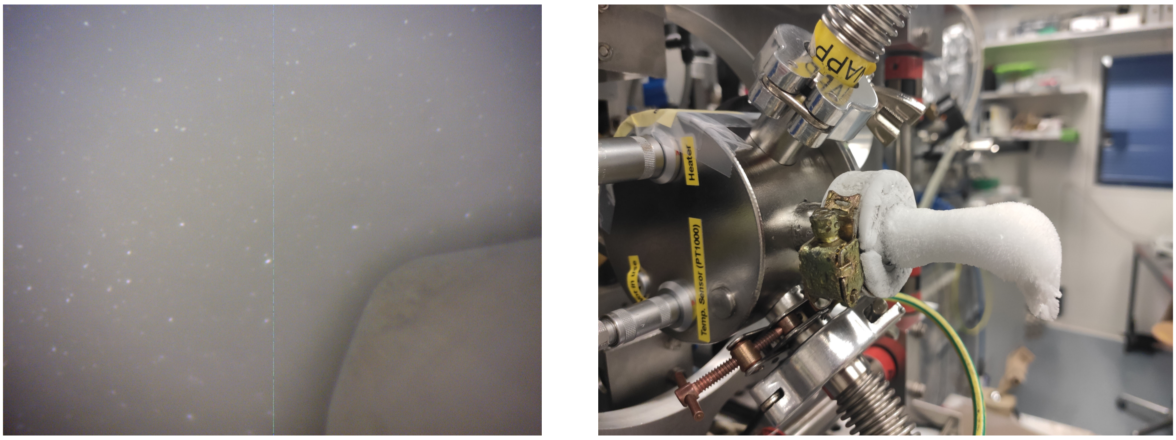

(a) Surface of the ice as seen by the endoscope. The temperature at the moment of the photograph was $\simeq -85\,^{\circ}\mathrm{C}$

(b) Cooling N_2-gas exhaust after 5 hours of measurement.

FIGURE 5.10: Photographs of (a) the ice surface and (b) the cooling N_2-gas exhaust at the end of the experiment.

5.3.3 *Results and discussion*

Figure 5.12 shows the PEY-XAS of ice at different pressure. The red spectrum is at low pressure and the blue spectrum is the average of spectra #52 and #53 at high pressure. The spectra are very similar. The signal-to-noise ratio is lower in the red spectra due to the gas phase scattering lowering the counts. We see a sharp peak and a little dip from 534 to 535 eV, enlarged in the inset, corresponding to the free hydrogen feature. This could be due to the gas phase scattering decreasing the probing depth making it more surface sensitive than the reference spectra (blue), as illustrated on Figure 5.11.

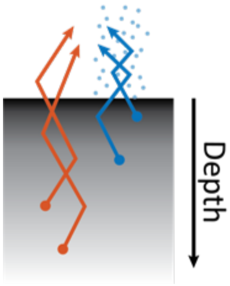

FIGURE 5.11

To quantitatively interpret the spectra, I deconvoluted them using 8 gaussians. From the gaussian deconvolution, I extract the main-to-post-edge ratio and the pre-edge intensity, both indicating 'liquid-like' content or disorder within the probing depth. The results are compared on Figure 5.14 and show that the ice reference and the ice under 5 mbar of pressure have a similar surface disorder, that cannot be quantitatively distinguished with the current signal-to-noise ratio. Indeed, all surface disorder data lies within the errorbars (1 standard deviation calculated from the 2 repetitions) of the ice measurement under 5 mbar of pressure. The data presented here suggest that pressure doesn't significantly impact surface disorder at such low temperatures.

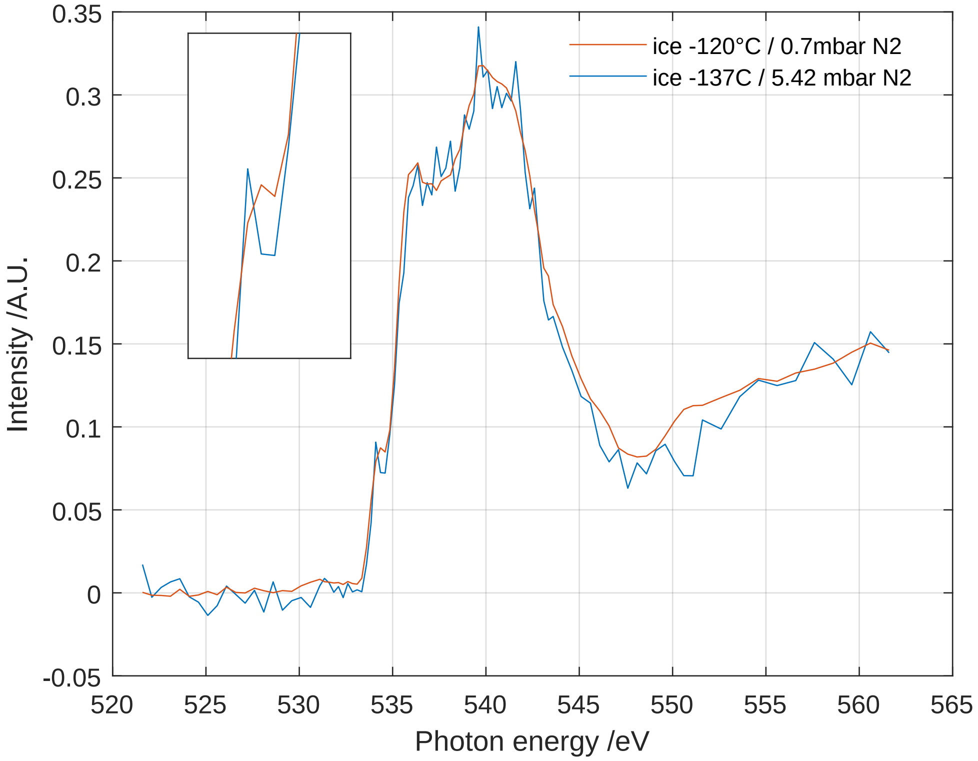

FIGURE 5.12: PEY-XAS of ice for different pressures. The red spectrum was acquired at −120 °C and with 0.7 mbar of nitrogen in the gas phase. The blue spectrum is the average of two spectra acquired at −137 °C and with 5.42 mbar of nitrogen in the gas phase. The inset is an enlargement of the spectra at the pre-edge region, at 535 eV

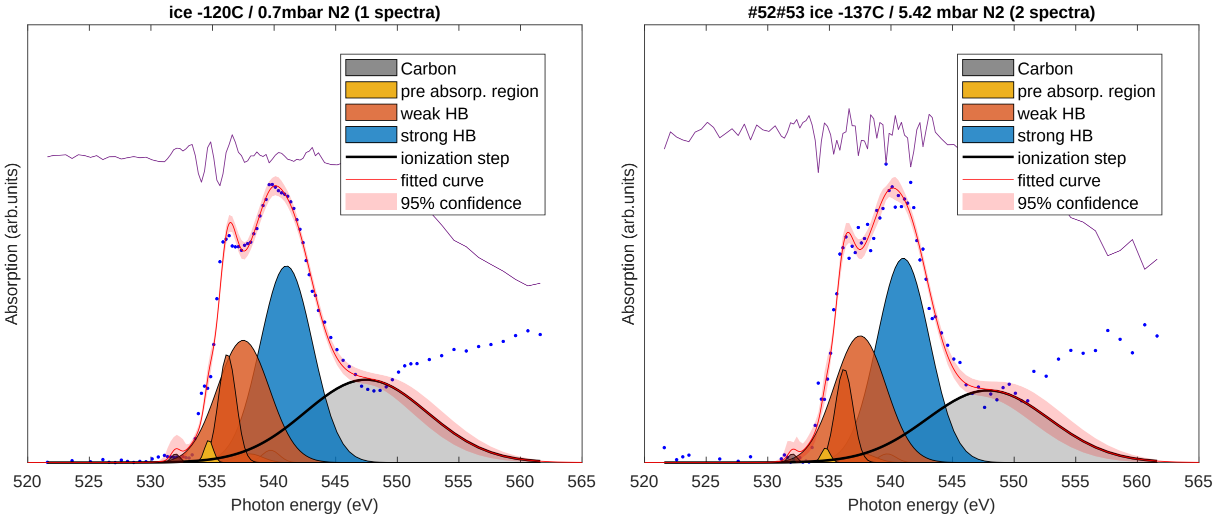

(a) Gaussian deconvolution of the PEY-XAS data at low gas phase pressure.

(b) Gaussian deconvolution of the PEY-XAS data at high gas phase pressure.

Undoubtedly the ice surface here was too rigid to be perturbed by gas phase molecular impact, and gas phase velocities (Equation 5.1) might as well decrease as they approach the cold surface. We note that the ice might prefer a cubic structure in this region of its phase diagram.

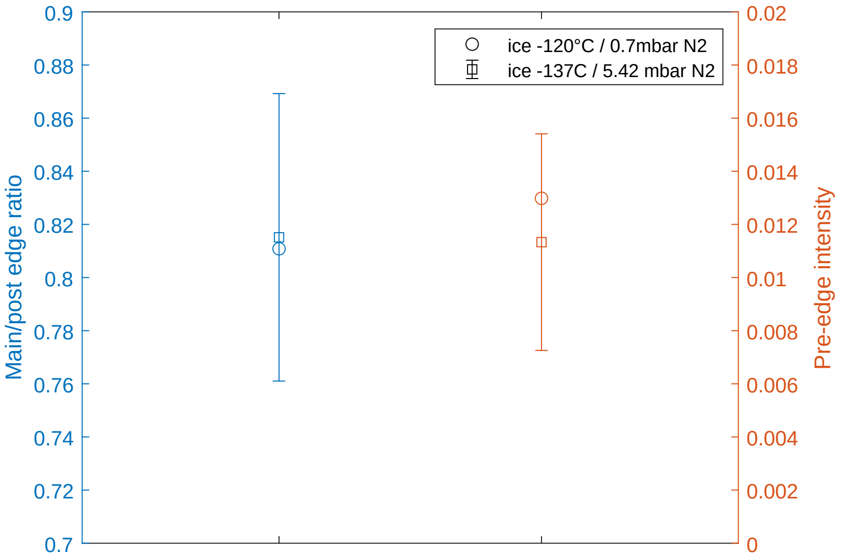

FIGURE 5.14: Surface disorder for cold ice sample with different pressure, as seen with PEY-XAS with different observable features. The blue data points are to be read on the left y-axis and correspond to the liquid-like feature or surface disorder as observed from the main-to-post-edge ratio. The red data points are to be read on the right y-axis and correspond to the liquid-like feature of surface disorder as observed from the intensity of the pre-edge. The circles denote the ice data at -120°C / 0.7 mbar while the squares represent the average of the two repetitions data of the ice at -137°C / 5.42 mbar and the errorbars are ±1 standard deviation.

5.3.4 *Conclusion*

I have measured PEY-XAS on clean cold ice with and without an additional amount of pressure, corresponding to the pressure variation that occurs when measuring the temperature dependence of the QLL on ice. There was no measurable increase in surface disorder upon dosing 5 mbar of N_2, at $-137\,°C$. The surface of this ice was spectacularly clean, although we would expect from such a cold surface to behave as a cold trap and accumulate all sorts of organic contamination from the chamber.

REFERENCES

1. Röttger, K., Endriss, A., Ihringer, J., Doyle, S. & Kuhs, W. "Lattice constants and thermal expansion of H2O and D2O ice Ih between 10 and 265 K". *Acta Crystallographica Section B: Structural Science* **50**, 644–648 (1994).
2. Bluhm, H., Ogletree, D. F., Fadley, C. S., Hussain, Z. & Salmeron, N. "The premelting of ice studied with photoelectron spectroscopy". *Journal of Physics-Condensed Matter* **14**, L227–L233 (2002).
3. Orlando, F., Waldner, A., Bartels-Rausch, T., Birrer, M., Kato, S., Lee, M. T., Proff, C., Huthwelker, T., Kleibert, A., van Bokhoven, J. & Ammann, M. "The Environmental Photochemistry of Oxide Surfaces and the Nature of Frozen Salt Solutions: A New in Situ XPS Approach". *Topics in Catalysis* **59**, 591–604 (2016).

6

SUMMARY

We have seen in the introduction (Chapter 1) that behind its apparent simple form, the water molecule has many intriguing properties. Among them, the ability to form hydrogen bonds is what allows water to be at the same time the matrix of life on Earth and ubiquitous in its solid form. Indeed, ice is present on Earth in many forms such as snow on the ground or ice clouds in the upper troposphere and lower stratosphere, and presents a large surface for chemical interaction with trace gases present in the atmosphere. The surface of the ice acts as a platform for heterogeneous chemistry and studies have reported that it can significantly influence the chemical equilibria in the atmosphere. Close to its melting point, ice exhibits surface disorder, which we describe with a Quasi-Liquid Layer (QLL) on its surface. This property allows the surface of the ice to dissociate acids and protonate bases which are present in the atmosphere in trace amounts. The introduction also provides insights into synchrotron based X-ray excited electron spectroscopy which is an ideal surface technique to study the QLL and the adsorption of trace species on the surface of the ice.

In Chapter 2, I characterized the beamline in terms of beam composition and showed that a significant fraction of second-order light was present and was perturbing the measurement in a non-negligible way. I estimated potential error propagation on depth profiles and XAS spectra and calculated the necessary correction.

In Chapter 3, I presented a study of the temperature dependence of QLL thickness using PEY-XAS. I developed a careful analysis of the different uncertainties related to this technique, with a special focus on the probing depth assessment using a Monte Carlo simulation of physical processes. The results of the simulation remind us of the importance of electron scattering and how they influence the probing depth in PEY-XAS. The results indicate that the choice of the kinetic energy (KE) window used to detect electrons in PEY-XAS increases the probing depth by a factor $\sim$3 for the KE window used in the QLL analysis, and that gas phase scattering decreases this factor down to $\sim$1.5, at 5 mbar. The improved QLL thickness estimation reveals a rather thin QLL thickening from 0.5 to 2 nm from -10 to -1°C. These results are in agreement with previously reported QLL thicknesses with the same technique and with molecular dynamics (MD) simulations.

In Chapter 4, we investigate the adsorption of an atmospheric base, hexylamine, on the surface of the ice, using XPS. We show that a saturated monolayer is present already at a partial pressure of 2×10^{-5} mbar at -20°C, and that more than half of the HA molecules are protonated. This shows how the surface of the ice, despite being formally a solid, chemically interacts with an atmospheric trace gas. With PEY-XAS, we were able to measure how the adsorbed HA perturbs the structure of the hydrogen bonding network of the ice below. The degree of perturbation is equivalent to what has been observed on the clean ice surface at -1°C, thus at 20 K higher temperature. Further corrections are needed in the analysis of the HA of ice data to quantitatively compare with the QLL of clean ice data. For example, electron scattering in the HA layer and in the argon has not been considered.

In Chapter 5, I present several additional works that are either preliminary to or the logical continuation to the QLL study (Chapter 3). Chapter 5 consists of:

- a study of the surface disorder as a function of temperature in liquid water, as a complement to the QLL investigation. Similarly to the QLL on ice, the surface of liquid water increases its disorder with temperatures, as seen with PEY-XAS. This is in agreement with the literature.
- a proof-of-principle of the PEY-XAS depth profile. As an application of the MC simulation results presented in Chapter 3, I established the proof-of-principle of PEY-XAS depth profiling ability on an ice sample, by probing the HB network and the carbon contamination as a function of depth. Despite the large scatter in the data, differences were measurable between the different probing depths, in line with expectations. These results are a very encouraging and show that PEY-XAS depth profiling is possible on environmental samples.
- a study of the direct impact of total pressure on the QLL. I investigated the direct impact of 5 mbar of N_2 gas phase pressure on the surface disorder and found no correlation on the ice at -120°C. This means that the impact of pressure is negligible under these conditions, which is a satisfying result.

To summarize, the results presented in this thesis improve the understanding of the probing depth in PEY-XAS and may contribute to a revised picture of the QLL and its molecular-level interaction with trace gases.

Chapter 2 Showed us that experimental artefacts can be unnoticed and cause large errors in the data interpretation. It is always important to do calibration measurement and quality control to ensure that the experiment is running as expected.

In Chapter 3, the investigation of the QLL thickness lead to rather thin results, of the order of 0.5 to 2 nm, although at the molecular scale these represent multiple bilayers of ice. Together with the ability of solutes to enhance the QLL, these results contribute to understanding how the QLL impacts the chemical equilibrium in the atmosphere. Because each experimental methods have their own flaw and artifacts, it would be interesting to use multiple analytical tools at the same time to study the same ice sample. For example: XPS with SFG or neutron scattering.

In Chapter 4, we have seen that a base can chemically react with ice and induce a QLL. One could think of increasing the complexity level of such an experiment by introducing a second species to the system, for example, a strong acid with a weaker acid (that would behave as a buffer), and see how the chemical equilibria evolve as the surface concentration of the strong acid increases.

Chapter 5 explored different aspects related to this thesis. The configuration of soluble species at the liquid-gas interface in aqueous systems and their impact on the structural arrangement of water molecules is definitely worth expanding, especially now that we have a tool to probe the HB network of liquid water as a function of depth. In addition, the temperature dependence of such a system may be of interest to the ice nucleation community. The potential of the PEY-XAS technique has yet to demonstrate its strength on environmental samples. For example, by looking throughout the QLL at warm temperatures (-10 to -1°C) to address its true nature or by analyzing each and every layer of the (cold) ice surface when it is disordered by the presence of a solute adsorbate.

Jérôme Gabathuler

Ph.D. in physical chemistry

Swiss
born in 1993
☎ *+41 78 906 95 89*
✉ *jerome.gabathuler@gmail.com*
www.linkedin.com/in/JeromeGabathuler

Education

ETH, *Eidgenössische Technische Hochschule*, Zürich, Switzerland.

2018 – 2022
- **PhD in atmospheric science**.
  Hydrogen-bonding structure of the ice surface studied with x-ray absorption spectroscopy.
  Aerosol I ○ Surfaces, Interfaces and their Applications I ○ Cloud Microphysics ○ Stratospheric Chemistry

EPFL, *Swiss Federal institute of technology*, Lausanne, Switzerland.

2015 – 2017
- **Master in Applied Physics**.
  Master project : Solar water purification using photocatalysis with a novel TiO_2 nano-porous aerogel
  Internship : Research in acoustics for Bernafon AG (Bern) ○ Acoustical impedance analysis and modeling

2011 – 2014
- **Bachelor in Physics**.
  Numerical analysis ○ Computational physics ○ Experimental methods in physics ○ Physics labs : Laser diodes, Nuclear Magnetic Resonance (NMR), Optical confinement, Supraconductivity, Plasma physics

Experience

Aug. 2018 – Sept. 2022 **PhD student**, *Paul Scherrer Institut*, Villigen, Switzerland.
Worked on ice interface and its interaction with the atmosphere, studying effects of the QLL seen with X-ray electron spectroscopy. ○ Provided comprehensive research and data analysis when designing and executing experiments, and documented findings. ○ Gathered, reviewed, and summarized literature from scientific journals and produced graphs and other scientific calculations using MATLAB. ○ Analyzed acquired information and presented it to professors.

Sept. 2016 – Jan. 2017 **Engineering Intern**, *Bernafon*, Bern, Switzerland.
Research in acoustics ○ Acoustical impedance analysis and modeling ○ Designed and coordinated engineering tests and experiments ○ Used MicroCap software to design electrical circuits analogous to the acoustic system and model impedance behavior

Sept. 2014 – Apr. 2017 **Teaching assistant**, *EPFL*.
Guide students during exercise sessions for classes of Physics I, II, III & IV ○ teach Physics labs

Skills

IT	Matlab ○ C++ ○ Python ○ LabView ○ MicroCap ○ Word ○ Excel ○ PowerPoint ○ LaTeX
Technical	Strong understanding of the laws of physics ○ Analytical and problem-solving skills with great attention to details ○ Able to work independently ○ Exceptional presentation and reporting skills
Soft	Enthusiastic and passionate about physics ○ Open-minded ○ Curious ○ Adaptable ○ Responsible ○ Willingness to Learn ○ Excellent verbal and written communication in English and French
Languages	English: *C2-C1* ○ German: *B1-B2* ○ French: *Mother tongue*

Interests

Science ○ Energy ○ Environment ○ Sustainable developpement ○ DIY projects • **Music** ○ Playing the trumpet ○ playing the violin ○ Experience with wind orchestra and string orchestra • **Sports** ○ Cycling ○ running ○ swimming ○ climbing ○ tennis ○ badminton ○ ski and snowboard ○ winter bathing

PUBLICATIONS

Articles in peer-reviewed journals:

1. Yang, H., Boucly, A., **Gabathuler, Jérôme Philippe**, Bartels-Rausch, T., Artiglia, L. & Ammann, M. "Ordered Hydrogen Bonding Structure of Water Molecules Adsorbed on Silver Iodide Particles under Subsaturated Conditions". *The Journal of Physical Chemistry C* **125**, 11628–11635 (2021).
2. Horváth, E., **Gabathuler, Jérôme Philippe**, Bourdiec, G., Vidal-Revel, E., Benthem Muñiz, M., Gaal, M., Grandjean, D., Breider, F., Rossi, L., Sienkiewicz, A., *et al.* "Solar water purification with photocatalytic nanocomposite filter based on TiO2 nanowires and carbon nanotubes". *npj Clean Water* **5**, 1–11 (2022).

Articles in preparation:

3. Yang, H., Boucly, A., **Gabathuler, Jérôme Philippe**, Kiselev, A. & Ammann, M. "Surface potassium ion exchange controls the coordination of water molecules on the surface of feldspar" (in preparation).
4. Chen, S., Artiglia, L., Yang, H., **Gabathuler, Jérôme Philippe**, Boucly, A., Iezzi, L., Abouhaidar, R., Duflot, D., Toubin, C. & Ammann, M. "Influence of surfactants with differently charged headgroups on the surface propensity of bromide" (in preparation).
5. **Gabathuler, Jérôme Philippe**, Yang, H., Manoharan, Y., Boucly, A., Alpert, P. A., Artiglia, L., Bartels-Rausch, T. & Ammann, M. "The premelting of ice revisited with X-ray absorption spectroscopy" (in preparation).
6. **Gabathuler, Jérôme Philippe**, Manoharan, Y., Artiglia, L. & Ammann, M. "Adsorption of Hexylamine on ice, as seen by near ambient pressure XPS" (in preparation).

Conference contributions:

7. Manoharan, Y., **Gabathuler, Jérôme Philippe**, Huanyu, Y., Artiglia, L., Boucly, A., Ammann, M. & Bartels-Rausch, T. *Photochemistry of acids and bases at the air-ice interface* in *AGU Fall Meeting Abstracts* (2019), A43Q p. 3128.
8. **Gabathuler, Jérôme Philippe**, Manoharan, Y., Yang, H., Boucly, A., Artiglia, L., Ammann, M. & Bartels-Rausch, T. *The Quasi-Liquid Layer on ice observed with NEXAFS* in *EGU General Assembly Conference Abstracts* (2021), EGU21 p. 15629.
9. Vattioni, S., Weber, R., Klaus, O., Luo, B., Dykema, J., Stenke, A., Feinberg, A., Döbeli, M., Vockenhuber, C., Krieger, U. K., Weers, U., Yang, H., Artiglia, L., **Gabathuler, Jérôme Philippe**, Ammann, M., Keutsch, F. N., Peter, T. & Chiodo, G. *Risks and benefits of stratospheric solid particle injection for climate intervention* in *AGU Fall Meeting Abstracts* (2022).